2007

The 2001 Martian global dust storm

Jeffrey M. Gawrych
San Jose State University

THE 2001 MARTIAN GLOBAL DUST STORM

A Thesis

Presented to

The Faculty of the Department of Meteorology

San Jose State University

In Partial Fulfillment

of the Requirements for the Degree

Master of Science

by

Jeffrey M. Gawrych

May 2007

APPROVED FOR THE DEPARTMENT OF METEOROLOGY

Alison F. C. Bridger

Dr. Alison Bridger

Douglas M. Sinton

Dr. Douglas Sinton

Robert M Haberle

Dr. Robert Haberle, NASA Ames Research Center

APPROVED FOR THE UNIVERSITY

Rhea J. Williamson 04/25/07

ABSTRACT

THE 2001 MARTIAN GLOBAL DUST STORM:

by Jeffrey M. Gawrych

This thesis addresses the 2001 Martian global dust storm and its effect on the atmospheric circulation of Mars. The 2001 global dust storm was unique in that it was seen in its entirety by the Mars Global Surveyor satellite. Observational data were collected, and compared with numerical simulations from the NASA Ames Mars General Circulation Model (MGCM) to better examine and understand the storm.

MGCM simulations using dust data as a driving condition showed numerous components of the circulation were modified by the storm, including enhanced slope winds, stationary waves, and the mean meridional circulation. The Hellas region shows consistently high surface wind stresses, and increased stresses are observed in the Claritas region; both regions with large observed lifting centers. Simulations show the presence of a wave-1 stationary wave, an amplified overturning circulation, and a large tidal response to heavy dust loading were all factors in the storm's development.

ACKNOWLEDGEMENTS

I wish to thank those people who aided in the completion of this work:
My committee members: Dr. Alison Bridger, Dr. Robert Haberle, and Dr. Douglas Sinton for providing encouragement, motivation, and feedback. NASA Ames Research Center Mars Atmospheric Modeling Group members. My wife Renee, for allowing my dreams to come true, and all students, faculty, and staff of the San Jose State University Department of Meteorology.

TABLE OF CONTENTS

LIST OF TABLES

LIST OF FIGURES

1. INTRODUCTION

1.1 Motivation and Importance of Work

Global dust storms are unique meteorological events that have been observed nowhere else but the planet Mars. Martin and Zurek (1992) coined the term "planet-encircling" to describe these events, but the term global dust storm will be used in this thesis. The haze created from this enormous atmospheric dust loading can be seen by Earth-based observers, capturing astronomers' interests in Mars beginning many centuries ago. These planetary-scale storms lift dust from the ground and inject it to high levels (~50 km) in the atmosphere, where it is caught up in the circulation and transported to nearly all locations on the planet (Leovy et al. 1973; Zurek et al. 1992). The addition of great amounts of dust into the atmosphere affects the weather and climate of Mars in numerous ways, yet the conditions leading to the development of global dust storms are still uncertain. Most theories involve feedback mechanisms that relate dust lifting to radiative transfer and circulation changes (Kahn et al. 1992).

The surface of Mars is covered with dust, and dust storms occur frequently on Mars, yet vary dramatically in size and strength (Zurek et al. 1992). The primary means of lifting dust are through winds (surface stresses) and free convection. Windy conditions often prevail on Mars due to the differential heating of the surface. Although Mars has no oceans, differences in surface properties exist due to the presence of ice caps, large topographical features, and different mineral structures, which in turn lead to pressure differences and wind. Nonetheless, surface winds must be quite strong (e.g., 30 $m\ s^{-1}$) to lift dust due to the low density of the Martian atmosphere (Haberle et al. 1982).

Free convection can often develop in the afternoon as the surface warms quickly leading to instability in the planetary boundary layer, and therefore lifting. The initial lifting of dust produces small events such as dust devils and local storms, the latter of which may sometimes organize into larger lifting centers (Smith 2003). Continuous dust lifting spreads dust to a broader spatial area, where it may become a local or regional storm. A global dust storm occurs when these lifting centers inject dust high into the atmosphere. The general circulation then transports dust around the globe, so that dust optical depth values increase all around the planet (Cantor et al. 2001). In a span of a few weeks, continuous dust lifting may form a thick veil of dust that may enshroud the planet (Kahn et al. 1992). Global dust storms are usually the aggregate of several regional storms, and blanket the entire globe with dust, so that even the most pronounced surface features, such as the high-elevation ridges and volcanoes become difficult to observe. The largest dust events generally begin in the southern hemisphere during the late spring and summer seasons, when solar insolation is most intense (Leovy et al. 1973). In contrast, the 2001 global dust storm began at the equinox season, significantly earlier than any other observed global storms.

Since surface dust is plentiful on the Martian surface, it is not surprisingly often injected into the atmosphere. What may be surprising is that global dust events occur very infrequently, and that only a handful of global storms have ever been closely observed. Table 1 shows the observed global dust storms in the past 100 years. The 2001 global dust storm was unique in that it was the first global dust storm to be seen in its entirety, by the Mars Global Surveyor (MGS) satellite. The MGS satellite retrieved

Table 1

Global Dust Storm Occurrence on Mars since 1925*

Year	Observed by	Seen from Earth
1925	Earth-based	Yes
1956	Earth-based	Yes
1971	Mariner	Yes
1973	Earth-based	Yes
1977	Viking	No
1977	Viking	No
1982	Earth-based	No
2001	MGS	Yes

**An observational bias must be taken into account as the angular size of Mars (as seen from Earth) changes with time.*

atmospheric information (in addition to geologic, chemical, and other scientific data), including temperature, dust opacity, and high-resolution imagery that is used to understand these large dust events.

NASA began Mars missions in the 1960s in order to better understand our neighboring planet. Since then, scientists now have many years' worth of observations that have led to a deeper understanding of the planet. These new discoveries have brought more questions and uncertainties regarding Mars' atmospheric phenomena, and therefore increased awareness and interest. Although remotely sensed observational data are being amassed by the day, a complete understanding of the atmospheric circulations

on Mars cannot be gained through these observations alone. MGCMs have been implemented to simulate the climate on Mars (Zurek et al. 1992). From MGCM simulations, one can better understand the wind, heating, dust lifting, and circulation patterns that play a role in Martian weather events, including global dust storms. Although these models are limited by the lack of comprehensive data and the uncertainty surrounding Martian weather events themselves, numerous achievements have been made through simulations.

Topography, variations in surface albedo, amount and concentration of surface dust, and non-uniform heating rates create a dynamic atmosphere that often leads to conditions favorable for dust lifting (Zurek et al. 1992). Strong surface winds and free convection lead to the formation of dust lifting centers, which may become quite organized (Kahn et al. 1992). Dust lifted to great heights can be caught in the general circulation and thus transported around the planet. It then disrupts the global radiation balance and alters the general circulation patterns (Leovy et al. 1973). Dust storms also control the amount of dust loading in the atmosphere, which has a significant impact for the future of Mars exploration.

This work is undertaken to better understand the processes controlling global dust storms. This work also strives to improve the NASA Ames MGCM. By learning more about the feedback mechanisms between dust lifting and the circulation and how the numerical model resolves dust, a more realistic and comprehensive model can be developed. Both of these goals serve to aid the future of NASA and Mars exploration.

1.2 Outline of Thesis

This work has three main objectives. The first is to collect and interpret data gathered during the 2001 global dust storm event. Most of the observations used are from the Mars Global Surveyor (MGS) satellite, which yielded information while orbiting the planet throughout the global dust storm event. These observations are used to formulate a hypothesis regarding the 2001 global dust storm.

Our second objective is to conduct MGCM simulations using the MGS dust data as parameters, using two Martian years. The 2001 global dust storm occurred in year two of the simulations, and will be much of our focus. No global dust storms formed in year one, and therefore will act as the control simulation. MGS dust data are used to better simulate the dust distributions conditions observed in both years. Output is examined and studied; this can hopefully show the role of large-scale circulation patterns, as well as smaller weather systems, which influenced the life and characteristics of the 2001 global dust storm.

The final task involves comparison of the simulations and the observations. In particular, MGS-observed dust-lifting centers are compared with model surface stress and lifting patterns. This investigation is not meant to simply reproduce the storm, but instead provide advancements in the theories of the Martian dust cycle.

2 MARS AS A PLANET

2.1 General Characteristics

Much of the surface of Mars is covered in dust, so any lifting of dust into the atmosphere may significantly alter the atmospheric structure and its thermal properties. However, in order to understand how dust gets into the atmosphere, one must first examine the planetary characteristics. Mars is the 4th planet from the sun in our solar system, and shares many similarities to Earth. Mars' rotational rate and axial tilt are similar to Earth's, and both planets have an atmosphere, although Mars' is much thinner and composed primarily of carbon dioxide (CO_2). Mars has an average sea-level pressure of only 6.1 mb, roughly 1/164th of Earths that leads to large variations of temperature, which subsequently leads to large variations in surface pressure patterns. Seasonal ice caps form in the winter hemispheres as temperatures plummet to well below the freezing point of CO_2 (145 K). The formation of the seasonal ice caps removes CO_2 from the atmosphere, while their retreat releases CO_2 into the air through sublimation, causing large seasonal surface pressure variations. Table 2 shows important physical constants that impact Martian atmosphere.

Mars has a more elliptical orbit than Earth, and this influences the intensity and duration of the seasons. Mars has an orbital eccentricity of 0.093, compared with Earth's value of 0.017. The maximum distance to the sun is ~250 million km, whereas the minimum distance is ~205 million km. This elliptical orbit causes a 40% seasonal change in solar insolation (compared with only 6% for Earth), which strongly influences temperature patterns (Zurek et al. 1992). The southern hemisphere summer is the

Table 2

Mars Constants

Orbital parameters	*Value*	*Units*
Mass	6.46×10^{23}	kg
Radius	3394	km
Surface gravity	3.72	$m\ s^{-2}$
Orbit eccentricity	0.093	
Solar Flux	590	$W\ m^{-2}$
Length of solar day	88775	s
Length of year	687	Earth days
Planetary rotation rate (Ω)	7.09×10^{-5}	s^{-1}
Atmospheric Parameters		
Scale Height	10.2	km
Gas Constant, *R*	192	$J\ K^{-1}\ kg^{-1}$
Dry Adiabatic lapse Rate	4.3	$K\ km^{-1}$

warmest season as Mars is in its closest proximity to the sun (this is called the perihelion season). The perihelion season also correlates with northern winter. In the perihelion season, surface temperatures may reach above 300 K, yet temperatures in the winter season can plummet to less than 150 K. A strong diurnal variation in temperatures is common on Mars as radiative transfer is the main mechanism for surface heating and cooling. That is, the small mass of the Martian atmosphere leads to the surface layer that is less subject to heating by advection and convection than on Earth. During the day, the Martian atmosphere absorbs solar radiation, but at night, the thin atmosphere does little to prevent infrared radiation from escaping to space, except during extremely dusty periods (Kahn et al. 1992). Globally-averaged surface pressures are at their highest (> 9 mb) during the perihelion season, when warmer temperatures sublime CO_2 ice from the polar

caps (Zurek et al. 1992). This is also the season when most large dust storms occur, as increased surface heating leads to an unstable boundary layer, aiding convection (Kahn et al. 1992).

Timekeeping on Mars is similar to that on Earth, but clarifications are in order to avoid confusion. One Martian day, or sol, is split into 24 "hours," with each hour being 3699 seconds in duration (39 seconds greater than an Earth hour). A Martian year lasts 687 Earth days. To avoid ambiguity, areocentric longitude (L_s) is commonly used to keep track of the seasonal cycle. The areocentric longitude is such that $L_s = 0°$ refers to the northern hemisphere spring equinox (i.e., the southern hemisphere autumnal equinox). MGCM data will always refer to specific L_s, although MGS data often has an associated Earth date as well.

2.2 Surface Features

Mars has seasonal CO_2 ice caps at both poles, and these expand and recede with the changing seasons. During the winter seasons, the ice caps extend to ~50° in the northern hemisphere and ~40° in the southern hemisphere. During summer, however, the ice caps never completely disappear. In the north the residual ice cap is water ice (Kieffer et al. 1976), while in the south it is CO_2 ice (Kieffer 1979; Paige et al. 1990). This interesting asymmetry in the nature of the residual caps has yet to be completely explained although recent GCM simulations suggest a major role of atmospheric heat transport (Colaprete et al. 2005).

Unlike Earth, Mars has no oceans, although large variations in topography exist. Fig. 1 shows the major topographical features of the planet, as determined by the Mars Orbiter Laser Altimeter (MOLA) on MGS (Smith et al. 2000). The northern hemisphere is generally lower and flatter, with a few exceptions being the Tharsis volcanoes in the western hemisphere and the Elysium Mons volcano to the east. The southern hemisphere is generally higher, and dotted with impact craters from asteroids and comets. One impact crater in particular, Hellas Planitia, is ~5 km deep and spans 30° in latitude and ~50° in longitude. Valles Marineris is a canyon several times larger than Earth's Grand Canyon, and is just south of the equator to the southwest of the Tharsis volcanoes.

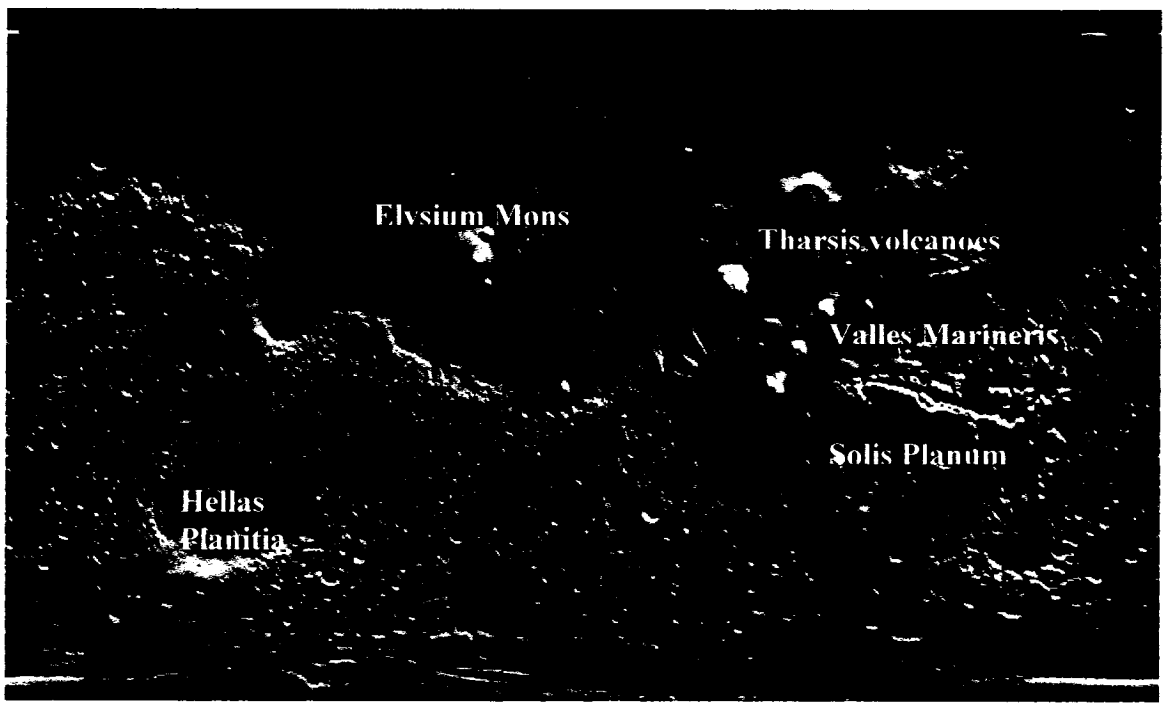

Fig. 1. Mars Orbiter Laser Altimeter (MOLA) topographical map of Mars. The northern hemisphere is generally lower and flatter than the southern hemisphere

The planetary albedo (accounts for atmosphere and surface effects) of Mars is ~ 0.25, but the presence of dust strongly influences this value (Kieffer et al. 1992). At the surface, deposition of only 10^{-4} g cm^{-2} of bright dust on an average dark area should increase the surface albedo by several tens of percent, effectively reducing the solar absorption (Kieffer et al. 1992). In the atmosphere, the amount of dust needed to account for the observed atmospheric haze and the changes in surface albedo is relatively small—equivalent to a surface layer of only a few microns for even the largest storms (Kieffer et al. 1992). Observations also show that surface albedo and color feature differences exist, so that the displacement of dust has obvious impacts on surface heating (Leovy et al. 1973). Generally, dust storms increase planetary albedo through deposition of bright dust on the surface causing cooler daytime surface and atmospheric temperatures well after a storm is over and opacities return to pre-storm values (Smith 2003). Cantor (2005) observed the albedo to increase by 3% during the 2001 global dust storm. This increase had the effect of reducing the average daytime surface temperature by nearly 1.6 K, and the effect lasted well after the storm ended (~L_s 300°).

Thermal inertia is the measure of the response of a material to heating and cooling within a substance. Both surface temperatures and their diurnal variation are driven by this measure (Zurek et al. 1992). Thermal inertia is defined as:

$$I=(k\rho C)^{1/2}$$

where k is the thermal conductivity, ρ is the density, and C is the heat capacity. Clearly, an increase in an object's heat capacity (C) or density will increase the thermal inertia. Due to the lack of oceans, most of the Martian surface has a low thermal inertia,

meaning that it heats up and cools off rapidly (Zurek et al. 1992). The effect of the constant movement and relocation of dust over the planet, which has a low thermal inertia, can therefore alter the thermal response of the surface. The average thermal inertia of the surface is about 272 SI units, but can range from lows near 50 in dust deposits to and highs near 1000 in the polar ices (Kieffer et al. 1977).

2.3 Atmosphere

2.3.1 Mass and Composition

The Viking mission determined that Mars' lower atmosphere consists mainly of CO_2 (95.3%), Nitrogen (N_2, 2.7%), and Argon (Ar, 1.6%). Smaller amounts of oxygen (O_2), carbon monoxide (CO) and noble gases are also present. The main variable constituents in the Martian atmosphere are water vapor (H_2O) and dust. Dust is an important variable atmospheric constituent whose visible optical depth (opacity) ranges from 0-5, with 5 being extremely dusty conditions (Kahn et al. 1992). The Viking Landers observed a consistent background dust opacity ranging from several tenths to more than 1.0 (Pollack et al. 1979). MGS TES observed similar background dust opacities. Fig. 2 shows the seasonal variation in TES dust opacity in a non-global dust storm year.

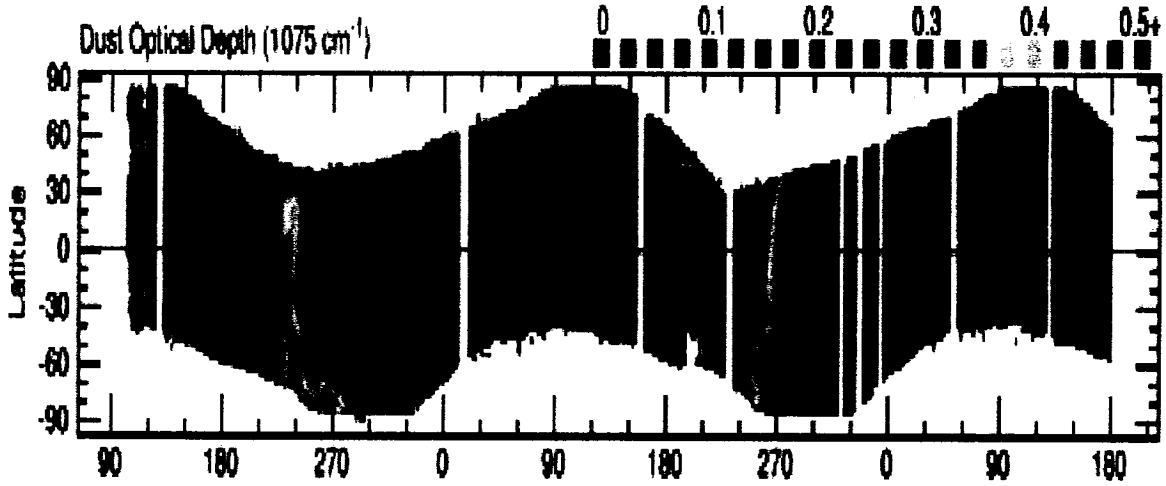

Fig. 2. Dust optical depth from Smith et al. (2001). The highest opacities (shown in red) occur near the perihelion season, making southern hemisphere spring and summer the dustiest periods of the Martian year.

2.3.2 Properties of Suspended Dust Particles

Pollack et al. (1995) revealed that Viking Lander sky brightness data could be fit with a log normal distribution to determine particle size. Suspended dust particles were shown to have mean radii of ~1.75 μm and variances of ~0.5 μm. These dust particles consist of clay, aerosolic dust, loess, and silt and have been created from such processes as impact cratering, volcanism, landslides, chemical weathering, and tectonic processes (Greeley et al. 1992). The Viking Landers observed numerous rocks on the surface approximately 2 m in diameter (Mutch et al. 1976), and between these rocks were drifts of particles < 100 μm that could easily be moved by the wind (Sharp and Malin 1984). Furthermore, the Landers noted the presence of a subsurface layer, dubbed duricrust by Binder et al. (1977) that is easily broken up into smaller particles, thereby creating another dust source.

Dust suspended in the Martian atmosphere plays a critical role in the radiation balance. Since dust is a mineral aerosol that both scatters and absorbs solar radiation and planetary outgoing radiation, the climate is strongly affected by its presence (Kahn et al. 1992). The extreme thinness of the Martian air means that it has a low heat capacity, so the atmosphere cools off and heats up more rapidly than Earth's (Leovy 2001). Also, since the atmosphere consists mainly of CO_2 (a good infrared radiation absorber), large diurnal temperature ranges are experienced in the lower levels of the atmosphere (Zurek et al. 1992). When there is little or no dust suspended in the atmosphere, the Martian atmosphere absorbs little energy directly, so heat transfer from the ground is the principle control mechanism of the temperature profile (Kahn et al. 1992).

Global dust storms may suspend large amounts of dust, and often cause air temperatures at mid-levels (25 km) to increase by 10-50 K during the day (Conrath 1975; Leovy 1985; Smith et al. 2002), while daytime surface temperatures during the 1977 global dust storm dropped 10 K (Ryan and Henry 1979). Peterfreund and Kieffer (1979) noticed that local, low-lying dust hazes appear to be 40 K cooler than the surrounding region in the daytime, and appear warmer at night. With enough dust in the air, the atmosphere cools more efficiently at night, so a vertical temperature profile would appear more isothermal in a dusty atmosphere (Smith et al. 2001). Under these circumstances, a narrower variation of temperature exists near the ground, while a greater variation is noticed at higher altitudes (Peterfreund and Kieffer 1979).

2.4 Seasonal Cycles of Dust, Water, and CO_2

Due to the abundance of mobile surface dust, dust storms affect Mars year-round and are classified according to size. Dust devils are the smallest organized dust activity (area $<10^{-1}$ km^2), followed by local storms ($\sim10^3$ km^2), regional storms ($\sim10^6$ km^2) and global events with span an area $> 10^6$ km^2 (Martin and Zurek 1993). Smaller storms are generally more common, yet have shorter durations than larger storms. Most dust activity occurs during the southern hemisphere spring and early summer when solar insolation is at a maximum, and the atmosphere is relatively warm, dusty and free of water ice clouds (Smith 2003). Cantor et al. (2001) observed that localized dust storms occur more frequently over two main regions: retreating ice cap edges, and near the high elevation regions in the northern hemisphere. The size and duration of storms in the polar cap regions varies considerably with season, but is most pronounced during the spring as the caps retreat. The tendency for local dust storms to form near cap boundaries suggests that these are net sources of dust for the atmosphere, and that lifting will occur if dust is present (Leovy et al. 1973). Briggs et al. (1979) determined that half of the dust clouds occurred at the south cap edge, where winds are enhanced by strong temperature gradients. The other half of the dust clouds could be attributed to forced lifting associated with topography (Cantor et al. 2001). It appears that dust accumulations in lifting-prone areas are potentially responsible for large dust storms, rather than small disturbances that arise elsewhere (Smith et al. 2001).

Although dust is constantly lifted from the surface, most dust clouds remain smaller in scale. The Viking Landers saw many local dust clouds form and dissipate in a

few days or less, and move with speeds 14 - 32 m s^{-1} (Peterfreund and Kieffer 1979). The growth of a global storm presumably requires the right circulation patterns and reservoirs of surface dust available for lifting. Cantor et al. (2001) state that regional dust sources are temporally variable over a twenty-year span, but the frequency of dust storms implies that regions of high dust are not the only factor in triggering dust storms. Also, cross-equatorial mass dust loading suggests the southern hemisphere subtropics require at least two-three years to replenish the dust sources before global dust storms can form (Smith 2003).

Global dust events are generally the aggregate of several smaller storms (Cantor et al. 2001). Dust storm merging is a growth mechanism that occurs in at least 50% of regional storms, and may be necessary for the formation of global storms (Cantor 2003). Past observations have yielded important clues regarding large dust storms, because these global events bring immediate changes to the weather and circulation. Besides drastically increasing global opacity levels, these storms cause a major increase in diurnal pressure amplitude, which is the amplitude of the surface pressure diurnal tide associated with the spreading of dust through a considerable vertical extent of the atmosphere (Ryan and Henry 1979). During the two planet-encircling storms in 1977, the correlation of changes in the surface pressure field with changes in atmospheric dust loading was generally consistent with predictions using the classical theory of atmospheric tides driven by the daily solar heating of a dusty atmosphere (Zurek et al. 1992). Global events also cause reductions in diurnal temperature variation, as dusty conditions decrease the amount of solar radiation reaching the surface and limit the longwave radiation lost to

space (Kahn et al. 1992). Planet-encircling storms can interrupt eddy activity as well. Ryan and Henry (1979) noticed a complete disappearance of baroclinic storms during the Viking global dust event.

The 2001 global dust storm was unique in that it began around the southern hemisphere vernal equinox much earlier than previously noted global dust events. Generally, perihelion season (L_s 220-270°) shows a high degree of interannual variability in atmospheric temperature and opacity, associated with dust storms (Smith 2003). The 2001 global dust storm caused lower daytime surface and atmospheric temperatures well after the storm was over. Bright dust from the storm caused increases in surface albedo in the southern hemisphere (Cantor 2005; Strausberg et al. 2005). Nighttime surface and atmospheric temperatures were only minimally affected by the storm. Months after the storm's decay, its effects were still evident (Cantor 2003). Smith (2003) noted differences in visible albedo and daytime surface temperatures caused by the storm, which implies that the time scale for redistribution of the excess surface dust left by the storm is about one Martian year. This may be a significant factor in why global dust storms do not occur every year. While MGS has increased our observational database of global dust storms, it has not been able to directly measure the circulation patterns associated with it. However, we can use models (GCMs in particular) to simulate the MGS observations and then infer the circulation from them.

The CO_2 cycle is important on Mars because CO_2 is the main atmospheric gas. CO_2 exists in both the vapor and ice phases, and it is estimated that 30% of the atmosphere takes part in the CO_2 cycle (James et al. 1992). During the winter, CO_2

temperatures in the polar regions cool off enough that CO_2 condenses. The condensation process releases latent heat, providing a major energy source. The condensed CO_2 sublimes during the spring and summer in response to higher insolation, leading to the seasonal variation in the polar caps and the sublimation and condensation/deposition of CO_2, which also play a role in dust lifting centers (as discussed above). The Viking Landers detected surface pressure variations over the course of several Martian years (Fig. 3). This variation is semiannual, because while one cap grows, the other recedes. The maximum surface pressures are at the perihelion season (southern summer) while the lowest pressures are observed in northern spring.

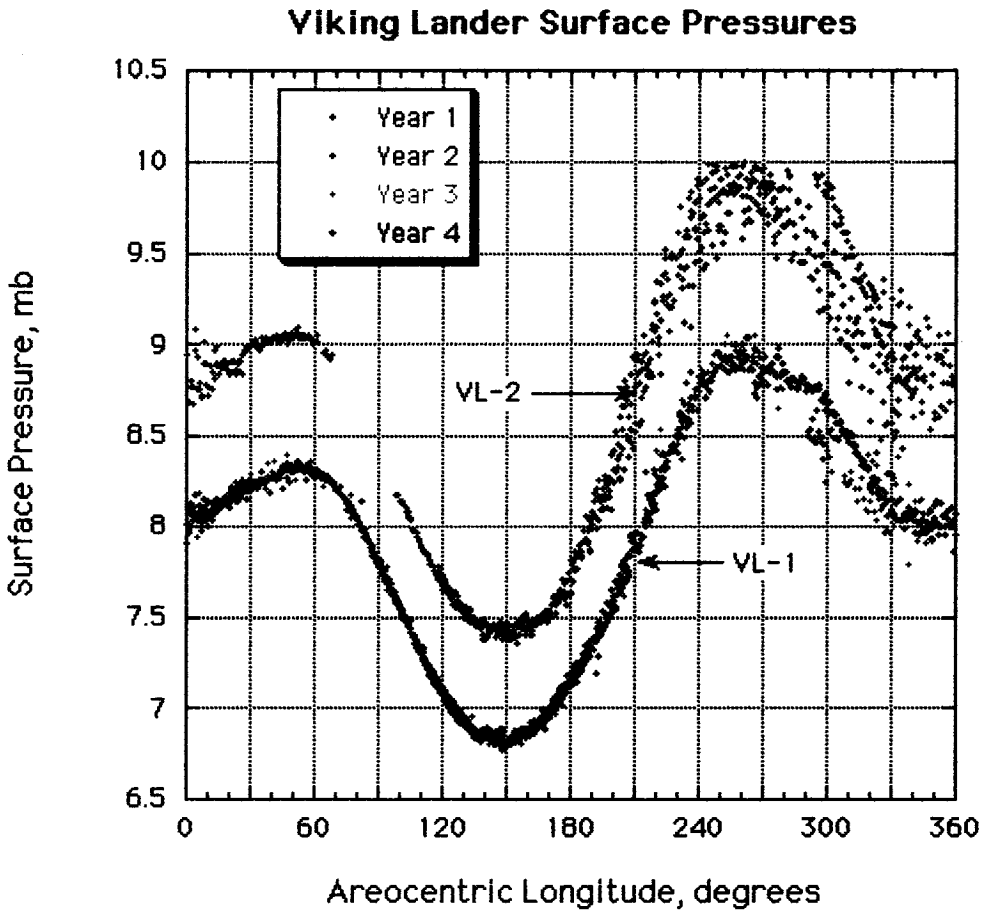

Fig. 3. Seasonal variation in surface pressure from Viking Lander observations over several Martian years. Highest pressures correspond to the perihelion season (near L_s 270°) while the lowest pressures occur in aphelion season (near L_s 90°).

Although Mars has no oceans, it does have a hydrological cycle. Fig. 4 shows the TES observations of column water vapor and cloud abundance. As the north polar seasonal CO_2 ice cap retreats it eventually disappears and exposes an underlying water ice cap. This residual cap absorbs sunlight and water therefore sublimes into the atmosphere. This is the main source of atmospheric water vapor. The peak abundance of ~ 100 precipitable microns (p-μm) occurs during mid summer. This water is transported into the southern hemisphere where some of it is deposited on the winter CO_2 ice cap. During southern spring this water is then re-released into the atmosphere and most of it is

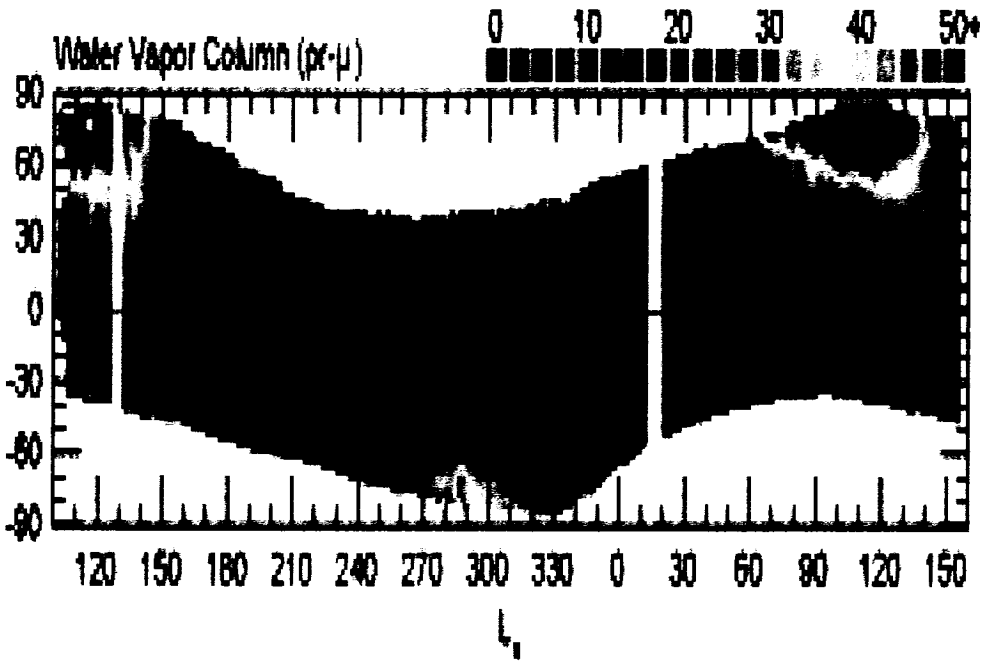

Fig. 4. Water vapor column abundance taken from Smith et al. (2001). The highest areas of water vapor abundance (shown in red) occur in the polar regions in their respective summer seasons.

transported back to the north cap closing the water cycle (Richardson and Wilson 2002). Although the radiative effects of water vapor and clouds are small, and the release of latent heat is insignificant because of the small abundances, the condensation of water vapor onto airborne dust grains may hasten the removal of dust from the atmosphere.

The coupling of the water and CO_2 cycles has many possible pathways that have yet to be explored. For example, the condensation of water onto CO_2 frost can alter its albedo and emissivity, the fundamental parameters that control the phase and amplitude of the CO_2 cycle. Variations in the CO_2 cycle can also affect the water cycle. It does appear that at least in one year, the residual south CO_2 ice completely disappeared and exposed an underlying water ice cap that served as a source of atmospheric water vapor (Barker 1971, Jakosky and Barker 1984). Recent MGS and Mars Express observations strongly suggest that the south residual cap is very thin (< 10 m) and may disappear on multiannual time scales (Malin et al. 2001; Smith et al. 2001). Studies of the coupling between the dust, water, and CO_2 cycles are just beginning. In this thesis, we ignore this coupling but recognize its potential importance.

2.5 General Circulation

Fig. 5 depicts our present understanding of the general circulation on Mars. Like Earth, the zonally averaged mean meridional circulation on Mars is dominated by a Hadley circulation. Unlike Earth, however, it is driven by radiative heating and cooling rather than latent heat release (Zurek et al. 1992). At the equinoxes, two symmetric Hadley cells develop and share a common rising branch near the equator, whereas at the

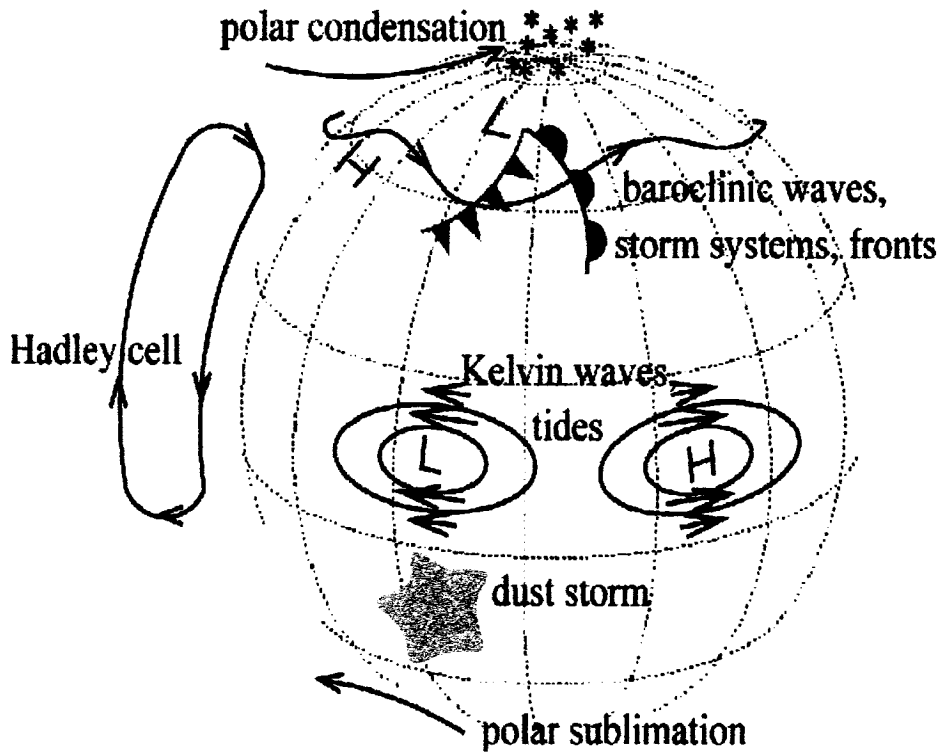

Fig. 5. The current understanding of the general circulation on Mars involves many different factors including polar sublimation, condensation, tides, and dust storms.

solstices, one cross-equatorial Hadley cell exists, with the rising branch in the summer hemisphere. The intensity of the Hadley circulation varies seasonally and with dust loading. It is strongest at the solstices and weakest at the equinoxes. Models suggest that the Hadley circulation is strongest at northern winter solstice when Mars is near perihelion. Peak mass fluxes at this season are on the order of 30-50 x 10^8 kg s^{-1} (Haberle et al. 1993). However, they are also very sensitive to the atmospheric dust loading. Dust intensifies the Hadley circulation because of the increased absorption of solar radiation and can easily double or triple its strength depending on how much is

present (Haberle et al. 1982). This relationship clearly points to a positive feedback between dust loading and the strength of the circulation.

Zonal mean easterlies dominate the tropics at all seasons, in the summer hemisphere at the solstices, and at middle and high latitudes during equinoxes (Zurek et al. 1992). Westerly jet streams exist in the winter hemisphere, formed by the strong difference in heating with respect to latitude. Based on observed temperatures and using the thermal wind relationship, peak winds of 100 m s^{-1} are expected (Conrath et al. 2000). Because horizontal wind speed tends to increase with height, the higher the dust is raised, the farther it is likely to go (Kahn et al. 1992). Also, eastward-propagating disturbances of high and low-pressure systems develop in these baroclinically unstable regions. Viking data revealed the presence of these baroclinic disturbances, and showed that they have wind and pressure patterns and timescales consistent with disturbances seen on Earth (Zurek et al. 1992). Generally, pressure decreases are accompanied by warming temperatures and southerly winds, followed by rising pressure falling temperatures and northerly winds. This is the classic signature of baroclinic eddies. However, unlike Earth the Martian baroclinic eddies complete disappear during summer as the temperature gradients needed to generate them are greatly reduced.

Forced oscillations, consisting of stationary waves and thermal tides, are a major influence on Martian weather and are a factor in the heat distribution in the atmosphere. They occur in the Martian atmosphere in response to the daily cycle of the sun and spatial differences in topography and heating (Banfield et al. 2003). Atmospheric thermal tides are extremely important in the Martian atmosphere due to the rapid response of the

atmosphere to radiative heating. These tides have temperature and velocity variations that grow with height as the air density decreases, which can therefore alter circulation patterns. The two most important components are the diurnal and semidiurnal tides. The diurnal tide has short vertical wavelengths (< 5 km) and can propagate vertically in the tropics (Zurek 1976). The semidiurnal tide has very long vertical wavelengths (> 40 km) and its dominant mode is expressed between +/- 60° latitude (Bridger and Murphy 1998). Both components are sensitive to dust loading; the diurnal tide because of its effect on diurnal surface temperature variations, and the semidiurnal tide because of its long vertical wavelength. This latter characteristic has been used to infer the global dust loading (Zurek and Leovy 1981).

A complicating factor regarding the thermal tides is excitation of non-classical modes. Longitudinal variations in topography and/or dust loading can excite eastward propagating tides as opposed to the classical westward propagating (sun-synchronous) tides (Wilson and Hamilton 1996). The interference of these two tides can increase or decrease the total tidal signature at any given point. Zurek and Leovy (1981) suggested that this interference effect was responsible for the dropout of the diurnal tide that was observed in one of the two global dust storms of 1977.

Stationary waves are large-scale disturbances in the atmosphere that are generated by zonally asymmetric forcing and atmospheric instabilities due to the lifting of air over varying topography and it's associated thermal forcing. Variations in surface temperatures due to albedo and thermal inertia differences may also create thermal continents, which may provide conditions favorable to generating stationary waves

(Zurek et al. 1992). Stationary waves are described using their zonal wavenumber (s), with s = 1 indicating that only one zonal wave exists around the globe.

Stationary waves may influence the stability of the atmosphere by enhancing the formation and development of disturbances at certain longitudes, but hindering them at other longitudes (Hollingsworth et al. 1996). Among other things, the position of a stationary wave could determine wind flows, such as whether winds will flow upslope or downslope. This is particularly important when considering dust lifting. Downslope flow may produce strong subsidence, thereby inhibiting Martian air from effectively rising, whereas an upslope situation would better allow dust to rise to greater heights. Using TES data, Banfield et al. (2004) found s = 1 stationary waves with significant amplitude that extended to the poles. This indicates that the stationary waves carry warmer equatorial air poleward. The heat transfer and forced topographical flow associated with stationary waves therefore alter weather events, and could possibly influence the formation of global dust storms.

2.6 Local/Regional Circulations

Although Mars has no oceans, spatial variations in thermal inertia and/or albedo cause regional circulations due to differences in surface thermal heat capacity and albedo (Zurek et al. 1992). For example, a low albedo surface may absorb more radiation than an adjacent high-albedo region, triggering a thermally direct circulation with rising air over the low albedo region and subsidence over the high albedo area. Large-scale sloping terrain affects the steady and diurnally varying wind and temperature fields,

especially near the surface (Blumsack 1971; Blumsack et al. 1973; Ye et al. 1990). Strong surface heating during the day results in buoyancy forces having an upslope wind component, while slope flow is downward at night (Zurek et al. 1992).

Unlike Earth, the seasonal condensation and sublimation of the ice caps represents a significant fraction of the total atmospheric mass (Zurek et al. 1992). While the vertically integrated velocity of this condensation flow is relatively small (~ 1 m s^{-1}), it can have a significant effect on surface winds near the edge of the polar cap (Haberle et al. 1979). A cap edge circulation may develop as colder temperatures over the ice caps (fixed at the CO_2 frost point, ~150 K) may be adjacent to much warmer ground (Haberle et al. 1979; Siili et al. 1997). These temperature gradients cause strong pressure differences that drive strong local wind patterns. These mesoscale factors create conditions favorable for strong winds, and therefore for dust to be lifted.

3. DUST IN THE MARTIAN ATMOPSHERE

3.1 Previous Observations of Martian Global Dust Storms

3.1.1 Telescopic

Astronomers have viewed dust storms for centuries, but only from Earth-based telescopes. Temporal coverage of Mars has been sporadic due to the large synodic period (time it takes to return to the same spot) and because of the large eccentricity of its orbit. More importantly, the apparent size of Mars (as seen form Earth) varies considerably in a 15-17 year cycle (Kahn et al. 1992). Optimal conditions for telescopic observations occur when Mars is at both opposition and perihelion. H. Flaugergues and later G.V. Schiaparelli both observed yellow clouds and veils in the 18^{th} and 19^{th} centuries. Antoniadi (1930) determined these yellow hazes to be dust clouds and reported large obscurations in dust patterns on Mars in 1877, 1892, 1909, and 1924. Due to changing albedo patterns, McLaughlin (1954) speculated the existence of windblown dust. Slipher (1962) also noticed an infrequency and natural variability of the presence of dust clouds. The first global dust storm to be well-documented occurred in 1956, and numerous astronomers and photographers followed the storm for several months and collected telescopic observations. These observations brought numerous discoveries regarding global dust storms such as their temporal irregularity, their preferred occurrence during the perihelion season. Telescopic studies also revealed that global dust storms usually originated in the southern hemisphere and grew first longitudinally then latitudinally. Further inspection revealed that dust storms usually become global events in around two weeks and last for several months, while significantly altering the surface albedo.

3.1.2 Spacecraft

The first spacecraft observations of a Martian global dust storm came in the 1970's with the Mariner 9 spacecraft. Mariner 9 arrived just after perihelion (L_s 293°) in November 1971 and witnessed the decay stage of a global dust storm. This global dust storm was, at the time the most severe dust storm ever seen. Surface detail was nearly impossible to recognize as atmospheric dust obscured Mariner 9's view (Kahn et al. 1992). For example, Greeley et al. (1992) noted that the 1971 global dust storm raised dust to over 60 km in the atmosphere, by far exceeding anything ever observed on earth. Anderson and Leovy (1978) observed that clearing occurred first at high latitudes and slower at the lower latitudes. This storm demonstrated how widespread and long-lived Martian dust storms could be, and also how these storms decay.

Mariner 9 utilized infrared technology that could estimate dust opacities using the depth of the observed 9-μm absorption (Martin and James 1989). The onboard infrared spectrometer used a silicate band using the range of 8-12 μm. Thermal contrasts between the Martian dust haze and the surface could be measured depending on the amount of suspended dust present (Kahn et al. 1992). From this technique, estimated global-averaged dust opacities during this time period were 0.32, with individual measurements ranging from 0-1.5 (Fenton et al. 1997). Infrared data from Mariner 9 also revealed the alteration of the atmospheric thermal structure and circulation due to the solar heating of the dust (Zurek 1982). The opacity variations within this band seen in the decay stage of the 1971 global dust storm and several regional storms afterward demonstrate the diminished thermal effects of the dust (Kahn et al. 1992; Leovy et al. 1973).

The Viking orbiters and landers observed two global dust storms in 1977 (1977a and 1977b) and retrieved dust opacities, wind measurements and pressure data that yielded information regarding the formation and atmospheric response to dust storms (Zurek and Leovy 1981). The limited field-of-view of the camera and the moderately inclined elliptical orbits prevented global coverage of the events (Briggs et al. 1979). However, each Viking Lander carried a camera that viewed the Sun as well as the local environment. By observing the Sun, line-of-sight extinction opacities were retrieved (Pollack et al. 1977). Viking images of the onset of the 1977a storm show large, organized dust storms in the Claritas/Syria Planum region. Similar images from the 1977b storm indicate initial develop in the Hellas region (Fig. 1). These observations indicate that global dust storms may tend to form in specific regions that are preferable to dust lifting. Viking Landers also recovered dust opacities from the first storm that began at L_s 205° and also the second storm (L_s 274°). Data showed dust opacity ranging from 0.5 to 9 over the landers, and large variations in the quantity and distribution of airborne dust. Wind velocities at the landers never exceeded 30 m s^{-1} and no surface material was observed to have moved, although brightness and contrast were altered after each storm, presumably due to dust settling from the atmosphere (Greeley et al. 1992). Finally, Viking Lander surface pressure data indicated an increase in the semi-diurnal tidal amplitudes during both global dust storms, due to the daily heating of a widespread dust haze. The observed tidal amplitudes compare well with the Zurek (1976) estimates of opacity levels required to produce such a change in the tidal amplitude. Semi-diurnal

tidal variations also increased at the end of the Viking mission, possibly indicating another global dust storm.

3.1.3 Summary

Mars spacecraft have observed the planet for the past 40 years, although it has been seen from Earth for centuries. Telescopic data revealed the presence of dust, and the variable nature of atmospheric dust and infrequent occurrence of global dust storms. Spacecraft observations have given a closer look at the effects of large dust loading. Seasonal trends, movement, opacity and other atmospheric data revealed that during major dust storms, the diurnal ground or near-surface temperature variation decreases, reflecting the decrease in surface heating and heating effects of airborne dust (Ryan and Henry 1979). As a consequence, these observations have led to the further development of theories regarding dust storms. Due to the irregular occurrences of global dust events and the small number of Mars missions, much uncertainty remains on the mechanisms of their growth and decay. From our limited observations (Table 1), it is clear that global dust storms are rare events that have been observed only sporadically. An observational bias exists due to the varying distance from Earth and the existence of spacecraft missions (Zurek 1982). For example, Viking observed two global dust storms that may not have been observed if not for the spacecraft. Therefore, it may be safe to assume that other global dust storms have occurred, but no observations exist because either telescopic observations were difficult due to Mars' position in orbit/distance from Earth or no spacecraft viewed the event. From all past observations and records, Martin and

Zurek (1993) concluded that large dust storms may occur during any given Martian year, but the probability of a global dust storm was one-in-three.

3.2 Theories of Global Dust Storms

3.2.1 Discussion of Theories

Zurek et al. (1992) explain that due to the strong influence of airborne dust on atmospheric temperatures, feedback mechanisms exist between to the absorbed solar radiation and the mass movement of air. Dust heating affects the temperatures, and therefore pressure patterns and winds. By altering the atmosphere's static stability, suspended dust affects the transfer of sensible heat from the surface, and possibly the strength of near-surface winds. Generally, most theories concerning the creation of large dust storms involve a positive feedback due to dust lifting and the direct heating of airborne dust particles. Specifically, strong winds raise the dust from the surface, radiative heating of the suspended dust lead to stronger surface wind speeds, raising more dust. A negative feedback may also develop since the increase in suspended dust heats up the higher levels of the atmosphere, leading to higher static stabilities. This atmospheric situation may act as a cap by preventing the upward movement of dust. Both feedbacks may play a critical role in the life cycle of global dust storms. However, the factors that shut down global dust storms remain unknown.

The dusty hurricane theory developed by Gierasch and Goody (1973) compares Martian global dust storms to hurricanes on Earth. The main difference between global dust storms and hurricanes is that the direct heating of suspended dust is the main source

of the storm's energy. This is analogous to the latent heat of condensation that fuels hurricanes. Storms begin with little rotation and light surface winds, but amplify when air converges to a dusty center and rises, creating a surface low-pressure that pulls in more air at low levels. Surface winds increase lifting of dust, and at upper levels, dust flows outward from the center. Observations have shown that dust storms do not have the spiral structure of hurricanes, and that very few dust clouds show any rotation. Also, this theory implies that dust storms should have a strong diurnal variation, as local solar heating is a major driving mechanism.

Leovy et al. (1973) suggested that when dust opacity reaches a critical threshold, winds strong enough to lift dust could be produced by the superposition of a varying Hadley cell, tidal winds, and global-scale topographic flow. The upsurge of dust prior to reaching the critical level is mainly through local storms that develop through mesoscale circulations involving the retreating south polar cap and CO_2 outflow winds. This is achieved best in southern spring and summer when the thermally direct Hadley circulation and tidal are winds enhanced by increased insolation near perihelion. It is also the time when tidal winds are strongest in the subtropics, due to the seasonal changes in dust opacity. Due to these factors, if dust is spread into the subtropics, the Hadley circulation strengthens and moves dust northward into the northern hemisphere.

Haberle et al. (1982) examined the effects of dust loading on the strength of the Hadley circulation. In the perihelion season, dust loading increases in the southern hemisphere, leading to a stronger Hadley circulation through a positive feedback. In the northward branch of the Hadley cell, how far north the dust goes depends on the

magnitude of the diabatic heating, which relates to the amount of dust raised initially.

Schneider (1983) proposed that dust storm conditions might develop without tidal and topographic winds. He conducted simulations in which maximum solar insolation was offset from the equator at latitude Θ_0. Results indicated that when the total diabatic forcing (Q) was less than the critical value of diabatic forcing (Q_c), the Hadley cell remained in the summer hemisphere. When $Q = Q_c$, the Hadley cell extended up to the equator, and when $Q > Q_c$, the Hadley cell extended into the high latitudes in the winter hemisphere.

The free-mode triggering theory by Tillman (1988) is a variation of the Leovy et al. (1973) mechanism involving an enhanced atmospheric circulation. Transient events associated with resonant excitation of Kelvin wave normal modes cause daily pressure variations at the surface that last several sols, but are generally repeatable on an annual basis. Analysis of three global dust events revealed an intensification of the normal-mode, global oscillations that may be involved in triggering large dust storms. This theory suggests that unique circulation patterns can either promote or inhibit the formation of global dust storms.

3.2.2 Summary

Mars has dust on the surface and in the atmosphere, and the distribution, movement and redistribution of dust on Mars illustrate circulation patterns. Generally, in a time span of a few weeks, dust is lifted and distributed around the entire planet (Kahn et al. 1992). Observed global dust storms have all begun in two main regions: Hellas Basin

or Syria Planum/Solis Planum, and all of the observed dust storms have occurred within 50° of perihelion (Kahn et al. 1992), except for the 2001 global dust storm. Although the origin of global dust storms is not well understood, the presence of strong winds causes the lofting of dust. These strong winds may be caused by thermal gradients due to the proximity of the ice cap edge (Leovy et al. 1973), large topographical variations (Siili et al. 1997), or fronts associated with baroclinic disturbances (Leovy et al. 1973). Mainly, the theories on the initiation of global dust storms involve feedback mechanisms between dust lifting, static stability, and meridional and topographical circulations. Numerical studies using general circulation models have shown that such feedbacks exist, and may play a significant role in the development of global dust storms (Haberle et al. 1982).

3.3 Dust Lifting and Fallout Mechanisms

3.3.1 Dust Devils

In order to lift dust from the surface, there must be winds strong enough to move the dust and a supply of loose particles and (Greeley et al. 1992). Dust devils are visible vortices containing dust that are a common method of dust lifting on Mars, even when surface winds are light (Ryan 1964). Pathfinder lander observations showed that these vortices have low-pressure centers. Thomas and Gierasch (1985) examined data from the Viking spacecraft which observed nearly 100 Martian dust devils. They determined that dust devils typically extend from 1-3 km in the vertical and vary from about 1 - 500 meters in width. Ryan and Lucich (1983) observed the vortices had peak wind gusts exceeding 25 m s^{-1}, and estimated that wind gusts can reach as high as 44 m s^{-1}. Dust

devils occur in all seasons, but are most frequent during the afternoon in the spring and summer seasons, when the surface heat flux is large (Kahn et al. 1992). Although no dust devils have been observed to lead to the formation of global dust storms, they significantly contribute to the background dust haze on Mars (Zurek et al. 1992).

3.3.2 Saltation

Strong winds and convection lift dust from the surface, but the process of saltation is mainly responsible for the creation of dust clouds and major dust storms. Bagnold (1941) first examined this process using wind tunnel experiments to make quantitative predictions about sand movement and accumulation in the Libyan deserts on Earth. Generally, horizontal surface winds create a surface shear stress (τ), which is a function of the surface friction speed (u^*) and the fluid density (ρ). The surface stress is given by:

$$\tau = \rho u^{*2}.$$

Wind tunnel experiments by Greeley et al. (1980) used Mars-like surface pressures to calculate the minimum wind speed necessary to set particles into motion. They found that 100 μm diameter particles have the minimum surface stress values and are therefore the most easily moved by the wind. Pollack et al. (1976) further showed that it would take wind speeds of at least 50 m s^{-1} to lift these 100 μm dust particles. Saltation acts as high wind speeds (between 50 -100 m s^{-1}) lift sand particles that bounce along the surface, and collide with other particles (Kahn et al. 1992). If the particles have enough kinetic energy, the collisions at the surface cause other, smaller dust particles to be lifted (Greeley et al. 1992). This process occurs in rapid, repeated cycles, and forces the lifting

of larger amounts of dust. Although 100 μm particles are the most easily moved, they are too large to remain suspended. They instead return to the surface and kick up smaller particles. Pollack et al. (1979) determined using simulations that suspended dust particles are ~2 μm in diameter, therefore proving that saltation is a major dust lifting mechanism. The saltation process is the major lifting mechanism responsible for large dust events like the 2001 global dust storm.

3.3.3 Gravitational Settling

Dust is removed from the atmosphere primarily through gravitational setting of airborne particles, and spacecraft observations have allowed the size, vertical distribution and time scale of removal to be estimated (Greeley et al. 1992). The terminal velocity (w*) for a spherical particle is given by Stokes-Cunningham relationship, written as:

$$w^* = -(\rho_p g d^2/18\eta)\,(1+2(\lambda/d)),$$

where ρ_p is the dust particle density, g is the gravitational acceleration, d is the particle diameter, η is the molecular viscosity, and λ is the molecular mean free path. Although atmospheric dust may be well-mixed, 1 to 10 μm particles dominate the Martian atmosphere, with particles having an effective radius of 2.5 μm being the most common (Toon et al. 1977). Using the Stokes-Cunningham equation, a 1 μm particle at 1 mb falls at a speed of 2.2×10^{-5} m s^{-1} and a 10-μm particle would fall at 6.0×10^{-3} m s^{-1}. Based on the 1977 dust storms, Pollack et al. (1979) estimated an average sedimentation rate of ~2×10^{-3} g cm^{-2} yr^{-1}.

Dust fallout occurs in all locations around the planet, although much of this dust may be deposited in the north polar region due to the enhanced effect of dust acting as condensation nuclei for water and CO_2 (Greeley et al. 1992). The exact location of sedimentation also affects surface albedo. Wells et al. (1984) showed that small amounts of dust are sufficient to alter surface albedo features, and that the deposition of 10^{-4} g cm^{-2} of bright dust should increase the albedo by several tens of percent. Examination of the 2001 global dust storm by Cantor (2005) showed surface albedo values increasing by 1 to 6 % around the planet.

4 MARS GLOBAL SURVEYOR MISSION

4.1 Overview

Launched in November of 1996, the MGS satellite's mission was to collect scientific data to expand the knowledge of Mars. MGS was designed to closer examine the surface features, atmosphere, and magnetic properties of Mars, all serving to build a comprehensive dataset to aid in planning future missions. From this satellite data, scientists have not only been able to better understand Mars, but they have also learned a great deal about Earth via comparison (Albee 2001). MGS began mapping the planet in April 1999, from a nearly circular, polar orbit that circles the planet 12 times per day and returns to same location every 89 orbits (about one week). The orbit is sun-synchronous, so that the spacecraft passes overhead at 2:00 local time (either pm or am), giving a constant lighting angle (Smith et al. 2001). This orbital configuration allows regular coverage of the planet. MGS was designed to operate for at least one Martian year, but has been observing the planet for over three full Martian years.

4.2 Payload

Data were collected during the 2001 global dust storm on Mars by MGS. The satellite took observations for the entire lifecycle of this global dust storm, yielding more information about global dust storms than ever before. The instruments on board collected satellite images, terrain elevation, local temperature data, pressure, and dust optical depth. MGS was designed to get continuous data using five separate instruments. The instruments of relevance to atmospheric research are: 1) the Mars Orbiter Laser

Altimeter (MOLA), used to determine topography; 2) the Thermal Emission Spectrometer (TES), collects temperature and dust information; 3) the Mars Orbiter Camera (MOC), gives low-resolution (~7 km) daily global maps and limited high-resolution (~ 2 m) images of the planet; 4) the Mars Horizon Sensor Assembly (MHSA), which provided temperature information over a deep region of the atmosphere (roughly 10-40 km). MHSA data are unique in that temperature data are gathered at four separate quadrants, with quadrant one being in the forward direction (with respect to the spacecraft velocity), two being aft, three being cross-track and to the right, and four being cross-track to the left. The cross-track quadrants provide local time-of-day variation of about three hours. Such data allowed inspection of wave disturbances that had time dependences.

4.3 Key Measurements for Present Work

For the purpose of examining the global dust storm and atmospheric data, several instruments' data were inspected in detail. The MOLA instrument bounces a laser signal off the planet's surface, and the duration of the pulse's flight is used to determine the elevation to within several meters (Smith et al. 2001). From these measurements, global topographic maps were created (Fig. 1). Knowing the topography of the planet allows better inspection and analysis of orographically-altered weather events and circulation systems.

Designed to inspect the mineralogy of Mars, TES can also study the atmosphere and can retrieve temperatures, pressures, and dust opacities (Christensen et al. 1992).

The TES instrument uses thermal infrared energy to determine the emissivity of a substance. Since molecules are selective emitters/absorbers that depart from a Planck blackbody (perfect emitter) distribution, one can deduce the type of molecule by the infrared waves it emits. That is, when light of a certain wavelength hits a particular molecule, the molecule starts vibrating and re-radiates at the same wavelength. The wavelengths that cause molecular vibrations occur in the infrared region, and since each molecule has its own characteristic frequency of vibration, the infrared light emitted by vibrating molecules can be used to identify them (Christensen et al. 1992). The infrared energy emitted by molecules is described in terms of radiance (measured in W m^{-2}), which is directly related to a substances' temperature. Christensen et al. (1992) further described that in order to make comparisons of emission from materials at different temperatures, the temperature effect must be removed. This is done by dividing the radiance spectrum of a selective emitter by that of a blackbody at the same temperature, yielding an emissivity spectrum. Therefore, emissivity data gathered by TES is a fraction describing the amount of energy from some material against the energy that would come from a blackbody at the same temperature. TES provides measurement in the infrared spectrum between 6 and 50 μm, and has a spatial resolution of around 3 km (Christensen et al. 1992, 2001). Since CO_2 has a strong absorption near 15 μm, examining the wavelength dependence of an observed radiance near the center of this absorption band yields information regarding the temperature of the atmosphere (Conrath et al. 2000; Smith et al. 2001). That is, thermal emission measurements estimate temperature as a function of atmospheric pressure level. The radiances near adsorption band center are

sensitive to the upper atmospheric levels, while those in the more nearly transparent band edges provide information on layers nearer the planetary surface (Conrath et al. 2000).

Our research uses the TES derived 2pm and 2am temperature fields at 0.5 mb, 3 mb, and the surface. By utilizing other absorption bands, the TES instrument can also retrieve dust, water vapor, and water ice information (Smith et al. 2000; Smith 2003; Pearl et al. 2001). For dust, TES collected 9-micron opacity measurements, which gives a clear indication of where dust was present and where it was lifted. Dust opacity is obtained by TES only once per sol at 2pm, as the surface needs to be warm enough in order to have sufficient thermal contrast and a clear emissivity spectrum. Therefore, it is common to have missing dust opacity data over the polar caps.

MOC images consist of two continuous color images with a spatial resolution of about 7.5 km with near limb-to-limb coverage (Albee 2001). The MOC instrument provided high-resolution visible images of the planet, allowing surface and atmospheric features to be seen clearly, and also offered a limited view of the vertical extent of dust. MOC limb data shows the height of the dust haze reaching over 50 km during the 2001 global dust storm (Cantor 2005). With each pass around the planet, MOC provided an image 30° wide in longitude (MOC has a 140° field of view, so each image extend out to the limb). MOC uses two wide-angle cameras to obtain a red and blue image, and a narrow–angle camera for closer inspection (Malin 1992). MOC has a peak spatial resolution of 250 m , although the cameras can reduce the resolution to reduce the downlink time (Malin et al. 1992). MOC data mosaics, created by Malin Space Science Systems, provided a daily global color image for each day during the storm by combining

the images taken on each successive orbit (twelve images per day). The daily maps were constructed by connecting the images in the continuous strips on the dayside portion of each orbit. Any incomplete areas not covered by the MOC instrument were filled and manipulated using image software. These images do not provide a true synoptic picture, as each mosaic consists of 24 hours worth of images. However, MOC mosaics alone show dusty regions, transient disturbances, and topographic features with fine detail, and provide the necessary landscape for inspecting a global dust event. Red-filtered MOC images were preferred over color or blue-filter images so that dust would be the focus of attention, as opposed to water and CO_2 ice clouds. Dust clouds appear brighter than condensate clouds at red wavelengths, while condensate clouds are brighter at blue wavelengths (James et al. 1992). This is a result of a higher single scattering albedo and surface albedo in condensate clouds in the blue band pass (Cantor 2005).

The raw TES temperatures and dust information were binned into 9° longitude and 5° latitude bins for the purpose of graphical analysis. The TES temperatures were then overlaid on top of the MOC mosaic images. Although the MGS satellite covered the entire planet during each sol (making 12 passes, each covering 30° in longitude), it was quite common for several bins to initially have no value. The major reason is that TES has very limited coverage, with footprints only 3 km wide. MOC, on the other hand see much broader areas. The result is, for each MOC image strip, there could be significant structure in the temperature field that TES simply cannot register. In the case of missing data, a simple linear interpolation in latitude was used to fill in the gaps, so that all points

contained information. Dust maps were generated using 2 pm TES linearly interpolated dust opacity measurements, and these were also overlaid on the MOC mosaics.

5. ANALYSIS OF THE 2001 GLOBAL DUST STORM USING MGS DATA

5.1 Description of Event

A detailed description of the 2001 global dust storm is given by Cantor (2005). At L_s 180°, June 2001, the Martian atmosphere appeared similar to most years at the near-equinox season, with a well-defined southern cap and several dusty locations dispersed around the planet. Cantor (2005) explained that Seasonal trends from L_s 170°-185° are generally similar in all three Martian years observed by MGS (1999-2000, 2001-2002, and 2003-2004). The dustiest area at this time, confirmed by MGS measurements, was over the Hellas Basin, a large depression in the southern hemisphere stretching in latitude from ~ 30°S to 50°S, very near the edge of the seasonal CO_2 ice cap (Fig. 1). The year 2001 began to diverge from the situation the previous year when seven small dusty pulses (Fig. 6) from the cap boundary near the southwest edge of Hellas were observed to move northward (Cantor 2005). Several local dust storms also propagated into western Hellas along the western rim of Hellas (Strausberg et al. 2005). These pulses and local storms may have provided the energy that led to the first significant lifting center (Malin and Cantor 2003), thereby triggering the global dust event (Cantor 2005). At the same time, visible poleward pushes of dust began on the eastern side of the Hellas Basin (Fig. 7). At around L_s 185°, a well-defined lifting center developed in eastern Hellas, and then propagated northward and eastward. The newly-lifted dust steadily moved eastward to approximately – 60°W, where a new lifting center emerged south of Tharsis in the Claritas region. Malin and Cantor (2003) observed that dust was

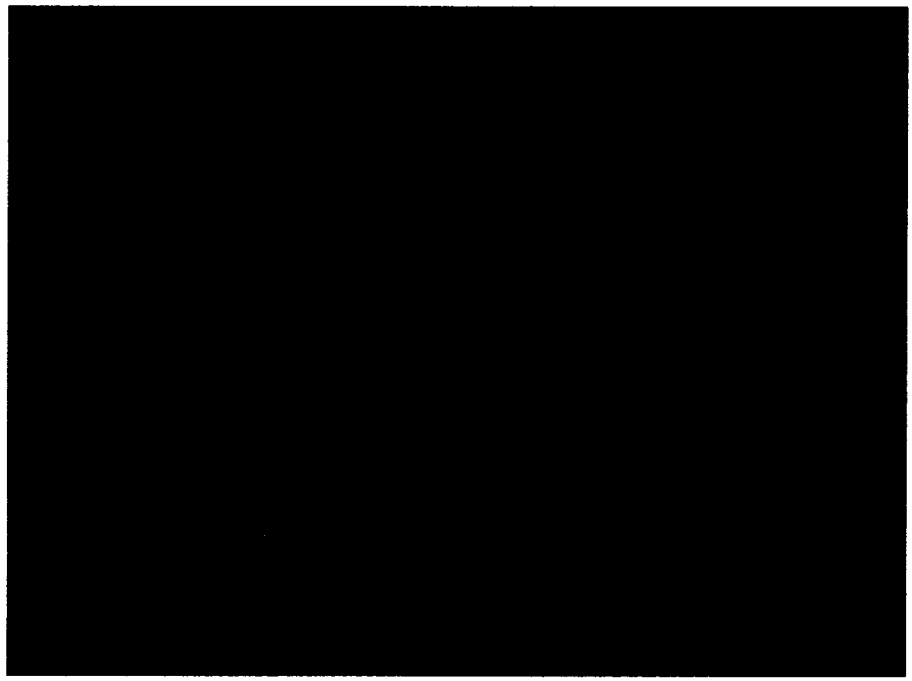

Fig. 6. Close-up MOC image of dust pulse moving from the southern cap edge. Image ranges from latitude 25° (top) -75°S and longitude 45° (left) -110°E.

Fig. 7. Close-up MOC image of dust moving over the southern cap edge. Image ranges from latitude 25° (top) -75°S and longitude 45° (left) -110°E.

lifted steadily here for 86 sols, and this location quickly became the dominant dust-lifting center by injecting dust that eventually spread around the planet. As the Claritas lifting center developed, rapid intensification began and global opacity values increased dramatically. The last areas to be affected by the dust were the longitudes surrounding the prime meridian (Fig. 1) and the northern hemisphere polar regions, as the polar vortex shielded these northernmost regions. Global opacities climbed steadily (from 0.1-1.5) from L_s 187° - L_s 215°, when the storm reached its peak. Opacities leveled above 1.0 for several weeks, then began slowly falling around L_s 220°. At L_s 240°, roughly 40 sols after the peak, the opacity levels of 0.6 were still more than three times the pre-storm values.

The 2001 global dust storm was not a single storm, but instead consisted of a series of local and regional storms, highlighted by the Hellas and Claritas storms (Cantor 2005). Also, the 2001 global dust storm occurred earlier in the dust storm season than previous global storms, yet still contained the necessary factors that allowed it to grow to the global scale. The development of this storm at the equinox season (near L_s 180°) has raised more questions about the essential driving mechanisms and properties that go into the development, growth, and decay of global dust storms. These include the need for strong solar insolation that produces a stronger circulation.

5.2 MOC Images

MOC mosaics analyzed in this thesis cover L_s 182° - L_s 205°: the onset, rapid development stage, and near-peak conditions of the storm. Fig. 8 shows a red-filtered

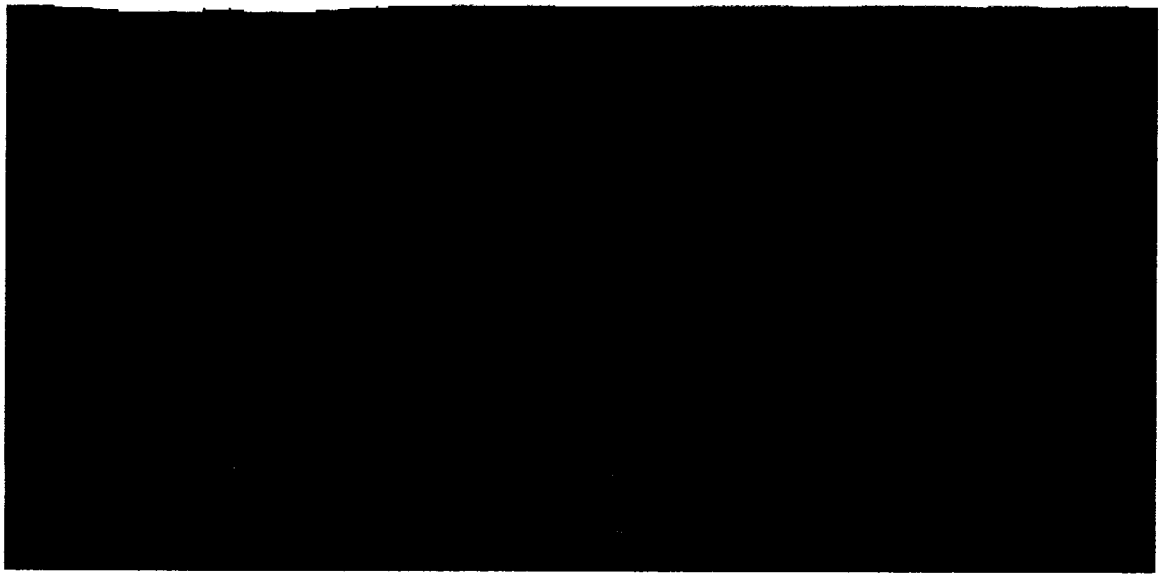

Fig. 8. Red-filtered MOC image of the entire planet at L_s 185.96°. The arrow points to eastern Hellas, where dust is being lifted. At this time, the dust has begun propagating northward and eastward. The south polar cap boundary is visible at ~65°S.

MOC image of the planet, taken at the beginning of the global dust event. Clearly visible is the south polar cap, which extends from the pole to about 65°S. Also, wave disturbances are noticed in the far northern hemisphere, as indicated by the oscillatory pattern. These systems propagate from west to east with timescales of several sols; this indicates baroclinic disturbances. The arrow points to the Hellas Basin, where the initial dust lifting began. At this time, dust has begun spreading eastward into the western hemisphere.

MGS MOC data clearly reveals the basic growth locations and propagation of the dust around the planet. Figs. 9, 10, and 11 show the condition of the storm at the onset, during the rapid-growth phase, and at near-peak conditions, respectively. At L_s 182° MOC shows a large amount of dust in the Hellas basin. Most dust is seen to be confined

to the western Hellas region near 45°S, 50°W. Slight lifting is noticed near Tharsis, although to a much lesser degree than seen in Hellas. At this point, dust is observed to propagate westward in southern mid-latitudes. Several sols later, at L_s 184, the main dust lifting center in Hellas has moved eastward towards the center of the basin, with only smaller, local storms visible elsewhere on the planet. A few sols later (Fig. 8), a large lifting center has organized on the eastern side of Hellas, becoming the first major lifting center of the soon-to-be-global event. Over the next few sols, dust is continuously lifted and caught up in the atmospheric circulation that moves the dust cloud eastward and northward. At L_s 188°, several dust clouds merge to create one large dusty area stretching from 75° to 135°W and from 10°N to 50°S. Also, a new lifting center is observed to the southwest of the Tharsis ridge. From L_s 188° to L_s 192°, the dust Lifting

Fig. 9. MOC mosaic from L_s 182.4°. Dust levels are highest in the Hellas Basin, and the South Polar seasonal ice cap is clearly visible.

Fig. 10. MOC mosaic from L_s 189.8. The storm is rapidly intensifying. Dust is clearly visible over the southern cap edge and in the western hemisphere.

Fig. 11. MOC mosaic from L_s 211.5°. Near the peak of the storm, surface features are extremely difficult to view. The arrow points to the faintly noticeable Tharsis volcanoes.

center south of Tharsis is rapidly growing, spreading dust all throughout the region. The Hellas region still shows lifting, and dust has spread in all directions. At this time, the meridional movement of dust equals the east-west movement. East of Hellas, dust is noticeably pushed over the southern seasonal cap. At L_s 192°, the main lifting center is now south of Tharsis, not in the Hellas Basin. This lifting center continues to lift dust until L_s 230°. The last areas to see increases of dust opacities are near the prime meridian, which are the furthest from the lifting centers. By L_s 195°, the entire planet is now enshrouded with dust, yet the upward movement of dust in Claritas indicates that more dust is being lifted. Over the next months, dust is observed to lift in the Claritas area until the peak global opacities are reached (L_s 212°).

5.3 TES Opacities and Temperature

The TES instrument provided both temperature and dust information essential for examining the storm. Fig. 12 shows how TES information alone clearly shows the development of the global dust storm. Before the storm's onset, global opacities were low and 0.5 mb temperatures were consistently cooler (by ~75 K) than the surface temperatures. This is expected because with little dust present, temperature falls off quickly with height. Once dust lifting began, the opacity levels quickly rose, which led the atmosphere to become more isothermal. In general, TES dust data covers the region between 60°N and 60°S, as less confidence is given to data seen in the polar regions due to the extremely cold conditions.

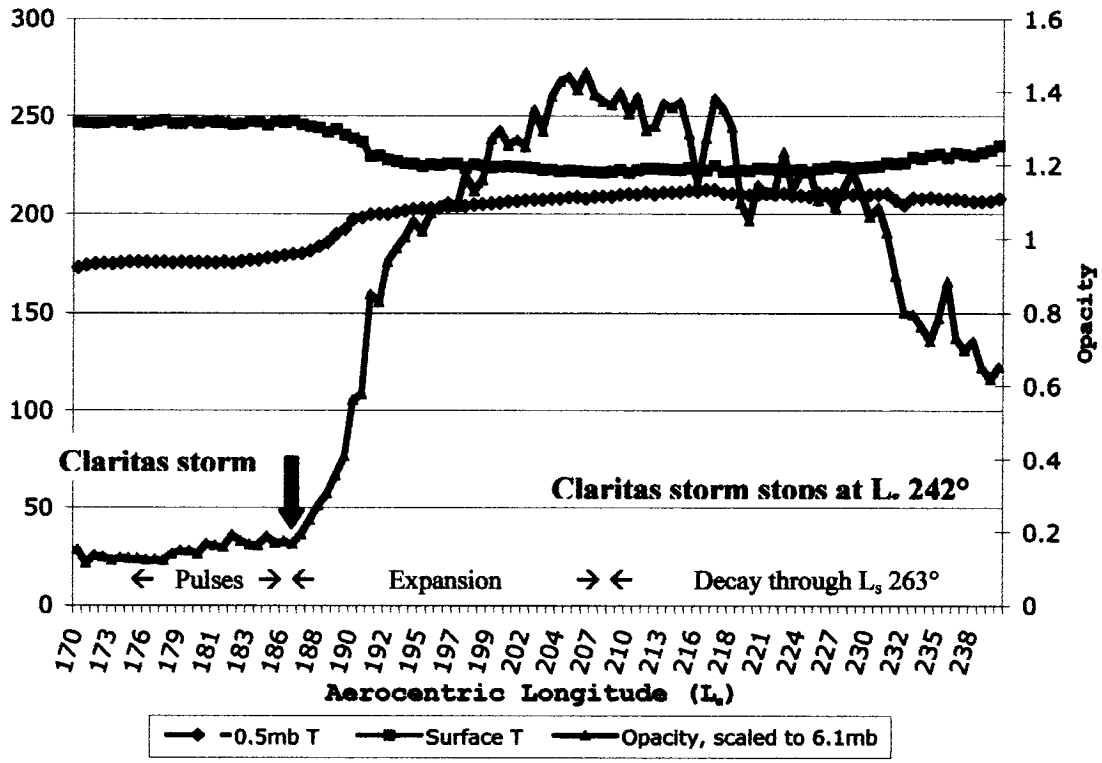

Fig. 12. Global area-weighted 0.5 mb and surface temperatures (K), and global, area-weighted dust opacity. Global opacity levels increase around L_s 190°. After that, 0.5 mb temperatures increase while surface temperatures decrease due to the large amount of atmospheric dust. Each tick marks on the x-axis represents 10 sols.

5.4 Overlays

The TES 9-micron opacities and 0.5 mb daily averaged temperatures superimposed onto MOC images (Figs. 13 – 18) give an excellent view of the storm's development. Figs. 13 shows the situation at L_s 181°, just before the onset of the storm. At this time, the equinox season is quite benign, with the temperature distribution appearing symmetrical with respect to the equator. Temperatures are at or above 180 K from 40°N – 40°S. The southwestern part of Hellas, a visibly dusty area has temperatures 10 K warmer than the surroundings. Opacities of at least 0.3 are seen in

the Hellas basin, and TES confirms the dustiest area (opacity of 0.45) to be north of Hellas between the equator and 30°S. Regions of opacity of at least 0.25 are consistently seen near the southern cap edge, where strong temperature gradients exist. Dust opacities of 0.35 exist to the northeast of Olympus Mons, although the rest of the northern hemisphere shows relatively low opacities ranging from 0.10-0.20.

Conditions during the rapid onset around L_s 186° are shown in Fig. 14. Here, opacity values are extending further in all directions, but especially longitudinally. Opacities levels have more than doubled along the equator, raising from 0.2 to 0.5. Dust opacities have increased in the Claritas region and other areas near Tharsis, signaling that other, independent dust lifting is occurring.

Fig. 15 shows the planet about 17 sols later. The lifting center in Hellas has expanded outward and dust levels have sharply increased, yet the dust does not yet enshroud the planet. At L_s 191°, the storm's growth and seasonal changes are more apparent. The strong latitudinal temperature differences (60 K) between 30-75°N and 50-

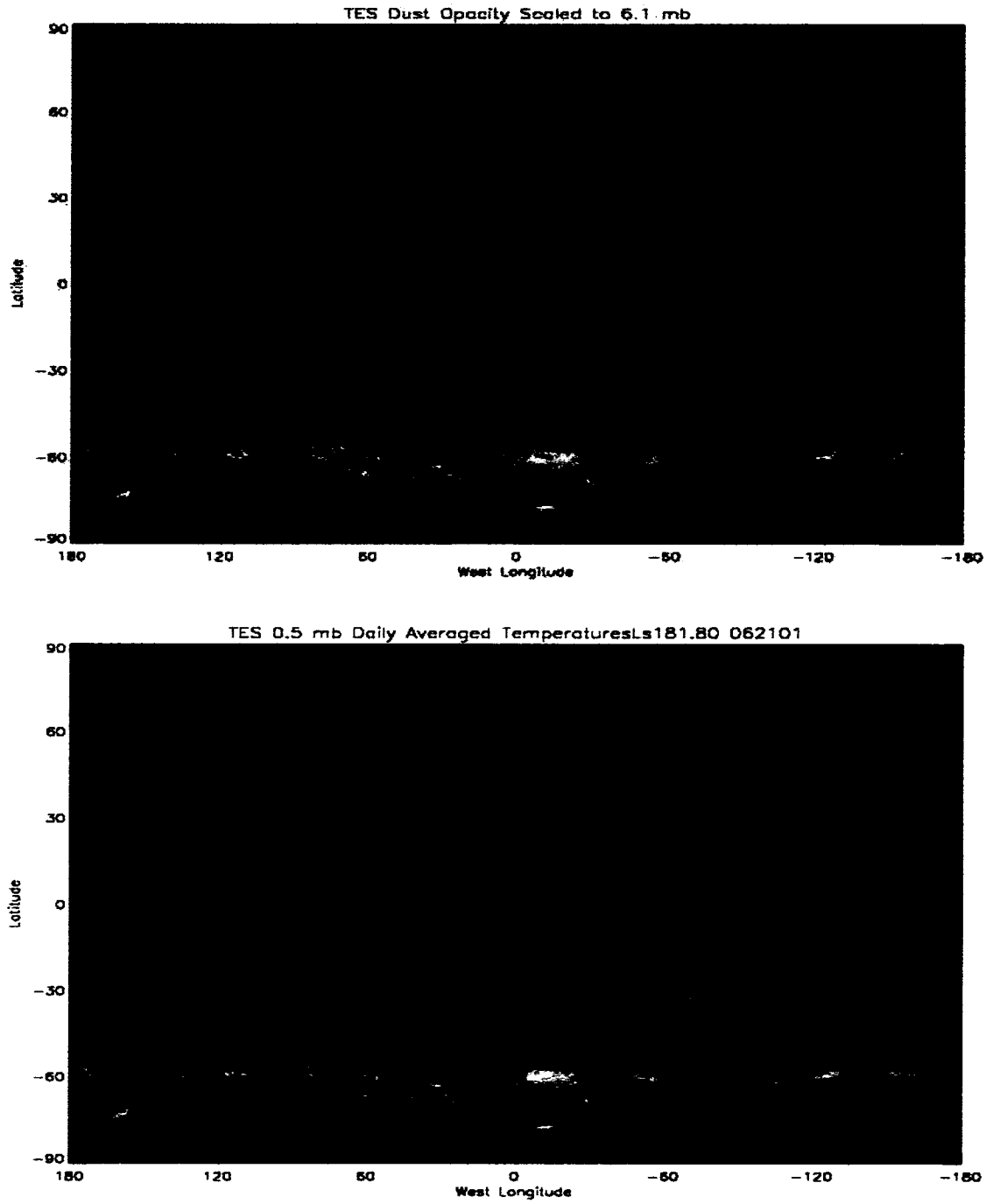

Fig. 13. MOC Image from L_s 181.8° with overlaid TES opacity (top panel) and TES 0.5 mb temperatures (K) (bottom panel). The dustiest region is in northeastern Hellas, although values of 0.2 values are common along the southern cap edge. At the equinox season, the atmospheric circulation is symmetrical with polar vortices present in both hemispheres. The tropics show little variation in temperatures.

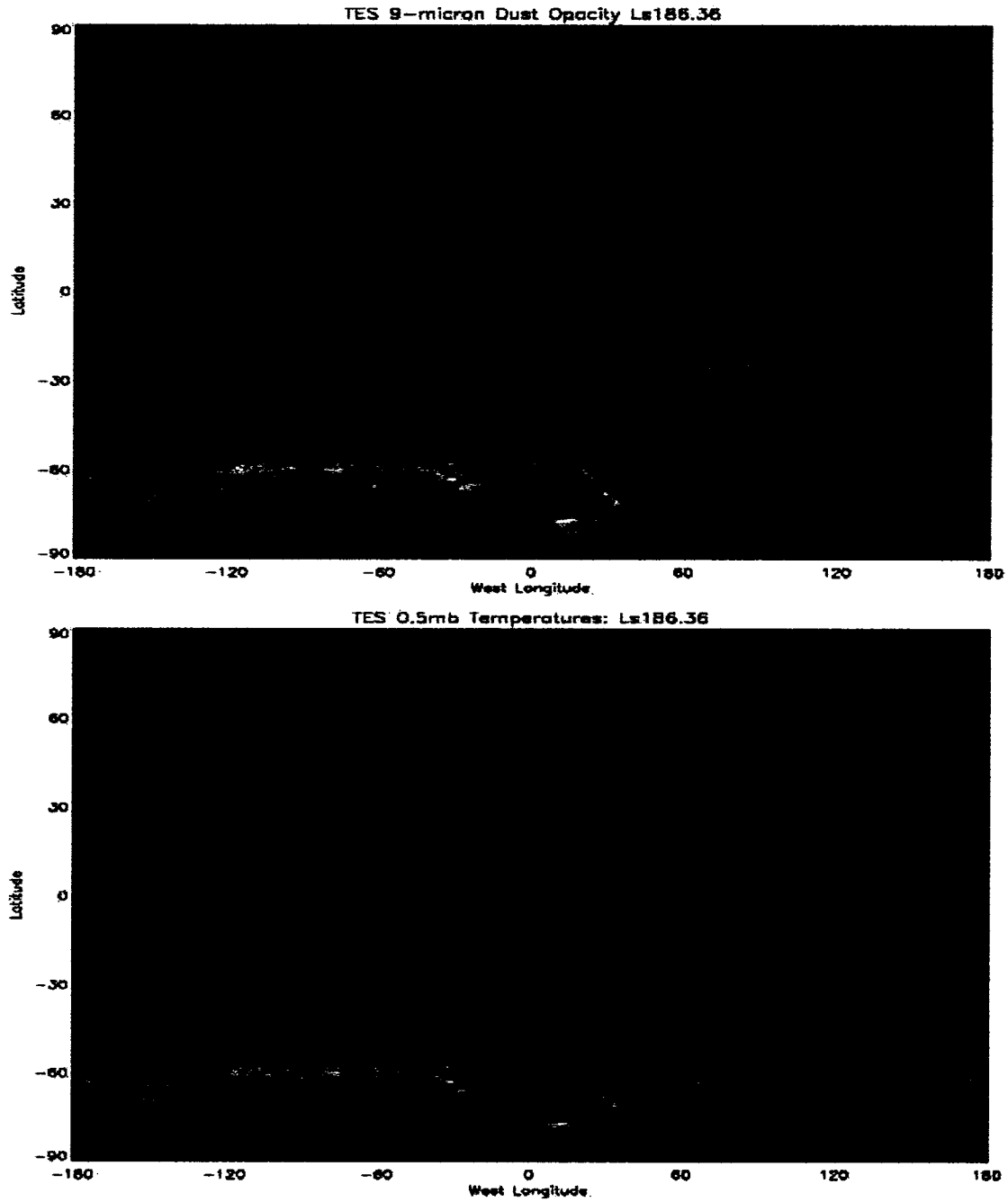

Fig. 14. MOC Image from L_s 186.3° with overlaid TES opacity (top panel) and TES 0.5 mb temperatures (K) (bottom panel). The dustiest region is in northeastern Hellas, although values of 0.2 values are common along the southern cap edge. At the equinox season, the atmospheric circulation is symmetrical with polar vortices present in both hemispheres. The tropics show little variation in temperatures.

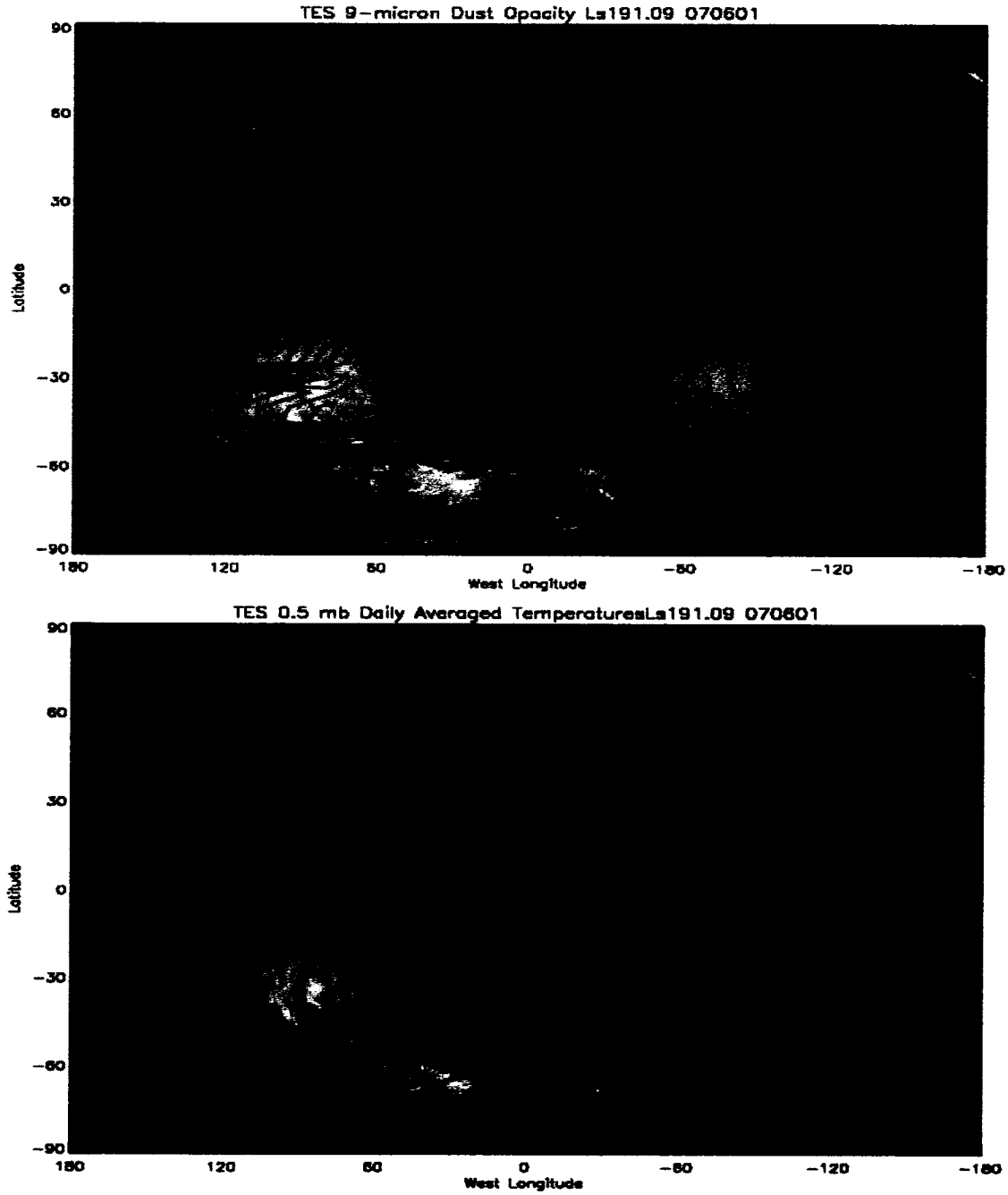

Fig. 15. MOC Image from L_s 191.1° with overlaid TES opacity (top panel) and TES 0.5 mb temperatures (K) (bottom panel). Dust levels have risen in Hellas and begun to spread northward and eastward. Longitudes around the prime meridian have yet to be affected by the dust cloud. The northern polar vortex is intensifying and the upper atmosphere shows significant warming as dust is injected high into the atmosphere.

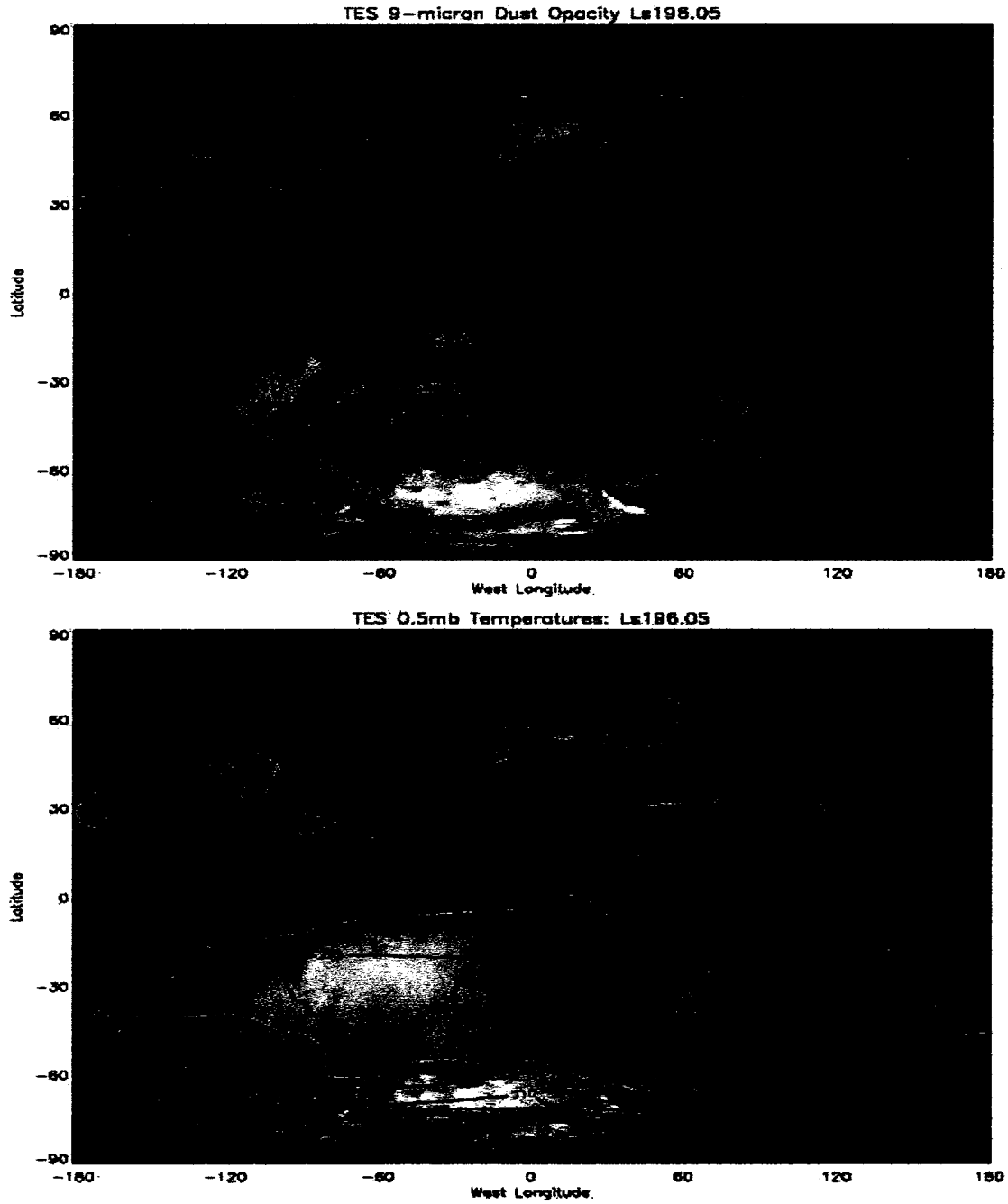

Fig. 16. MOC Image from L_s 196.1° with overlaid TES opacity (top panel) and TES 0.5 mb temperatures (K) (bottom panel). High opacities now exist at all longitudes. The northern polar vortex is intensifying and the upper atmosphere shows significant warming as dust is injected high into the atmosphere.

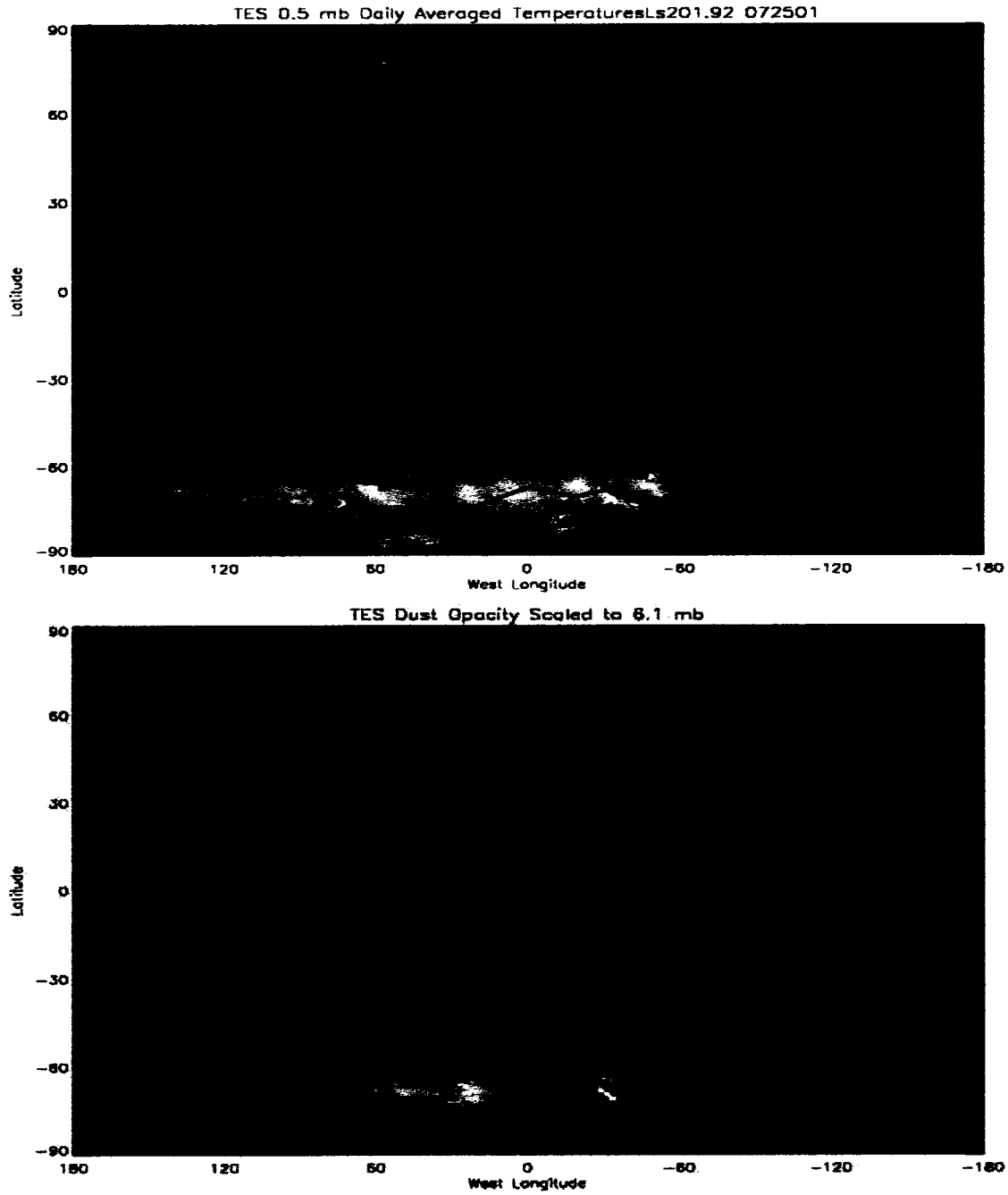

Fig. 17. MOC Image from L_s 201° with overlaid TES opacity (top panel) and TES 0.5 mb temperatures (K) (bottom panel). The highest opacities are now in the Claritas region, yet the entire southern hemisphere has opacities greater than 1.0. As dust enshrouds the planet, temperatures have risen to above 220 K from –60°S to 30°N.

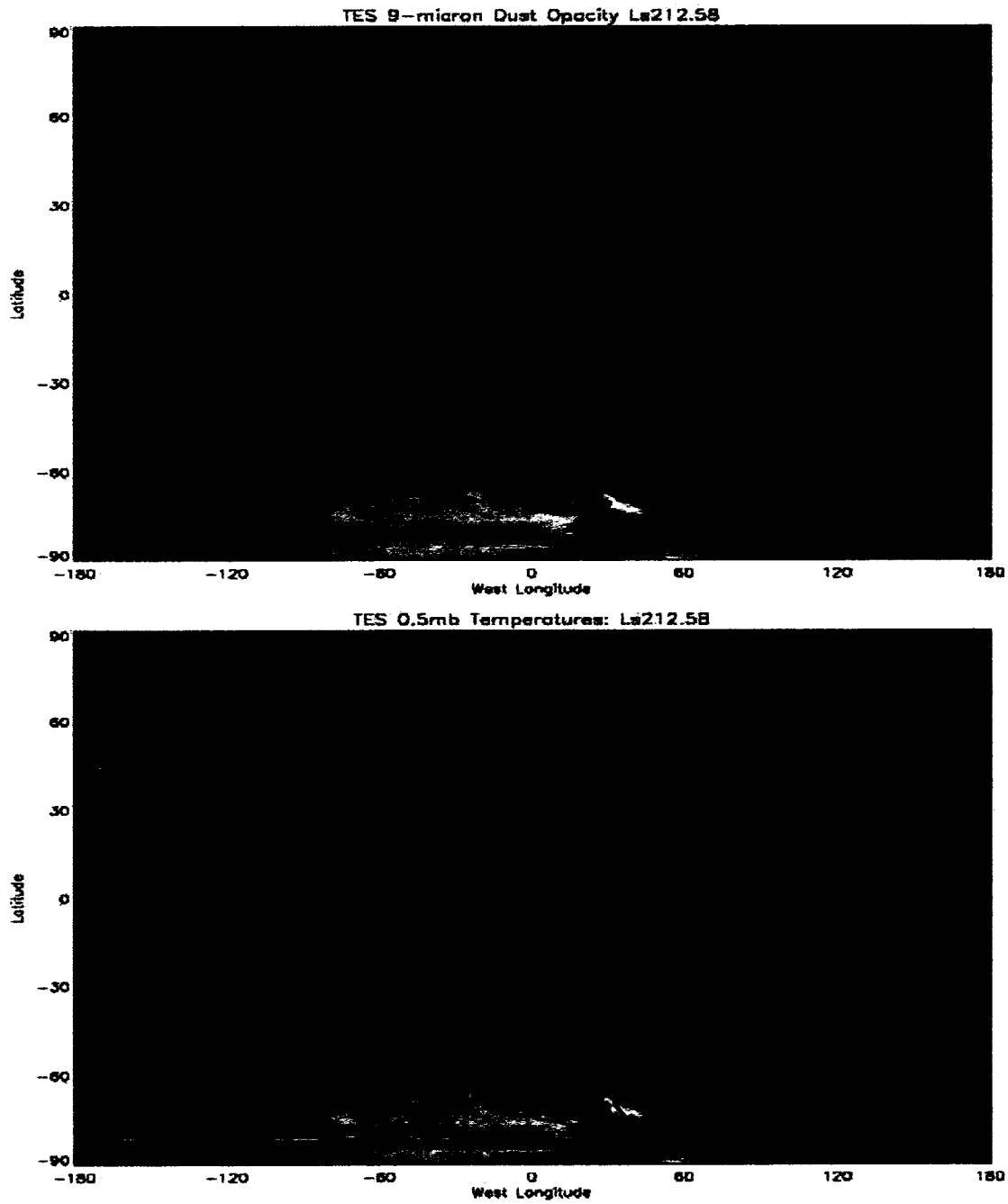

Fig. 18. MOC Image from L_s 212° with overlaid TES opacity (top panel) and TES 0.5 mb temperatures (K) (bottom panel). The highest opacities are now in the Claritas region, yet the entire southern hemisphere has opacities greater than 1.0. As dust enshrouds the planet, temperatures have risen to above 220 K from –60°S to 30°N.

70°S show the boundaries of the polar vortices. The northern polar vortex is quickly becoming better developed as winter affects the northern hemisphere. The temperatures from 30°N to 45°S have risen nearly 30 K in the last 17 sols. Several large areas with temperatures of at least 220 K are noticeable near Solis Planum (Fig. 1) and northeast of Hellas. These elevated temperature regions indicate that dust has been lifted to the 0.5 mb level, where it warms by directly absorbing solar radiation. These increases also indicate the seasonal warming in the southern hemisphere. Also, a 40 K temperature gradient exists between the south pole and the south cap edge, a 10 K increase since L_s 181°. Opacities climbed to 1.5 in northeastern Hellas, and values have considerably increased northward and eastward. Solis Planum and Claritas show values greater than 2.0, as the main dust lifting is now occurring in the western hemisphere. In Claritas, opacities of 2.0 are also seen, although values quickly fall off to the east. The lowest dust levels in the southern hemisphere (0.5-0.8) are between 30°W and 45°E, in the region between the Claritas and Hellas lifting centers. Northern hemisphere opacities are greater than 0.5 from 35°N to the equator. Lower dust levels (<0.4) are seen poleward of 45°N due to the presence of the polar vortex.

The rapid growth phase (L_s 196°) is shown in Fig. 16 and Fig. 17 shows the storm even more entrenched in its growth phase (L_s 201°). At this time, large TES opacities are in the Claritas region, south of Tharsis, exceeding 3.0. At this time, global opacities have climbed above 1.0 for the entire southern hemisphere and well into the northern mid-latitudes. An opacity gradient of >1.0 is noticeable around the Claritas lifting center. At this time, the storm has grown into a global event and 0.5 mb temperatures are

at least 230 K from 30°N to 60°S. The northern polar vortex has further intensified (showing 70 K gradients from 45°-70°N), while the southern vortex is decaying (< 30 K) as the summer season approaches. A large area of temperatures above 230 K coincides with the Claritas lifting center (now the main lifting center), where dust at high altitudes continues to heat the upper atmosphere. Peak globally averaged opacities occurred near L_s 212°, and Fig 18. shows the planet at this time.

5.5 Working Hypotheses on Origin and Evolution

MGS observations allowed us to visualize the storm's lifecycle. Specifically, the visible images combined with temperature and dust information allowed an in-depth view of the storm's intricacies. The close proximity of the 2001 global dust storm to the southern cap, and the slope flows induced by the topographical depression, led to the formation of strong lifting centers and regional storms in the Hellas region. Although commonplace most years, the difference in 2001 was that a global dust storm emerged, suggesting this year was unique in its meteorological conditions.

The pulses of dust that moved into southwestern Hellas prior to L_s 180° could have arisen from baroclinic disturbances that formed in the area. These successive pulses transported dust into the region where large increases in opacity soon followed. The time scales (of several sols) are consistent with transient disturbances that often arise on Mars that have been both observed and simulated (Barnes et al. 1993; Hinson and Wilson 2002; Wilson et al. 2002). Furthermore, these disturbances may have provided the energy needed to create the first large lifting center in Hellas.

Dust was observed to move over the southern ice cap east of the Hellas basin at the same time as a northward surge of dust was observed 180° in longitude away. This could indicate the presence of a wave-1 stationary wave pattern that allowed the development of the Claritas lifting center. GCM simulations performed by Colaprete et al. (2005) predicted the presence of a stationary wave side on the eastern side of Hellas, precisely where the dust movement was observed. The stationary wave position is due to the topographic forcing caused by the Hellas Basin.

An increase in the thermal tides may have aided in the initial expansion of the 2001 global dust storm as well. Leovy and Zurek (1979) found that diurnal and semidiurnal components of the pressure and wind oscillations were observed to systematically increase after the onset of a dust storm. The localized increases in opacity seen in Hellas may have triggered an increase in these tides as the injection of particles high in the atmosphere altered absorption of solar radiation (Leovy et al. 1973). The strong lifting observed in Hellas could also have triggered a positive feedback, promoting the lifting of more dust by increasing the amplitude of the thermal tide.

As dust loading increased, the mean meridional circulation patterns may have been altered, allowing dust to migrate eastward and northward. The strong latitudinal temperature gradients seen from the TES observations in the southern hemisphere mid-latitudes are most likely accompanied by strong upper-level westerly winds. This is consistent with the thermal wind relationship.

The Claritas lifting center appeared to be the lifting center that transformed this from a regional to a global event. The growth in this area may be due to a sharp increase in the

diurnal tide, as observed dust lifting only occurred during the day, when solar radiation could be absorbed (Cantor 2005). This amplification also occurred as solar insolation was nearing its peak in the southern hemisphere low latitudes.

Ultimately, the 2001 global dust storm reached a point where dust could no longer be injected into the atmosphere and opacities started falling. One possible reason is that the finite supply of dust simply was exhausted. That is, all available dust from the main dust lifting regions had been injected. It is also possible that a critical level of dust in the atmosphere was reached where lifting mechanisms shut down, or that the widespread dust haze reduced the effectiveness of dust lifting in the core lifting centers of Claritas.

The changes in the circulation due to increased dust loading caused by the 2001 global dust storm should therefore be examined in more detail. MGS observations illustrate many points, but have some weaknesses. TES observations correlate well with MOC images, although a slight misalignment is noticeable. The regions of maximum TES opacities do not match up geographically to where MOC images indicate the highest levels of dust. Generally, a 5° difference in longitude separates the respective maxima. In order for the MOC mosaics to be continuous, planetary images, some interpolation and approximations were used. These approximations act to offset the opacities at certain local times. It is important to remember that each MOC image only takes a 30° wide image, so a daily image does not reflect the same moment of time planet-wide, but rather the aggregate of one full sol's worth of data.

The observations available do not describe the mechanisms responsible for the global dust event, nor do they fully clarify the circulations patterns during the dust storm

period. TES observations are only taken twice a day, which does not allow one to see a full diurnal variation. No wind information is available to provide insight into why dust is being lifted. MGCM simulations will provide a greater understanding of this storm by showing the circulation patterns that may be the cause or result of strong dust loading.

The method for studying the storm is split into two parts: 1) Analysis and interpretation of MGS information; and 2) Model simulations of the MGCM, where the spatial variation, temporal variation and vertical distribution of dust will be prescribed using observed TES dust opacities. MGS data was analyzed using several techniques. At times it was useful to combine multiple data sets to better examine the situation, as it painted a broader picture of the global dust storm. At other times, the isolation of one instrument allowed us to notice trends and traits related to only one data source. Several tests and comparisons to past work were conducted to prove the validity of the data itself. Once inspection of the data was complete, the model, using MGS information was run and model output was first analyzed in raw form. Model output was then organized and analyzed in numerous ways, including direct comparisons to actual MGS data. The objective of the GCM simulations is not an attempt to replicate the 2001 dust storm event, but instead to examine the circulation patterns seen while under dust-storm conditions.

6. MARS GCM SIMULATIONS OF THE 2001 GLOBAL DUST STORM

6.1 Ames GCM Description

MGCM work stemmed from the successful use and development of Earth GCMs, which attempt to simulate global circulation patterns. MGCM work began with Leovy and Mintz (1969), who used the primitive equations to examine the energy transfer mechanisms in the Martian atmosphere. Mass and Sagan (1976) and Moriyama and Iwashima (1980) explained the role topography has on dust lifting and its heating effects. In particular, Moriyama (1974, 1975) noted that suspended dust affects both solar heating and thermal cooling of the atmosphere. The NASA Ames Research Center MGCM was initially developed using the primitive equations and with a scheme from the UCLA model. Consistent revisions and improvements have been made by Pollack et al. (1976, 1981, 1990) and later by Haberle et al. (1993, 2002, 2003). This model has been used to interpret MGS data, as well as Orbiter and Viking data, and this has led to a better understanding in the circulation patterns and other atmospheric phenomena. Continued developments of MGCMs are occurring at a rapid pace as computing technology advances and research projects proliferate. Current model improvements to the NASA Ames MGCM by Haberle et al. (2003) include adjusting the tendencies for diabatic heating and using atmospheric tidal responses that compare well with Viking Lander surface pressure measurements. The current radiation scheme includes the effects of dust and CO_2, and accounts for aerosol multiple scattering and gaseous absorption (Haberle et al. 2003). In regards to dust lifting, model analysis is used to model preferred regions for dust lifting (Haberle et al. 2003). Results show that the strongest lifting occurs during

northern fall and winter (when the planet is closest to the sun). They developed a lifting rate equation to determine the depth of dust that could be removed from the surface during a specified period of time. In order for the model to predict lifting, a given location must have a surface stress value greater than an assigned threshold. The lifting rate is giving by this expression:

$$FLUX = (2.3 \times 10^{-3}) * \tau^2 * [(\tau-\tau^*)/\tau^*] \ (kg\ m^{-2}s^{-1}),$$

where τ and τ^* are in units of N m^{-2} and $\tau^* = .0225$ N m^{-2}.

The stress value (τ) is a function of latitude and longitude and is required to be greater than τ^*, otherwise model bins have a value of zero.

6.2 Approach and Setup

The simulations used in this project use version 1.7.3 of the NASA Ames MGCM. The MGCM is a hydrostatic, finite difference model constructed on the Arakawa c-grid. Our simulations have a spatial resolution of 7.5° latitude x 9° longitude, so there are 24 grid points in latitude and 40 in longitude. We use 30 vertical sigma layers, with sigma level 30 being the surface and sigma level 1 being 5 $\times 10^{-5}$ mb (~ 80 km). The top of the model is set at 5 nanobars, corresponding roughly to the 100-kilometer level. Elevation parameters are based on MOLA topography.

Each simulation discussed below covers the time period L_s 170°-240°. This generates 119 sols of data for each year, giving ample time to see year-to-year changes, as well as seasonal changes. For year 2, model output covers the period May - September

2001, which thoroughly covers the pre-storm, development, peak, and decay of the global event. The MGCM outputs data 16 times per day, or roughly every 1.5 Mars hours. Temperature, geopotential, the u-wind component, and the v-wind components were each archived as functions of latitude, longitude, sigma pressure level, and time. Pressure, ground temperature, and the x and y components of surface stress field are also archived.

For the MGCM simulation, the dust distribution is adjusted to look like the 2001 storm. Two 50-sol simulations are used to gather the information for the storm's entire duration. The same TES dust opacity observational data are inserted into the model to follow the storm's path. That is, the temporal and spatial distribution of dust is prearranged using TES dust data. The only difference is that the latitudinal grid spacing used in the model (7.5°) is slightly coarser than the 5° increments in latitude gathered from observations. Any instances of missing data are once again filled with a zonal linear interpolation. TES opacity measurements give an indication of how dusty an atmosphere is, but little indication of how high the dust reaches in the atmosphere. Once again, this is important as the thermal structure of the atmosphere strongly depends on the amount and depth of dust present. For this problem, the MGCM uses the Conrath (1975) parameterization. This model parameter describes how dust is distributed with height. Conrath (1975) described the steady-state vertical distribution of dust using this equation:

$$q(z)=q_0\exp\{v[1-\exp(z/H)]\},$$

where q(z) is the specific dust concentration (particles per gram of atmosphere), H is the pressure scale height, z is the altitude in meters, q_0 is the value of q at z=0, and ν is a term that determines the effective height of atmospheric dust. A different value of ν is used in different dust conditions, so that the height of injected dust is as accurate as possible. For this experiment, ν is set to 0.03, to better analyze the extremely dusty conditions. Under this modest condition, the dust concentration falls off exponentially with height, and at 25 km, the concentration is at 50% of its 6.1 mb level value. It should be noted that this prescription for the height of dust does not vary in time.

6.3 Results

6.3.1 Surface Stresses and Lifting Rate

Model output suggests the presence of several favorable dust-lifting locations. Fig. 19 shows the surface stress magnitudes during the pre-storm time (L_s 181°). The highest stresses occur at the western edge of Hellas, precisely the location where MOC imagery indicates lifting. Surface stress values of 18 mN m^{-2} are noticeable in the southwest corner of the Hellas Basin, due to consistent slope flows and a strong temperature gradient between the Hellas Basin and the cap edge. Also near the cap edge, Solis Planum stress magnitudes are around 8 mN m^{-2}. Stress magnitudes above 3 mN m^{-2} are common near the cap edge, but are dominated by the Hellas and Solis regions. Stress values of 10 mN m^{-2} are observed over the western slopes of the Tharsis Ridge, and are associated with increased slope flows.

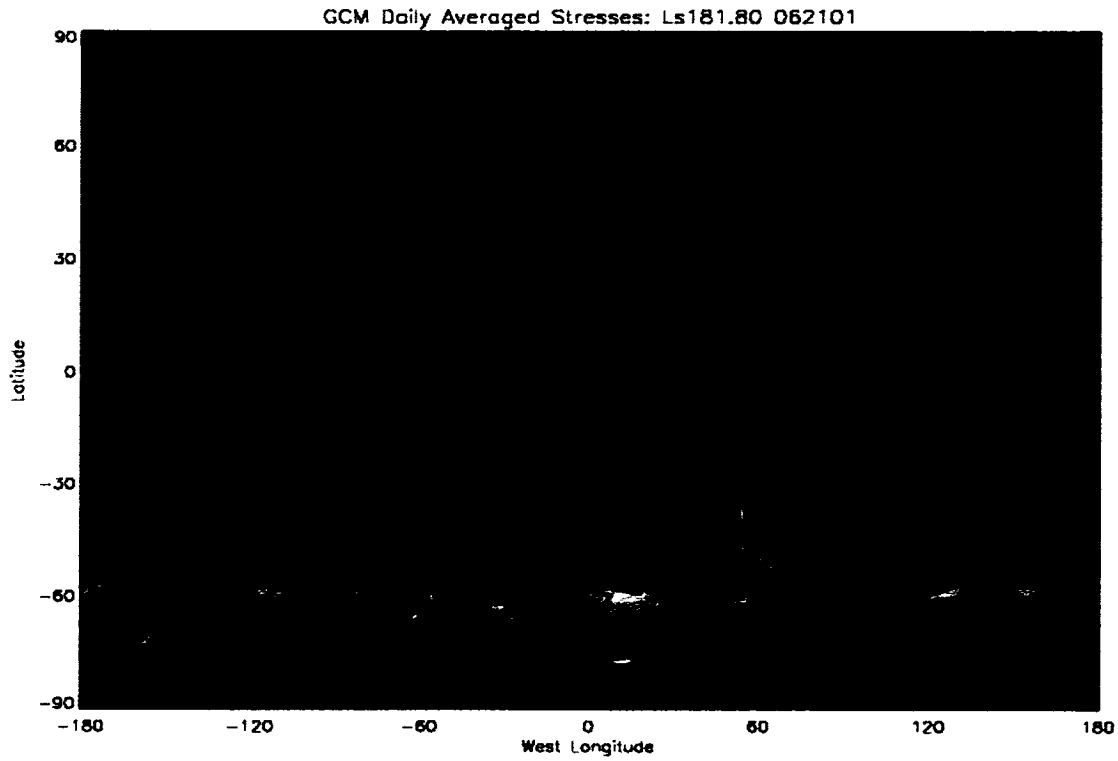

Fig. 19. Daily averaged surface stress magnitudes (mN m^{-2}) for L_s 181°, overlaid on a MOC mosaic. Maximum stress magnitudes are noticeable in the southwest region of the Hellas Basin.

Fig. 20 shows the stress field during the stage of rapid growth (L_s 188°) . The highest stress values are still in western Hellas, with values above 18 mN m^{-2}, but surface stress values in the visibly dust areas show an increase. Surface stresses east of Hellas have doubled, as the dust cloud moves along, indicating a positive feedback. That is, a dustier atmosphere leads to higher surface stresses, and more dust can to be lifted. The more dust in the atmosphere, the more dust can be lifted. This is also the region where a stationary wave is hypothesized to exist. In Syrtis Major Planum, stresses have risen to 8 mN m^{-2} as the dust cloud moves northward. High stress fields remain west of the Tharsis volcanoes. No dust was observed to lift from these locations, suggesting that the lack of surface dust. Also at L_s 188°, the stress field around Solis has expanded and stress magnitudes have increased to 10 mN m^{-2}.

Fig. 21 shows conditions around the peak of the storm (L_s 212°). As dust has moved around the planet, the overall stress magnitudes have increased, further illustrating the positive feedback. Stress magnitudes have increased in nearly all locations on the planet, yet the south cap edge shows the most activity. At this stage, the maximum observed dust lifting by MGS was south of the Tharsis region, where stress values are 6-8 mN m^{-2}. Large stress values greater than 25 mN m^{-2} are noticeable south of Hellas Basin and southeast of Solis Planum.

Figs. 22-24 show year two/year one comparisons of the stress field. At the pre-storm time, there are similar stress distributions since both years had comparable dust opacity values. For both years, the greatest magnitudes are located west of Hellas and west of the Tharsis ridge, with magnitudes near 12 mN m^{-2} both years. The small

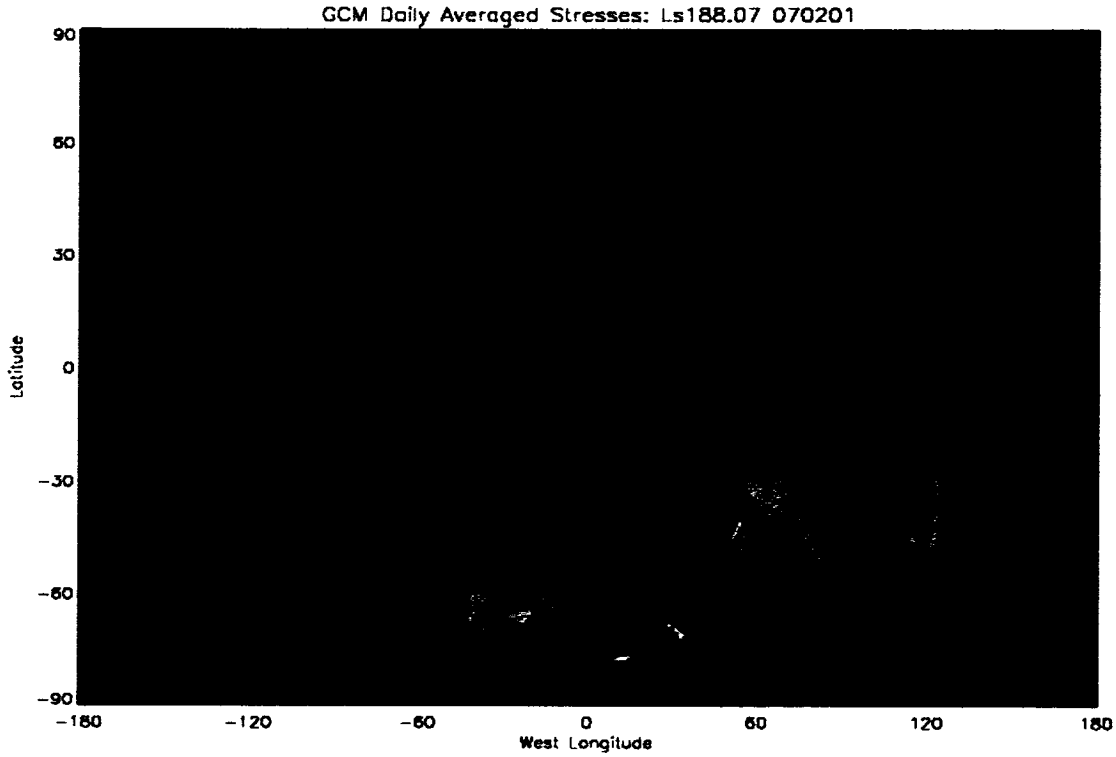

Fig. 20. Daily averaged surface stress magnitudes (mN m^{-2}) for L_s 188°, overlaid on a MOC mosaic. Maximum stress magnitudes remain in the western region of Hellas, although all dusty areas show an increase in stress magnitude.

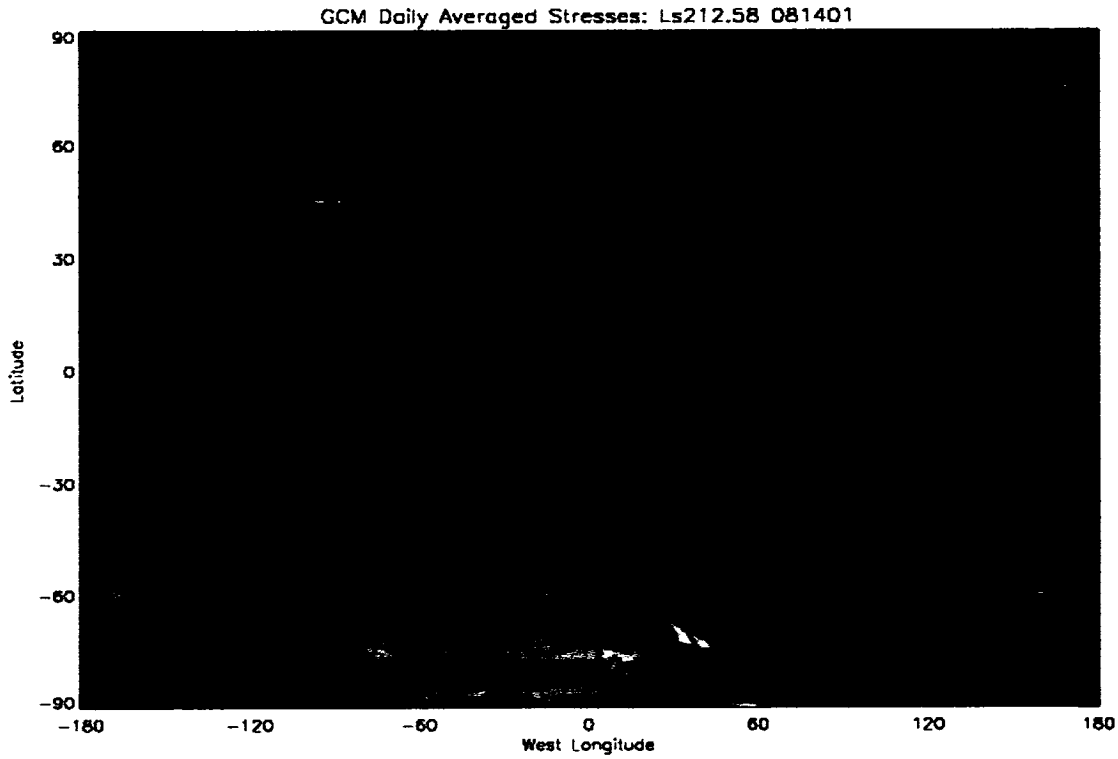

Fig. 21. Daily averaged surface stress magnitudes (mN m^{-2}) for L_s 212°, overlaid on a MOC mosaic. Stress magnitudes have increased globally, yet the south cap edge still has consistently high magnitudes (>20 mN m^{-2}).

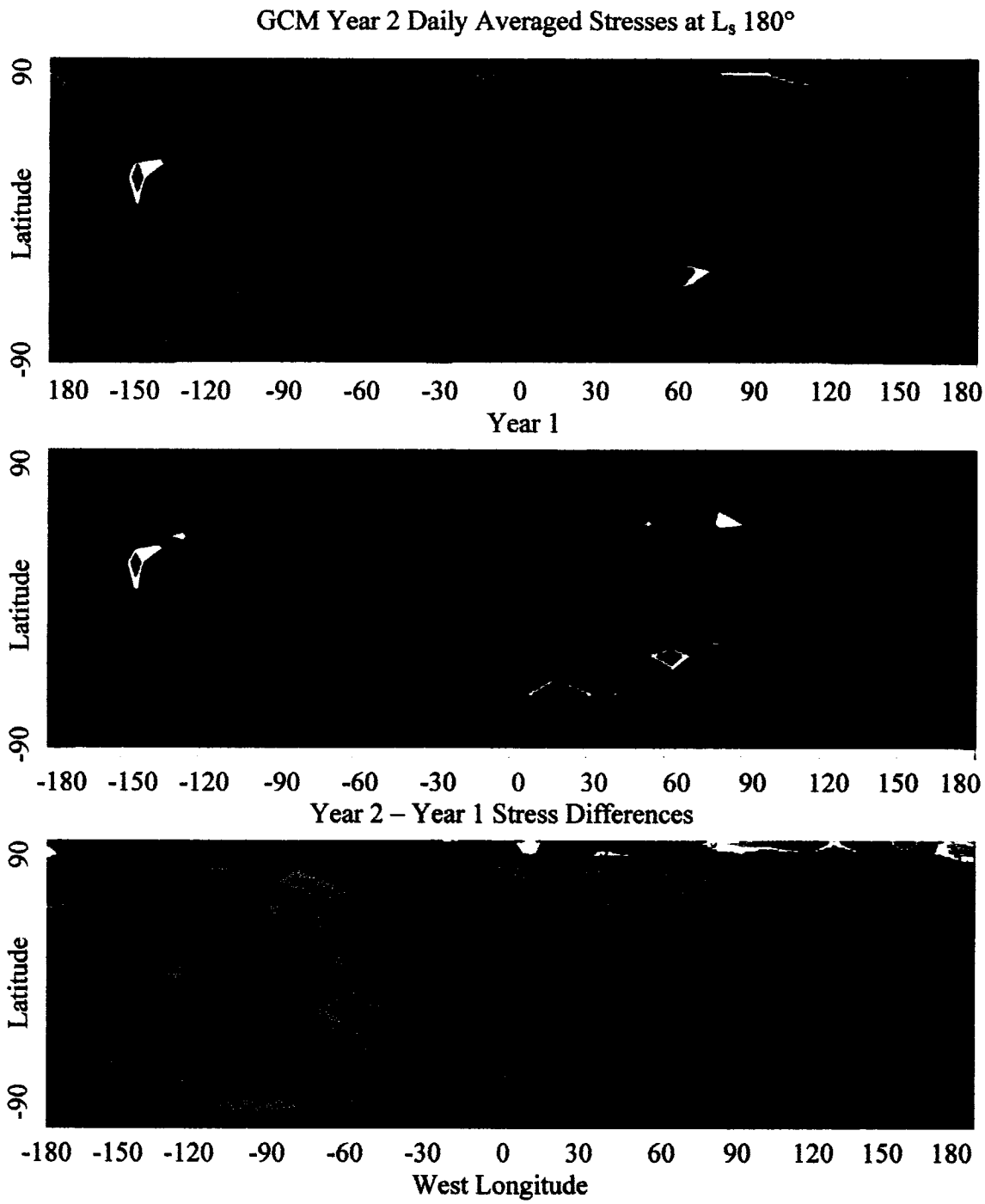

Fig. 22. Surface stress magnitudes in mN m^{-2} at L_s 180° for year two (top panel), year one (middle panel), and year two-year one differences (bottom panel). Prior to the dust storm, both years experience similar stress fields, with small differences due to interannual variability in weather.

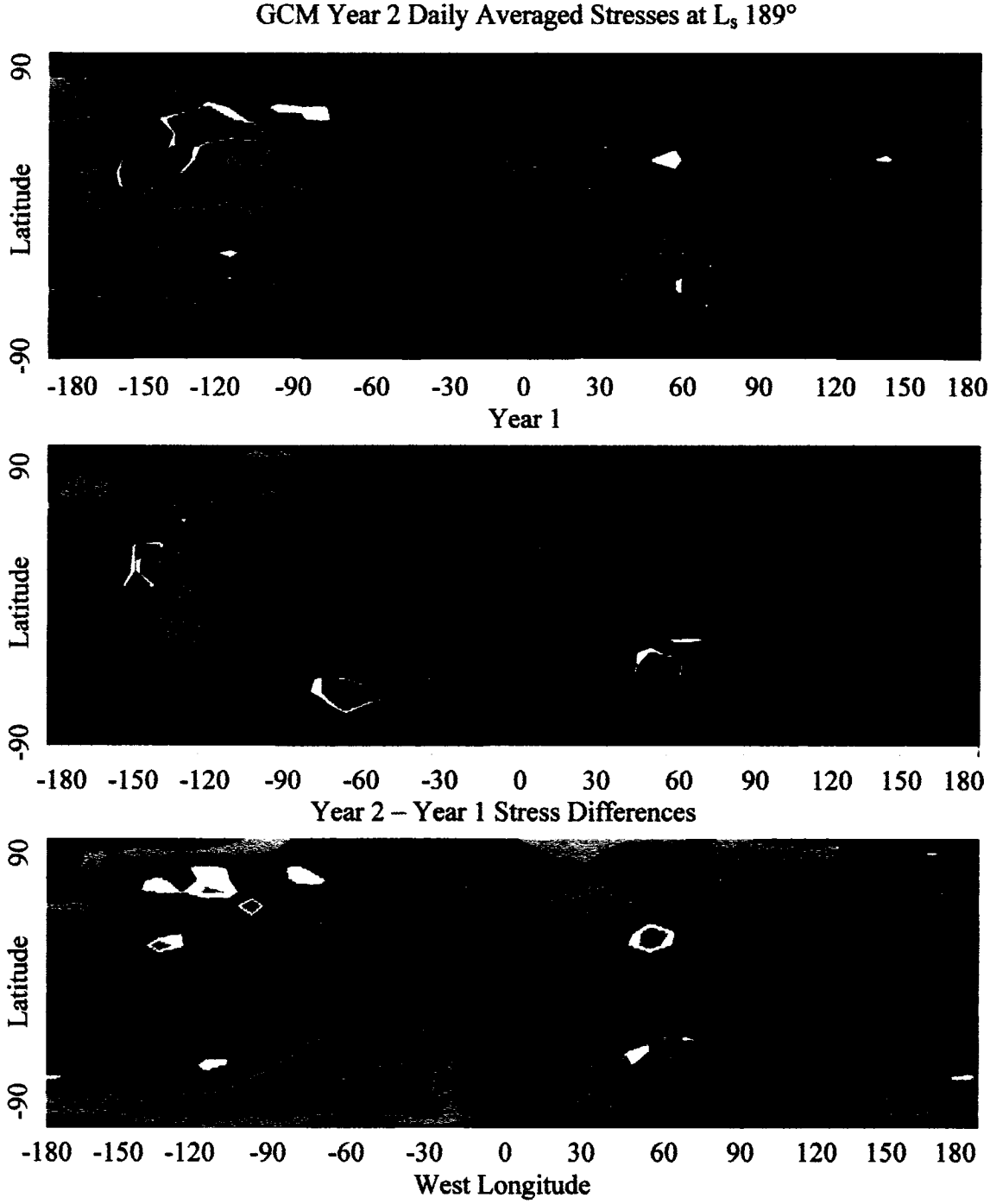

Fig. 23. Surface stress magnitudes at L_s 189° for year two (top panel), year one (middle panel), and year two-year one differences (bottom panel). Year two shows stress levels of > 10 mN m^{-2} in western Hellas and southeast of Solis Planum.

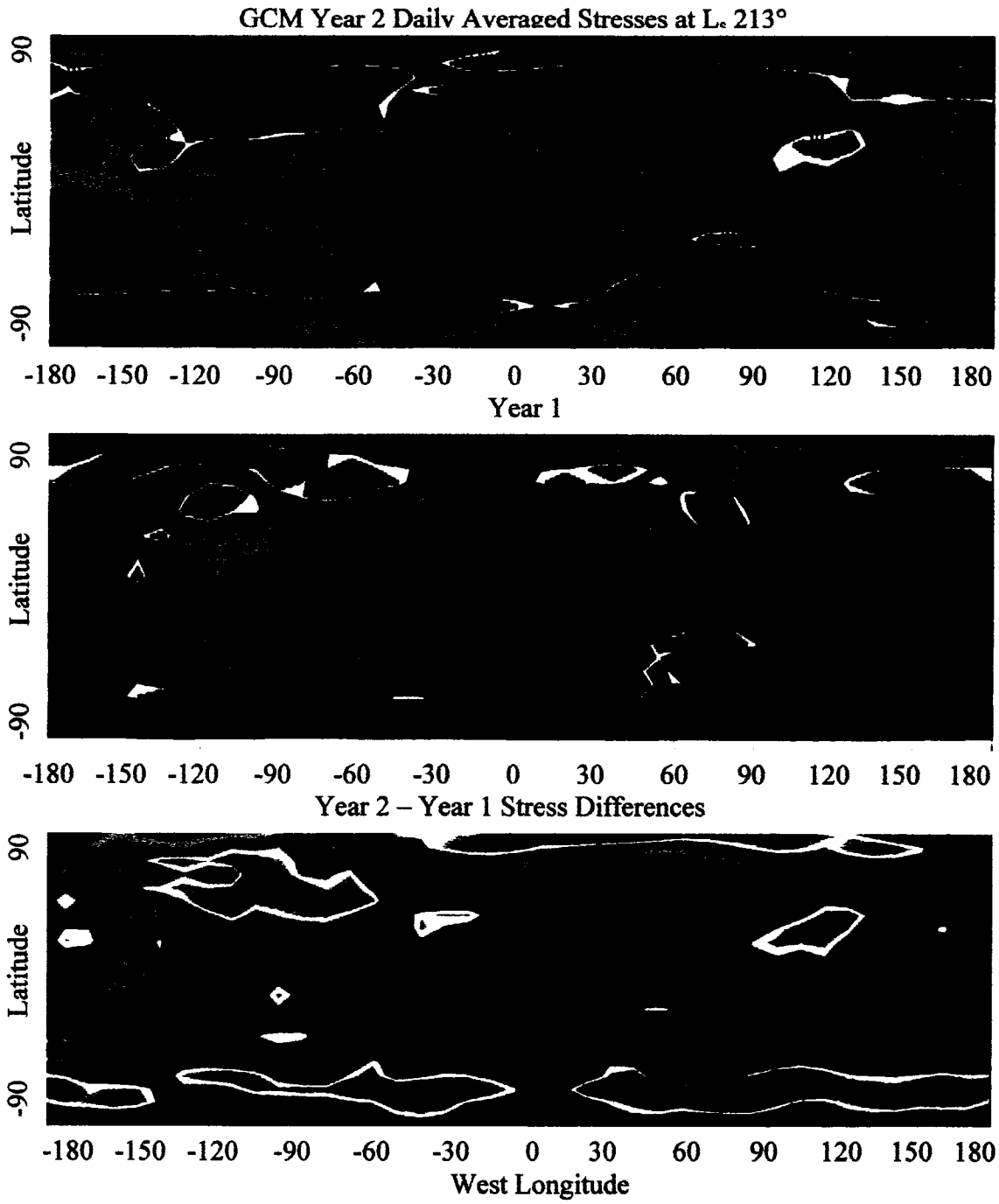

Fig. 24. Surface stress magnitudes at L_s 213° for year two (top panel), year one (middle panel), and year two-year one differences (bottom panel). Year two shows a 5 mN m^{-2} increase in stress magnitude in the Claritas region.

differences seen are attributable to yearly differences in the weather patterns. As the storm grows (L_s 189°), year two shows an enhancement in stresses in the Claritas region, with values of 8 mN m^{-2} (5 mN m^{-2} greater than year one). Year one and two both have similar stress fields (greater than 20 mN m^{-2}) in Hellas, indicating the Claritas lifting center was a major difference in the development of the global dust storm. At the storm's peak, the biggest changes from year two to year one occurred in regions where the stress fields were already strong. The increases in the stress field near the southern cap edge in year 2 are large, but do not correlate with lifting centers, indicating a finite supply of dust in these regions. Stress levels in southwestern Hellas show a decrease of 4 mN m^{-2} from year one. Dust opacity levels have increased to the point where surface dust can no longer be lifted as efficiently. This is perhaps an indication of a negative feedback mechanism. Furthermore, stresses are stronger in the Tharsis area in the dust storm year. Year one shows magnitudes 5 mN m^{-2} higher than year one in the Claritas region.

The hourly lifting rates are used to determine when during the course of a sol dust is lifted. We use the lifting rate equation from Haberle et al. (2003) to look at both year two and year one by taking surface stress fields and inserting them into this formula. Fig. 25 shows the lifting pattern during the rapid growth phase, where the local time at the prime meridian is 7:30 am. At this time, the model showed lifting occurring east of Hellas and in the Claritas region, which is consistent with observations. However, closer inspection of other times of the day reveals that dust is not consistently lifted in the Claritas region all day long. Only at limited times (usually pre-dawn/morning local time) did model output show lifting in the Claritas region, indicating the possible influence of

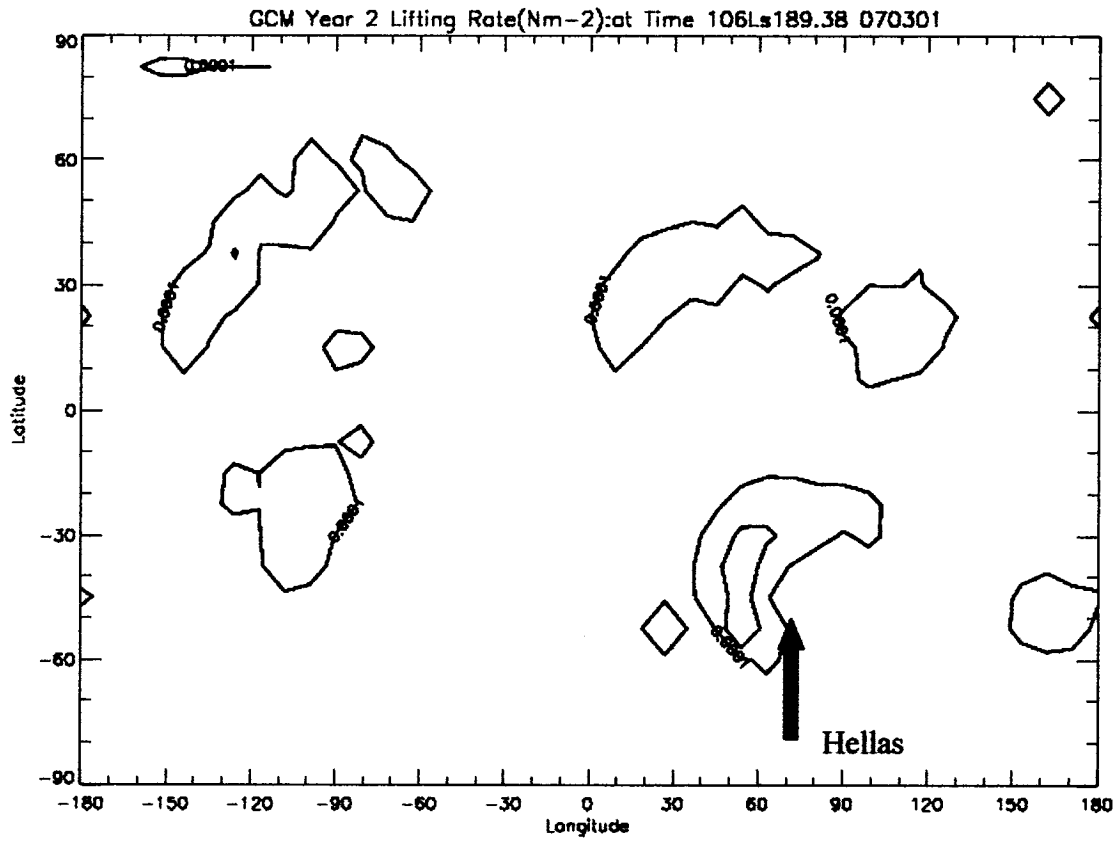

Fig. 25. Dust lifting rate at L_s 189° (kg m^{-1} s^{-1}). Contours indicate where dust lifting is possible. Of particular interest are western Hellas and the Claritas region, regions that show dust lifting is possible.

the diurnal tide. This is unlike the western slopes of Hellas, which is an area that always has the ability to lift dust.

Slope flows and the strong temperature gradients near the cap edge are factors in lifting dust. Fig. 26 shows the diurnal variation in surface wind speed at L_s 195°. Clearly the strong temperature gradients near the southern cap edge contribute to the largest diurnal variations in wind speed. Maxima are noticed around the 55°S latitude band, where diurnal variations commonly exceed 20 m s^{-1}. Other maxima not along this band mainly relate to slope flow, noticeable over the Tharsis ridge. The Hellas Basin is unique in that it has slope flow and a close proximity to the southern cap edge. Strong temperature gradients from the seasonal ice cap and large differences in topography create pressure gradients, thereby causing strong winds.

6.3.2 Temperatures

Since atmospheric dust directly absorbs solar radiation, vertical temperature distributions give a good idea on how high dust has been the model is injected. Figs. 27-30 show the year two and year one zonally averaged temperature fields versus pressure at various stages, and also the year two minus year one temperature differences. Several general trends can be observed as the southern spring season moves into summer. Southern hemispheric temperatures generally warm as Mars nears perihelion. The northern hemisphere polar vortex becomes a more distinct feature as it intensifies over time, as solar insolation lessens as the winter season approaches. At the storm's onset (Ls 180°), the southern polar latitudes show temperatures greater than year one, up to 9 K

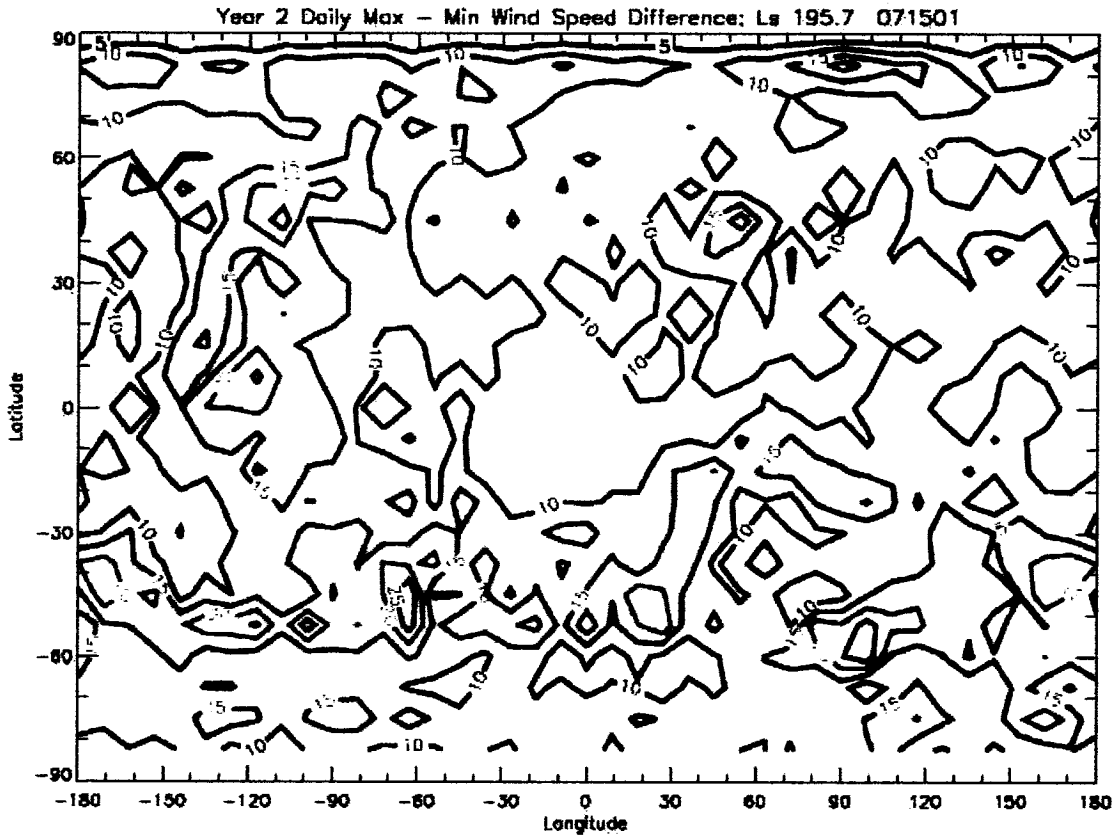

Fig. 26. Daily (maximum – minimum) wind speeds (m s^{-1}) at L_s 195°. Strong variations are seen near the southern cap edge and in the Tharsis ridge.

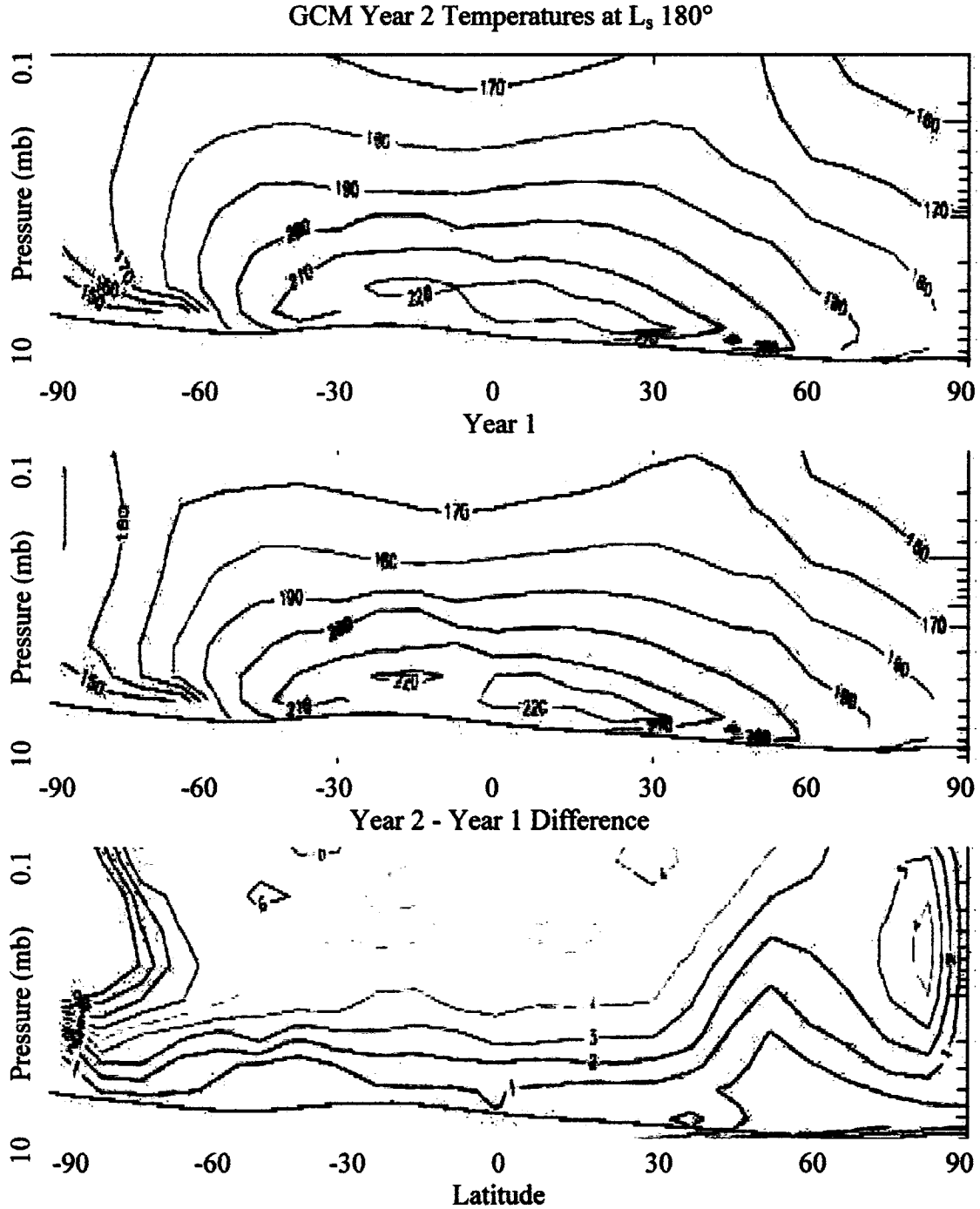

Fig. 27. Vertical temperature distributions (K) for L_s 180° for year two (top panel), year one (middle), and year two/year one difference (bottom). The surface level is indicated by the solid black line that slopes downward from the northern hemisphere to the southern hemisphere.

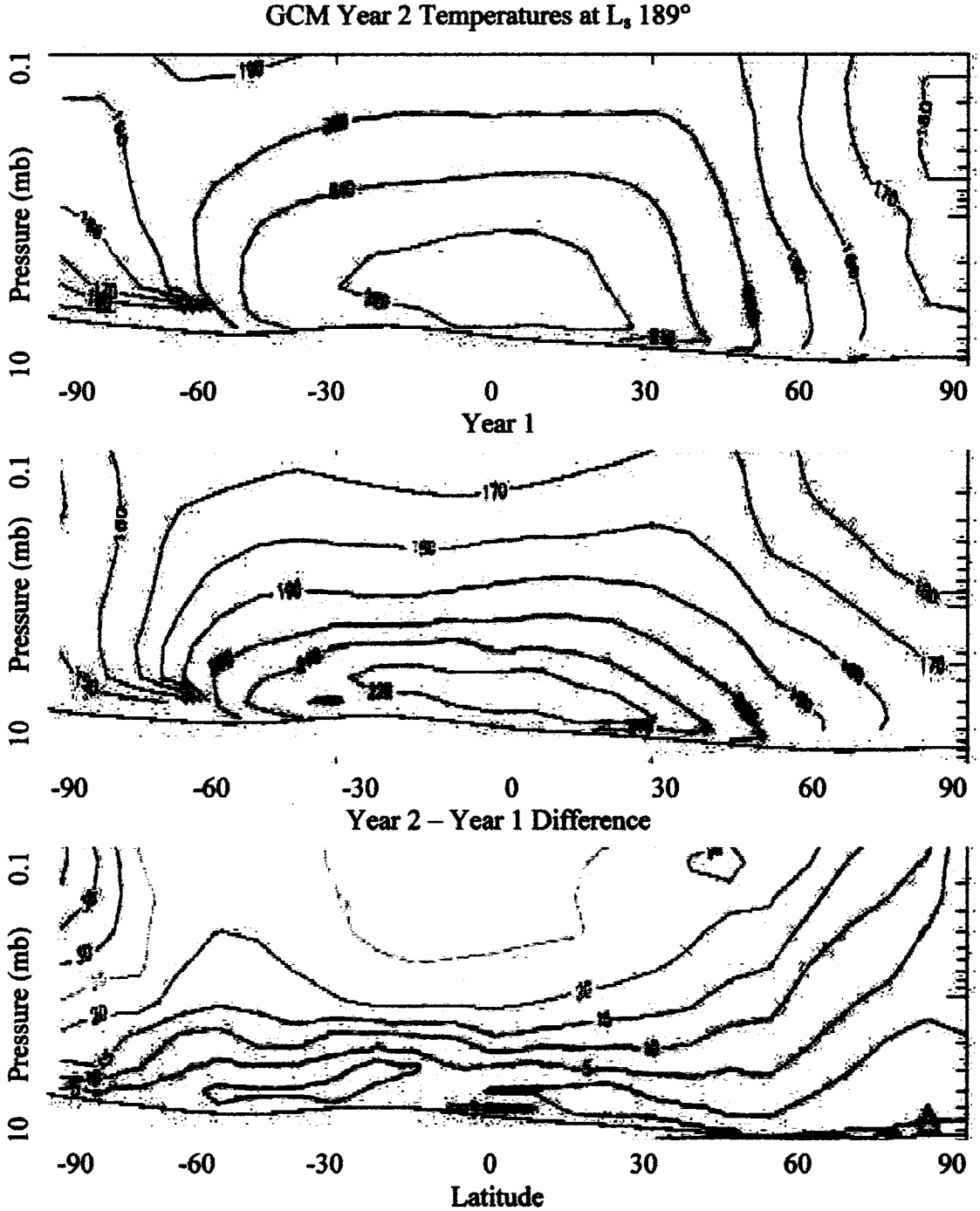

Fig. 28. Vertical temperature distributions for L_s 189° for year two (top panel), year one (middle), and year two/year one difference (bottom). As the storm grows, year two temperatures are warmer aloft, indicating dust has been injected high into the atmosphere.

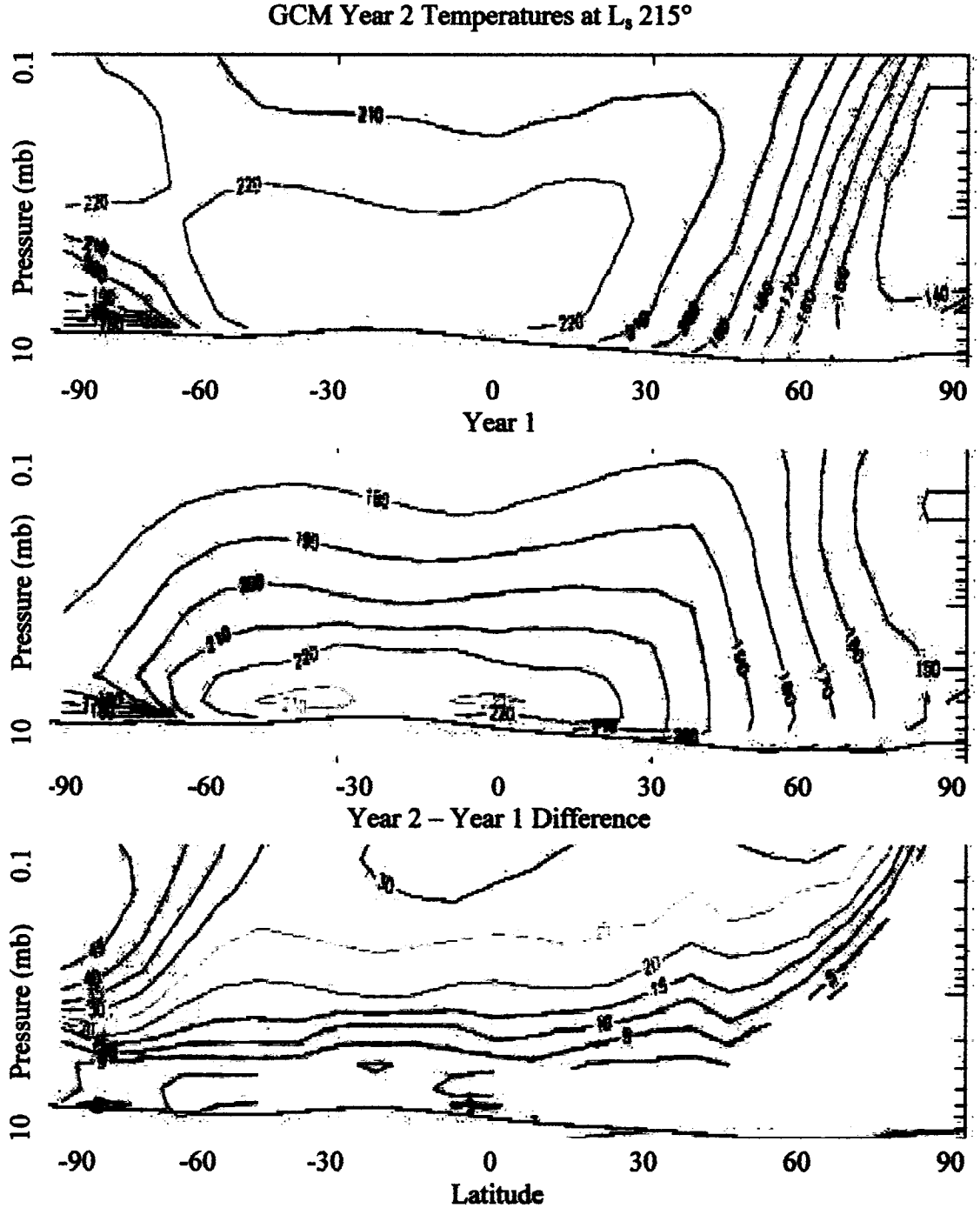

Fig. 29. Vertical temperature distributions for L_s 215° for year two (top panel), year one (middle), and year two/year one difference (bottom). Near the peak of the dust storm, the upper atmosphere in the southern hemisphere is significantly warmer (over 45 K) in year two than year one.

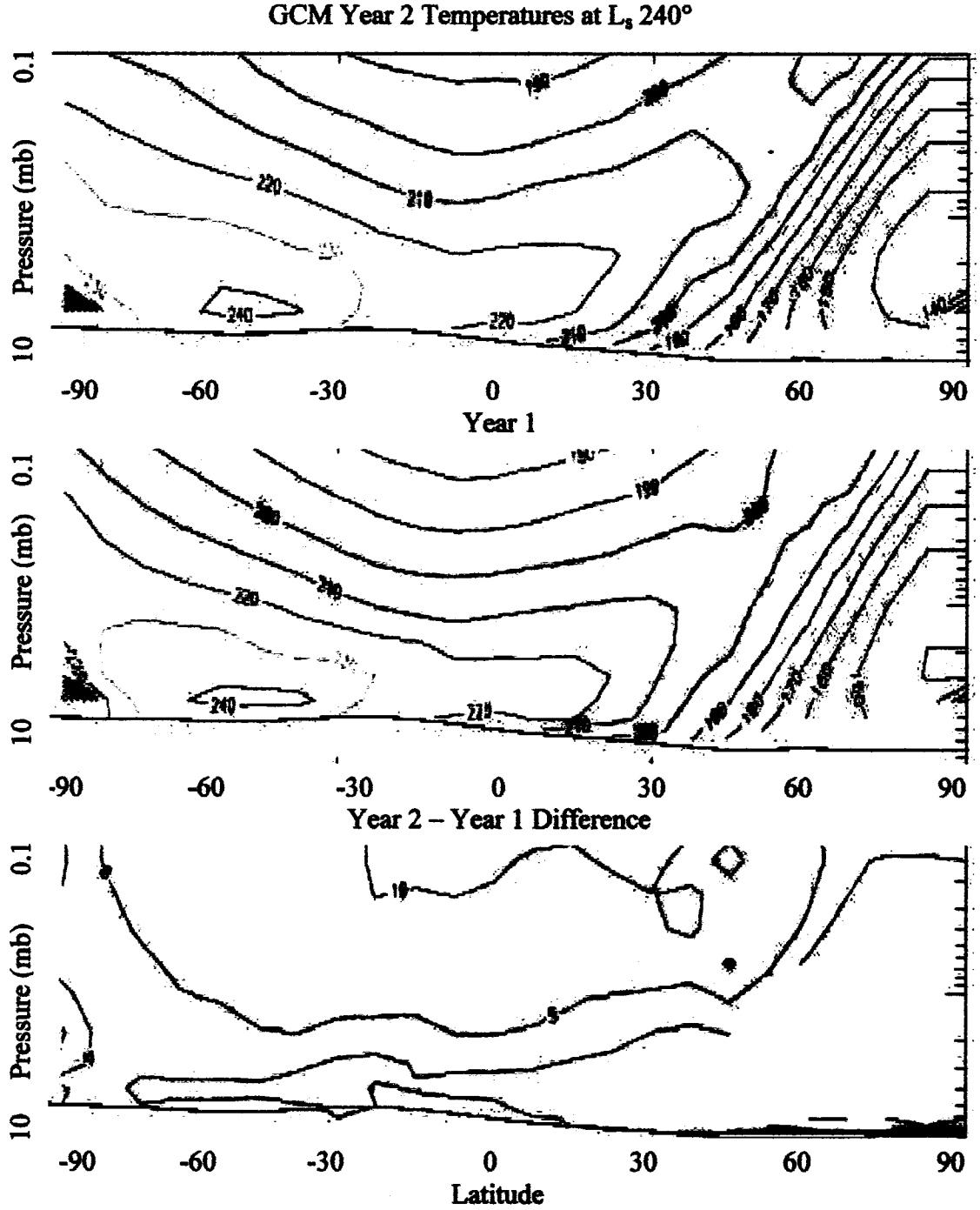

Fig. 30. Vertical temperature distributions for L_s 240° for year two (top panel), year one (middle), and year two/year one difference (bottom). In the decay period of the storm, the northern polar vortex has intensified and years one and two begin to show less variation.

higher above the 1 mb level. This also shows that a weaker south pole-equator temperature gradient exists, which therefore reduces the westerly jet wind speeds (through the thermal wind equation). In year two, a steady warming of the upper atmosphere is apparent, as dust is continuously lifted into the atmosphere. At the peak of the dust storm, year two temperatures show a near-isothermal atmosphere. The near-uniform distribution of temperatures from the southern mid-latitudes to the northern mid-latitudes shows how dust is regulating the temperatures. The dust aloft absorbs solar radiation, but by doing so leaves less solar radiation available to warm the surface.

6.3.3 Zonal and Meridional Winds

Figs. 31 and 32 show the year two and year one zonally-averaged zonal and meridional winds for the entire dust storm period (L_s 180°- 240°). The year two zonal winds show a weaker westerly jet in the southern hemisphere, yet a stronger jet in the northern hemisphere. This can be attributed to an increase in dust at the higher altitudes and the subsequent warming of the atmosphere. This lessened the south pole-equator temperature gradient, resulting in a weaker jet stream. The meridional flow indicates more northward transport of momentum in the dust storm year in the tropics (30°S to 30°N), which may account for the cross equatorial flow of dust. Year two also shows more southward flow near the surface in the southern hemisphere. These results fit well with observations that showed dust flowing over the southern cap and also propagating from the southern hemisphere tropics to the northern hemisphere. The increase in meridional winds at high altitudes indicates an amplified overturning circulation. At ~

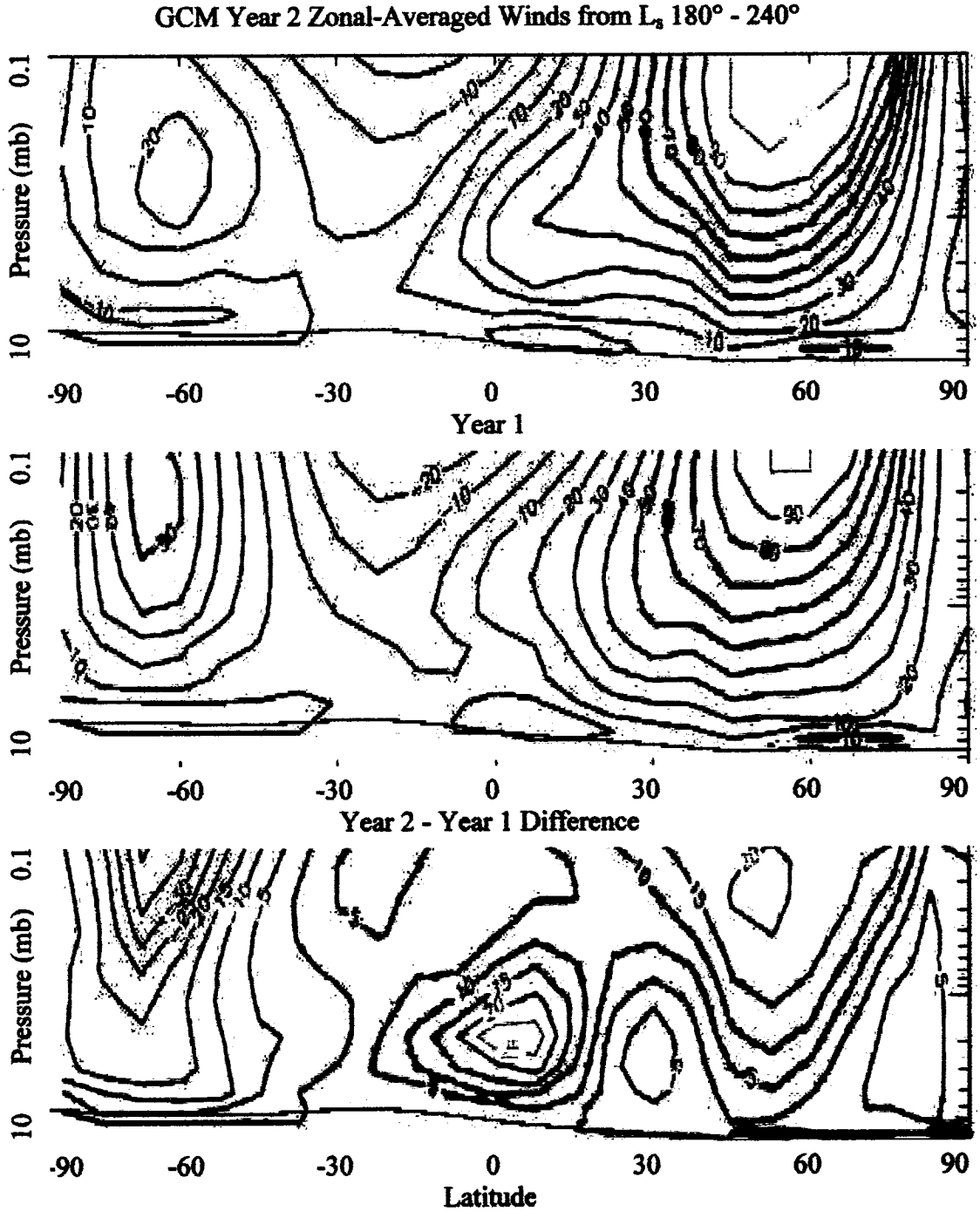

Fig. 31. Zonal winds for the dust storm period in m s^{-1}. Year two shows a weaker westerly jet in the southern hemisphere yet stronger westerly flow in the equatorial region and in the northern hemisphere.

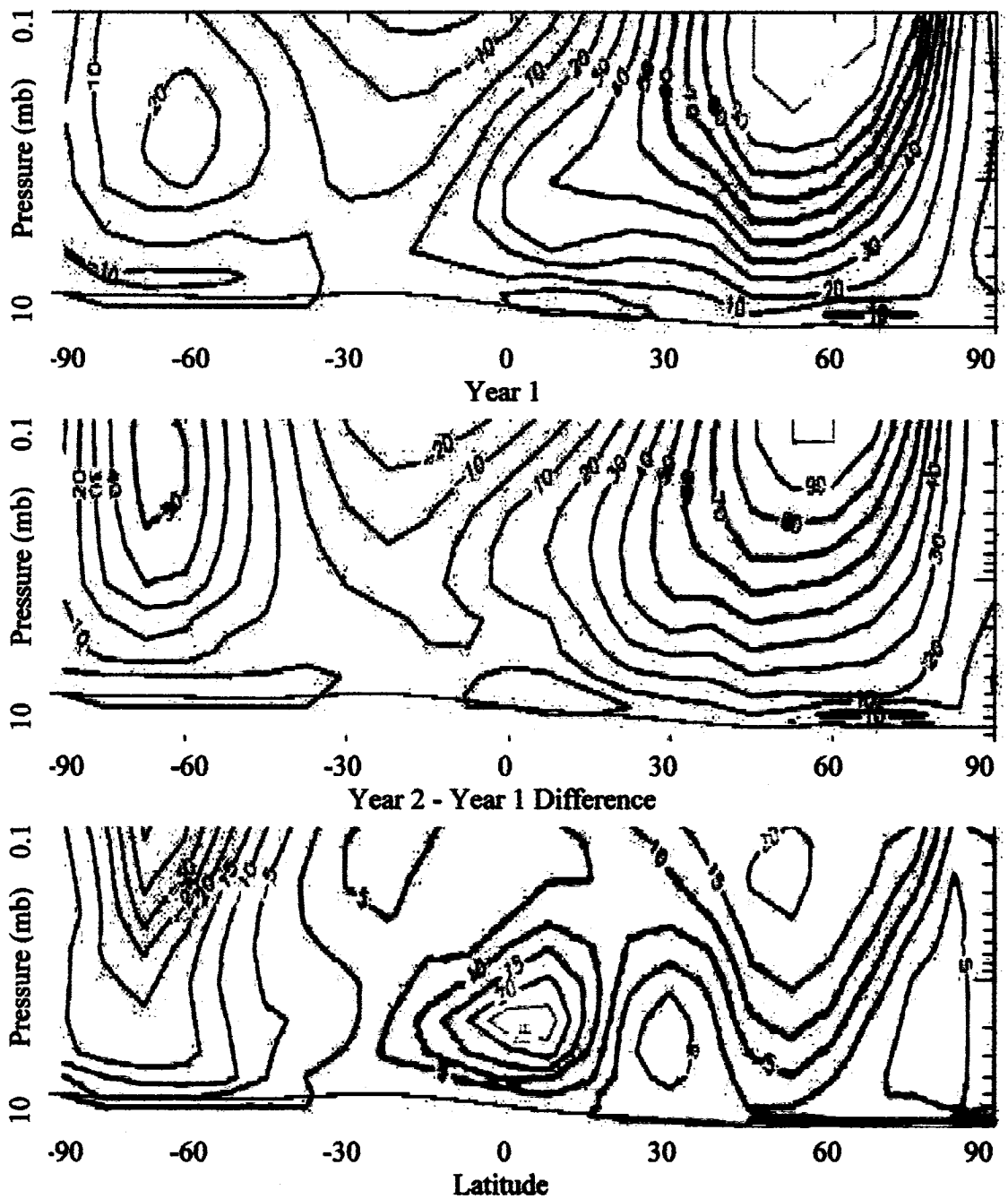

Fig. 32. Meridional winds for the dust storm period in m s^{-1}. Year two shows a stronger northward flow aloft in the tropics, while indicating a more pronounced southward flow of momentum aloft in the southern hemisphere.

40°S, the meridional winds above the 1 mb level appear to diverge in year two, indicating the presence of two overturning circulations, with the rising branch of air occurring over 40°S. Year two meridional winds are ~ 5 m s^{-1} stronger than year one in both circulations. The enhanced southerly flow poleward of 30°S and the northerly flow equatorward shows the intensification of the mean meridional circulation.

6.3.4 Mass Stream Function

The annual changes (at specific ° L_s) in the Hadley circulation are shown in Figs. 33 - 35. This analysis uses a one-day average mass stream function to inspect the overturning circulation. Before the storm's onset (L_s 180°), both years' overall structure appear similar with several slight differences. The stream function values of 0.03 x 10^8 kg s^{-1} between 0.1 and .001 mb above ~ 60°S are three times higher than year one, yet year one indicates a more intense circulation at the 1 mb level in the southern subtropics. At L_s 195°, the rising branch in the southern hemisphere shows a slight increase, indicating a response to the dust loading. Also, stream function values of 10 x 10^8 kg s^{-1} are seen in year two near the equator, compared with year one values around 3 x 10^8 kg s^1. At the storm's peak at L_s 214°, the circulation shows an increase in amplitude at nearly all levels of the atmosphere, and affected all latitudes except from 60°-90°N. The circulation is stronger and deeper, clearly showing the circulation's response to dust loading.

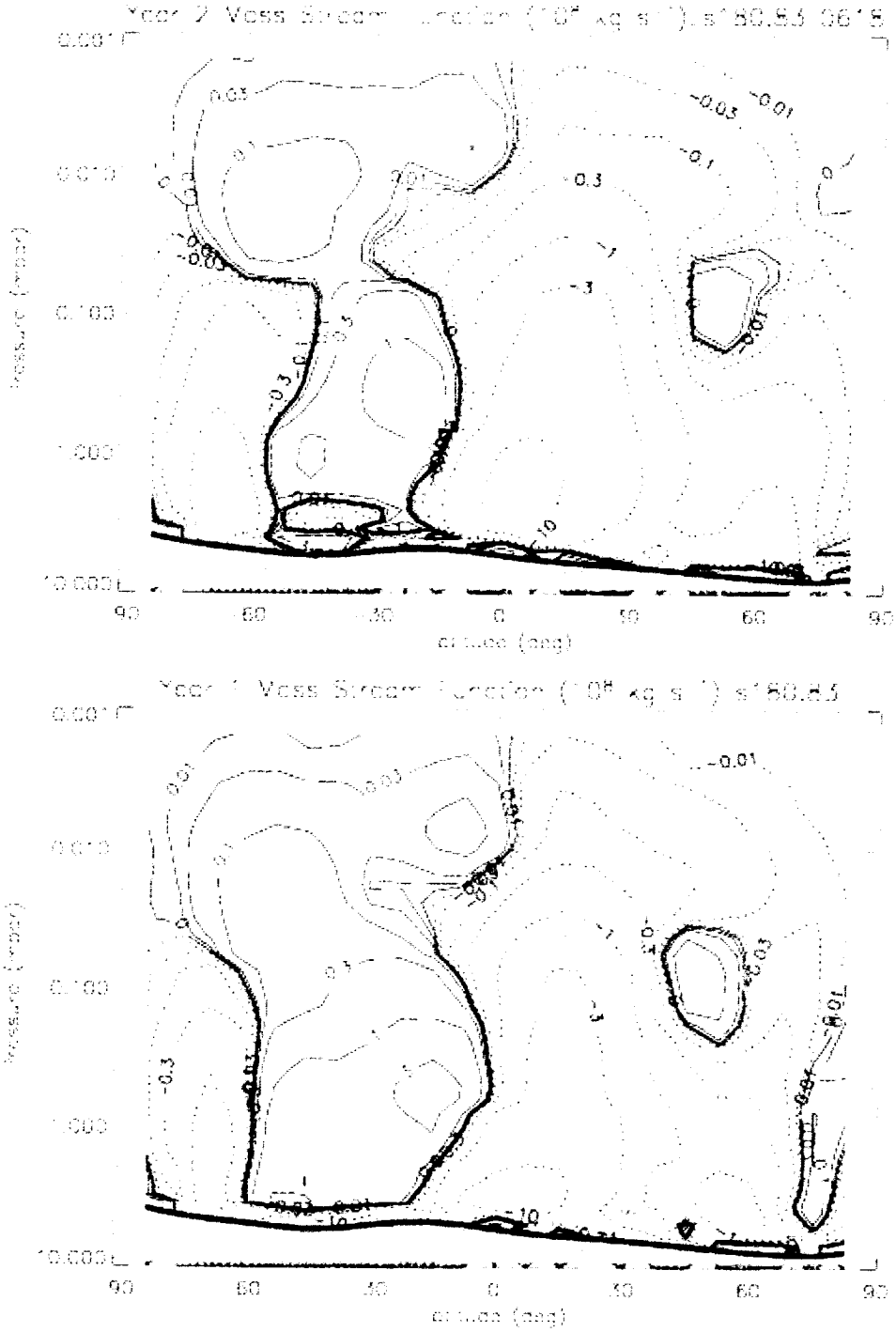

Figure 33. Mean meridional circulation at L_s 180° for year two (top) and year one (bottom). Positive contours are clockwise, negative, and counter-clockwise

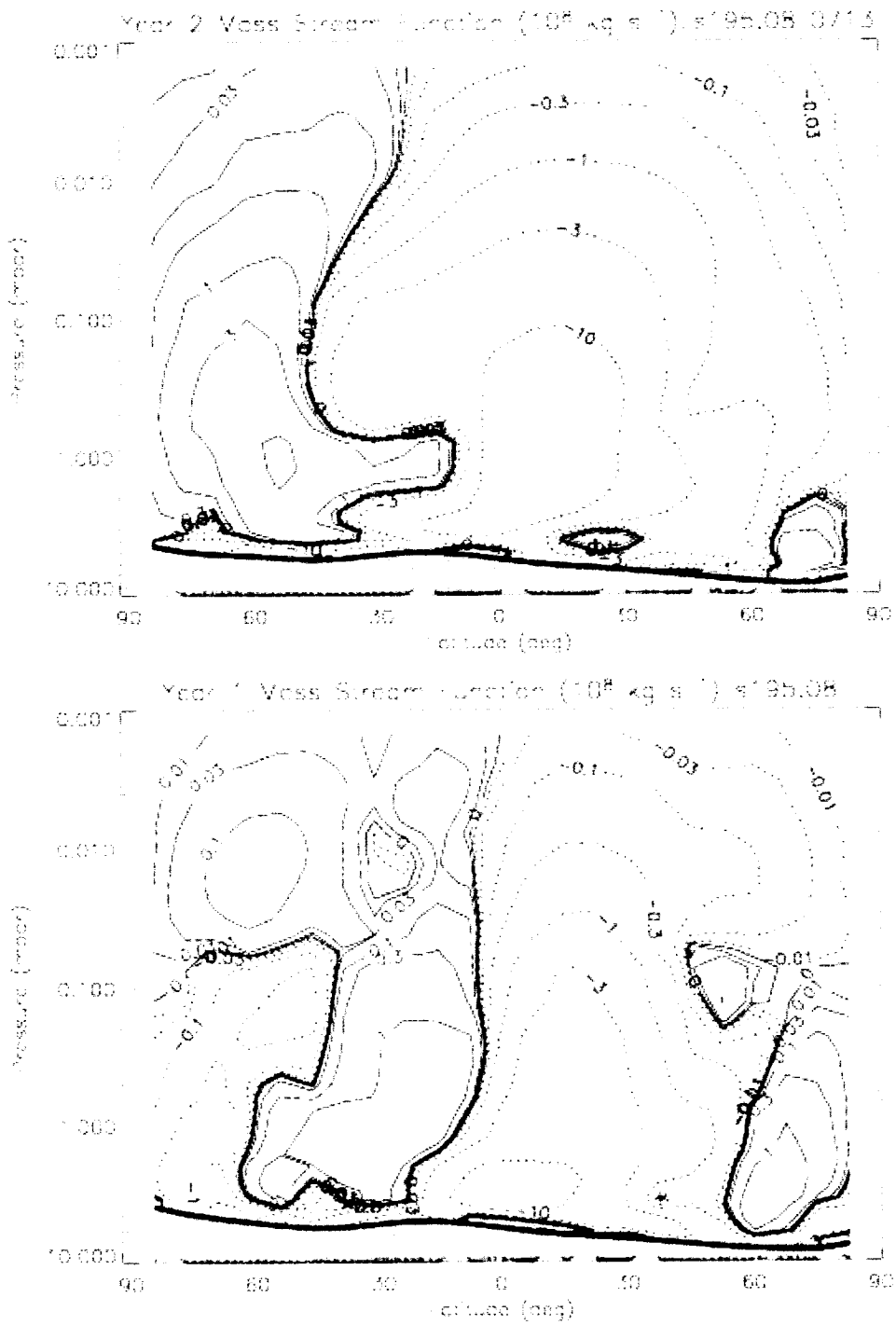

Figure 34. Mean meridional circulation at L_s 195° for year two (top) and year one (bottom). Year two shows increased amplitudes in the southern hemisphere and equatorial region.

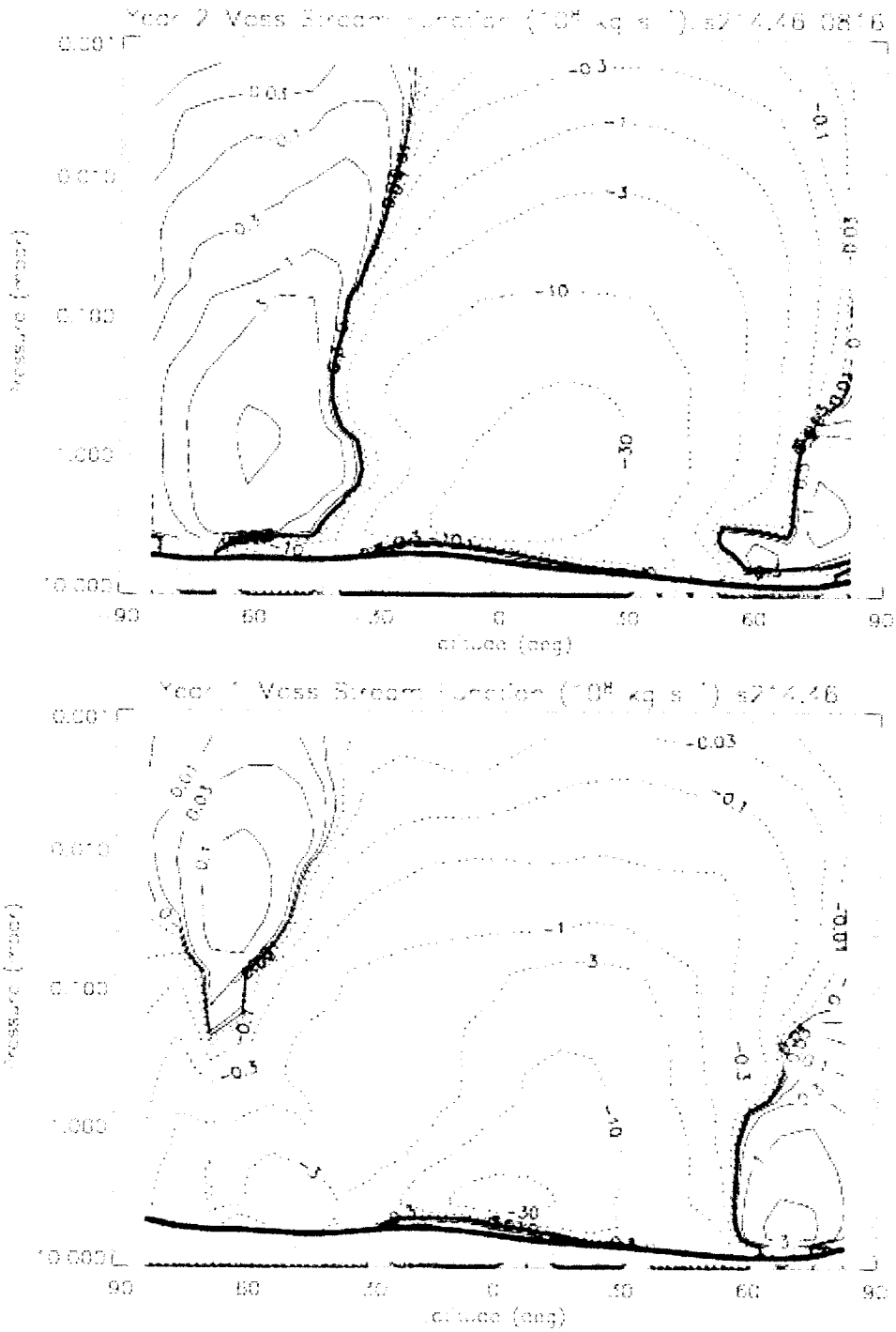

Figure 35. Mean meridional circulation at L_s 214° for year two (top) and year one (bottom). Year two shows a stronger and deeper overturning circulation, showing the effects of dust loading.

6.3.5 Stationary Waves

A wave-one stationary wave is noticed through examination of the v-wind component. Stationary waves, or time-averaged spatial variations were isolated by this approach: 1) take 10 sols of v data; 2) take the time average (vbar), which is 3-dimensional (x, y, sigma); 3) take the zonal average of time average, leaving the 2-dimensional field ([vbar]); 4) take {vbar- [vbar]} to get the time-averaged spatial variations, which shows stationary waves. Fig. 36 shows stationary wave activity at L_s 185° at the surface, when the Claritas storm is beginning to intensify. This v-field illustrates the stationary wave that influences the growth of the dust storm. A poleward push is noticed to the southeast of Hellas (-60°S, 90°-150°E). This southward-directed motion pushed dust over the cap, as discussed in Chapter 5. In the western hemisphere, 180° in longitude away, an equatorward flow is noticeable. This flow is possibly a strong influence on the development of the Claritas lifting center. Fig. 37 also shows stationary wave activity, but for both years one and two. Both years have similar features, but year two shows a more intense poleward push east of Hellas and increased northward flow in the western hemisphere. This increased northward flow of air is a possible reason for enhanced dust activity and lifting in the Claritas region.

6.4 Summary

MGCM simulations showed that many factors played a role in the development, amplitude, and decay of the 2001 global dust storm. Surface stresses, lifting rates, winds were examined to see when and where dust is lifted in the model. Model simulations

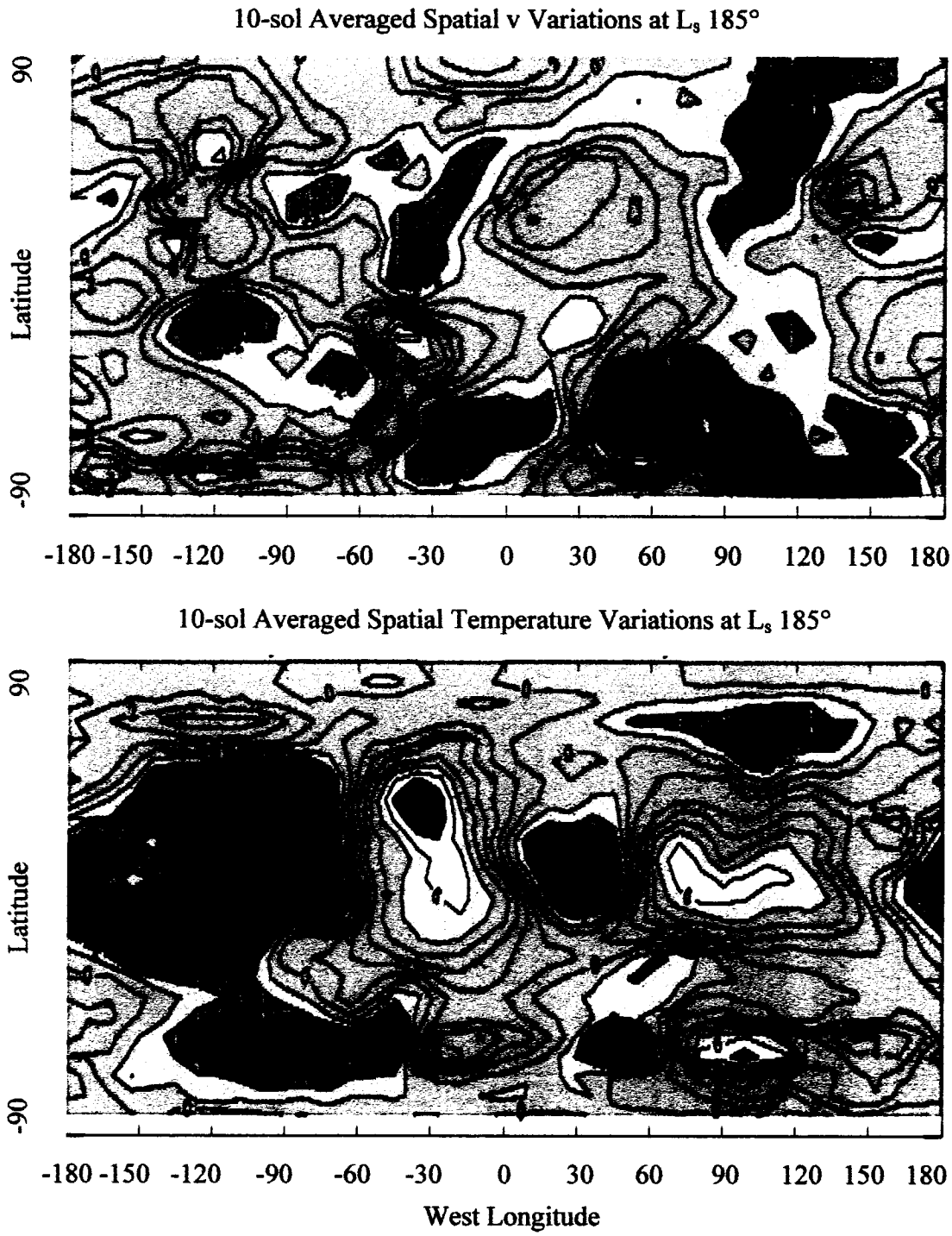

Fig. 36. v wind (top) and temperature (bottom) time-averaged spatial variations at L_s 185° (in m s^{-1}). A northward push is seen west of Hellas, but southward flow dominates east of Hellas.

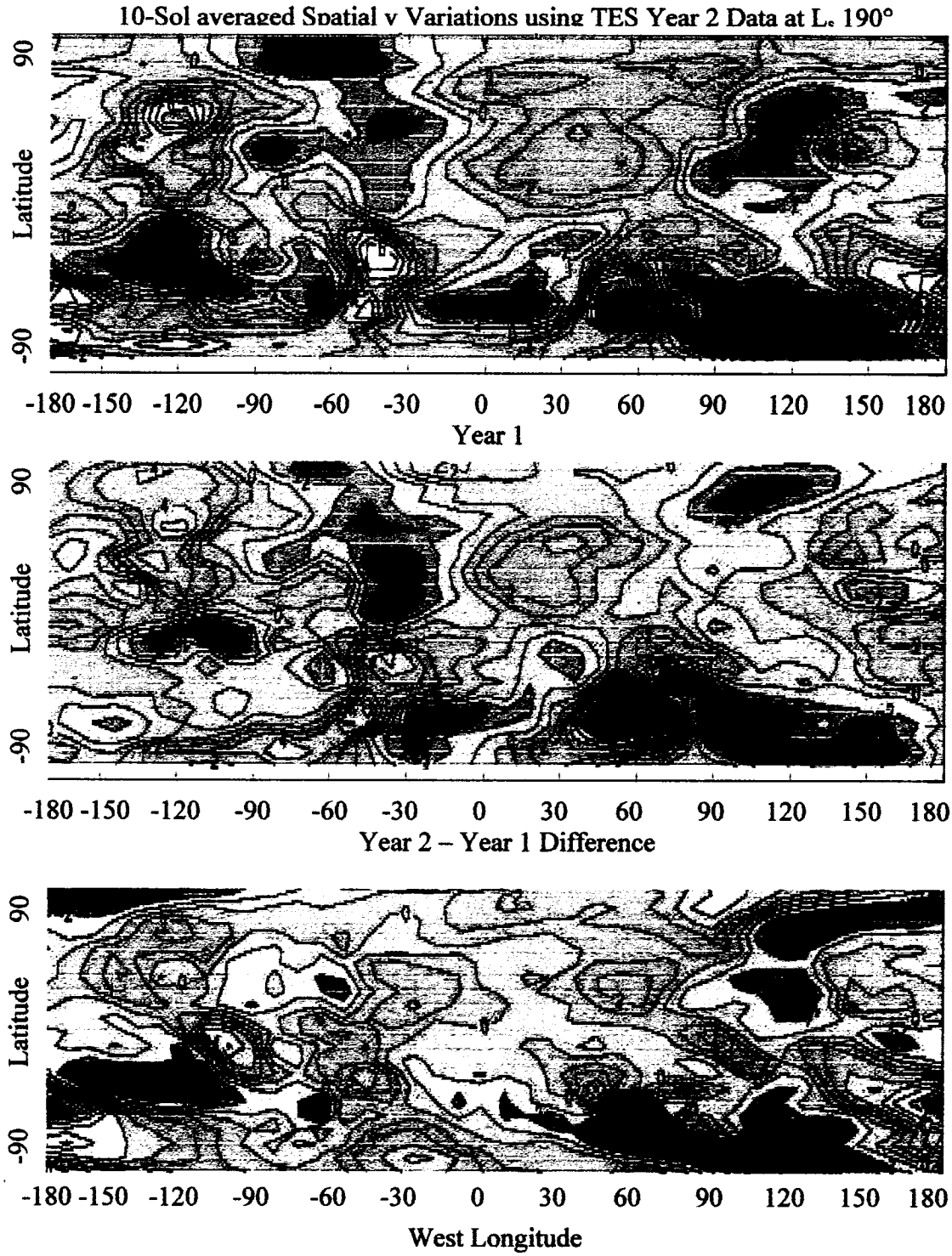

Fig. 37. v wind time-averaged spatial variations (in m s^{-1}) at L_s 190° for year two (top), year one (middle) and year two - year one (bottom). Year two shows a 6 m s^{-1} increase in wind speed near the Claritas region near the period of rapid growth.

results indicated that dust lifting occurred near the Hellas Basin near the storm's initial development. Model output also showed increases in surface stresses and lifting rate for the Claritas region. However, the simulations do not show the Claritas storm becoming the established long-term lifting center, as noticed in MOC observations. Many other model fields were examined to examine the circulation patterns and response to heavy dust loading. As the storm grew, model output showed changes in several circulation patterns. These results indicated the response of the circulation to large dust loading, and that many factors are involved in the creation of a global dust event.

An increase in the diurnal tide amplitude is apparent from MGCM output. As the storm developed, maximum wind speeds were observed to increase as more dust was lifted. Comparisons of wind speed deviations from year one showed an increase from the onset to the peak of the storm. This is a direct result of the immense amount of dust loading during the event. This increase in loading caused atmospheric temperatures to sometimes be higher at night, than during the day.

7. CONCLUSIONS

7.1 Discussion

Global dust storms are global scale events that affect many aspects of the Martian circulation. Better understanding global dust storms can lead to greater understanding of the circulation patterns on Mars. MGS data sets were combined to better examine the storm and observe how the dust storm grew, migrated and decayed. Many tasks were required to superimpose MGS data onto MOC images, such as ensuring the proper timing of each dataset, developing an interpolation scheme to better illustrate the data, and creating algorithms to read images and display the data accurately. MGS observations show the development of the global dust storm. TES observations showed an increase in 0.5 mb temperatures, a decrease in globally-averaged surface temperatures, and a large increase in global opacity. TES data alone shows that a dusty atmosphere creates an anti-greenhouse effect, as more dust loading leads to a decrease in surface temperatures. MOC images indicated the rapid increase in atmospheric dust from Ls 180°-200°, as the dust haze obscured surface features. This dust haze revealed the movement of airborne dust and the location of prominent lifting centers. Observations also showed that dust was lifted to great heights, and that it significantly affected the vertical temperature profile. TES dust opacity information confirmed the presence of two main lifting centers (Hellas and Claritas), and showed the zonal and meridional propagation of the dust. The merging of datasets allowed the 2001 global dust storm to be seen in an entirely new way.

MGCM simulations using MGS observational data were run, and they show the evolving circulation patterns during the 2001 Martian global dust storm. The superimposing of these data sets allowed for a better synopsis of the situation that allowed the circulation to be viewed in new ways, and analyzed even deeper. This study used MGCM simulations with prescribed dust data observed by TES. From these simulations, many important findings regarding tidal influence, wave activity, dust lifting, and dust transport were found. Also, these simulations allowed the circulation patterns of the planet to be viewed in response to a large dust event. Here are the conclusions in regards to the working hypotheses:

- *Baroclinic eddies and the initial onset:* Several transient disturbances were noticed on MGS observations that might have been responsible for the dust pulses seen at the onset of the storm, and that ultimately fed energy into the system so that more dust could be lifted. Low-pressure disturbances may have created strong pressure gradients leading to stronger than normal winds and enhanced dust lifting.

- *Stationary waves:* Results indicated that lifting occurs at the onset of the storm in the Hellas Basin. Stationary wave activity showed lifting occurring over southwest Hellas, pushing dust over the south cap on the eastern side of Hellas. Lifting rates and surface stress fields indicate that dust can potentially be lifted from the western Hellas region consistently through the dust storm

period, indicating that this is a storm initiation zone. The wave-one stationary wave that pushed dust over the southern cap edge east of Hellas also brought dust equatorward in the other hemisphere, possibly leading to more dust lifting in the western hemisphere, especially around Solis Planum.

- *Thermal tides and storm amplification*: As the dust levels rose in altitude in the atmosphere, an amplification of the thermal tide was noticed, mainly the semidiurnal tide. Both the surface stress and wind fields indicated a strong increase in both the diurnal and semi-diurnal component in response to dust loading. This is a typical response of the circulation to dusty conditions. The MGCM simulations indicated that lifting occurred mainly in early morning; unfortunately MOC observations were only available during the day. However, lifting rates did not indicate any consistent dust lifting during the daylight hours, which did not agree with MOC observations.

- *Development of Claritas as a lifting center*: Observations showed dust lifting south of Tharsis, in Claritas during the storm's development. However, the Claritas region did not show stress levels and lifting rates as high as in the Hellas Basin, nor did output show the region to have consistent dust activity throughout the storm's growth stage. The simulations showed an increase in dust lifting in the Claritas lifting center south of the Tharsis region, but no consistent lifting rates were seen. In fact, continuous alteration of the lifting

rate threshold values was required to consistently lift dust in regions other than Hellas. This is possibly due to a localized dust distribution or small-scale features that evaded the model. Although consistent lifting may not have been observed in the Claritas region, the existence of a semi-permanent feature to the south may have facilitated conditions sufficient for the formation of a large dust storm.

- *Mean meridional circulation:* The overturning circulation was stronger and deeper in year two than year one, indicated by stream function, temperature and wind simulations. Year two showed a weaker westerly jet in the southern hemisphere, and the winds are more westerly in the tropics. Also, the north polar vortex was enhanced in year two, with dust storm period-averaged (Ls 170 – 240°) zonal winds in the jet core at least 20 m s^{-1} greater than year one. This vortex acted to keep dust away from the northern polar regions. The enhancement of the vortex was likely due to the significant warming of the upper atmosphere by the direct absorption of solar radiation by the dust particles.

- *Storm decay:* MGCM simulations revealed that high surface stress and lifting rates are common in Hellas region throughout at most times, yet dust is not continuously lifted. MGS observations showed that dust was not lifted in Hellas for the entire storm, but mainly from L_s 180° -200°. This indicates that

the Hellas region may have had a finite amount of dust available for lifting. Once the dust reservoir was depleted, no more lifting could occur, although conditions remained favorable. Also, western Hellas appears to be a preferred region for dust lifting, although output showed that stress levels in the Hellas region did decrease as the storm neared its peak, indicating a negative feedback mechanism. That is, stress fields were high for the entire storm period, yet the magnitudes decreased as dust opacities rose. A critical level of atmospheric dust may be been reached that slowed dust lifting.

- *Year-to-year variation:* Generally, GCM simulations indicated few differences in the lifting and circulation patterns preceding the 2001 global dust storm. Surface stress patterns showed high stress values in the Hellas Basin region and near the Tharsis volcanoes, but comparisons showed few differences. Year one did have higher stresses over the northern cap, but values were slightly lower in the major dust lifting areas of Hellas and Solis Planum. Vertical temperature distributions indicated slightly warmer (5-10 K) conditions in the southern polar latitudes above the 1 mb level in year two.

7.2 Remaining Questions and Suggestions for Improvements

Not surprisingly, many questions remained unanswered in regards to the 2001 global dust storm, and for global dust events in general. The timing of this storm brings forth questions regarding seasonal variation versus dusty situations. The previous

mapping year showed similar pre-storm conditions until L_s 182°. Simulations showed that western Hellas is a preferred dust lifting area. Further analysis can be done to inspect the dust reservoir, and how its placement is crucial in determining whether enough dust can be lifted. Investigations can be done to determine why the MGCM did not indicate that the Claritas lifting center had significant lifting, although observations showed that dust was clearly consistently lifted here. A better look at the Tharsis region can be done using a higher resolution grid in the MGCM. This may allow the role of mesoscale effects such as slope flows and other local features to be examined. The Claritas storm was observed to be the main reason the 2001 storm became a global event, and some essential features could have been overlooked through the current coarse MGCM spatial resolution. More studies can inspect the seasonal versus interannual differences that apply to the storm. It is unclear which processes are unique to the dust storm year specifically, or instead are a product of the seasonal cycle. An in-depth examination can be done on transient eddies and their role in the storm's initiation. Perhaps the energy associated with transient eddies initiated dust lifting and propagation. Also, more numerical simulations can be done using non-uniform surface roughness values, which will most likely alter model dust lifting patterns. Overall, the use of an MGCM continues to increase our knowledge and insight into the Martian atmosphere, and further work will help achieve our goal of a full understanding of Martian global dust storms.

REFERENCES

Albee, A.L., 2001: Mars Global Surveyor: A success by any measure. *Engineering and Science*, **3**, 3141.

Anderson, E. and C. Leovy, 1978: Mariner-9 television limb observations of dust and ice hazes on Mars. *J. Atmos. Sci.*, **35**, 723-734.

Antoniadi, E. M., 1930: *La Planete mars 1659-1929*. Herman et Cie (Paris).

Bagnold, R. A., 1941: *The Physics of Blown Sand and Desert Dunes*. Chapman and Hall, 320 pp.

Banfield, D., B.J. Conrath, M.D. Smith, P.R. Christensen and R.J. Wilson, 2003: Forced waves in the Martian atmosphere from MGS TES nadir data, *Icarus*, **161**, 319-345.

Banfield, D., B.J. Conrath, P.J., Gierasch, R.J. Wilson and M.D. Smith, 2004: Traveling waves in the Martian atmosphere from MGS TES Nadir data. *Icarus*, **170**, 365-403.

Barker, E. S.,1971: Variations of the Martian CO_2 abundance with Martian season. *Planetary atmospheres*, Springer, C. Sagan, T. C. Owen and H. J. Smith, Springer, 425 pp.

Barnes, J. R., J. B. Pollack, R. M. Haberle, C. B. Leovy, R. W. Zurek, H. Lee, and J. Shaeffer, 1993: Mars atmospheric dynamics as simulated by the NASA Ames general circulation model, 2, Transient baroclinic eddies. *J. Geophys. Res.*, **98**, 3125-3148.

Binder, A. B. R. E. Arvidson, E. A. Guinness, K. L. Jones, E. C. Morris, T. A. Mutch, D. C. Pieri and C. Sagan, 1977: The geology of the Viking Lander 1 site. *J. Geophys. Res.* **84**, 4439-4451.

Blumsack, S. L., 1971: On the effects of topography and on planetary atmospheric circulation. *J. Atmos. Sci.*, **28**, 1134-1143.

Blumsack, S. L., P. J., Gierasch and W. R. Wessel, 1973: An analytical and numerical study of the Martian planetary boundary layer over slopes. *J. Atmos. Sci.*, **30**, 66-82.

Bridger, A. F. C. and J. R. Murphy, 1998: Mars' surface pressure tides and their behavior during global dust storms. *J. Geophys. Res.*, **103**, 8587-8601.

Briggs, G.A., W.A. Baum and J. Barnes, 1979: Viking orbiter imaging observations of dust in the Martian atmosphere. *J. Geophys. Res.*, **84**, 2795-2819.

Cantor, B. A., 2003: MGS-MOC observations of Martian dust storm activity. Sixth Inter. Conf. Mars. Pasadena, California. Abstract #3166.

Cantor, B.A., 2005: MOC Observations of the 2001 Mars planet-encircling dust event. Journal manuscript.

Cantor B.A., P.B. James, M. Caplinger and M.J. Wolff, 2001: Martian dust storms: 1999 Mars Orbiter Camera observations. *J. Geophys. Sci.*, **106**, 23653-23685.

Christensen, P. R. and Coauthors, 1992: Thermal Emission Spectrometer Experiment: Mars Observer Mission. *J. Geophys. Res.*, **97**, 7719-7734.

Christensen, P. R. and Coauthors, 1998: Results from the Mars Global Surveyor Thermal Emission Spectrometer. *Science*, **279**, 1692-1698.

Christensen, P. R. and Coauthors, 2001: The Mars Global Surveyor Thermal Emission Spectrometer experiment: Investigation description and surface science results, *J. Geophys. Res.*, **106**, 23,823-23,871.

Colaprete, A., J. R. Barnes, R. M. Haberle, J. L. Hollingsworth, H. H. Kieffer and T. N. Titus, 2005: Albedo of the south pole on Mars determined by topographic forcing of atmospheric dynamics. *Nature*, **435**, 184-188.

Conrath. B,J., 1975: Thermal structure of the Martian atmosphere during the dissipation of the dust storm of 1971. *Icarus,* **24**, 36-46.

Conrath, B. J., J. C. Pearl, M. D. Smith, W. C. Maguire, P. R. Christensen, S. Dason and M. S. Kaelberer, 2000: Mars Global Surveyor Thermal Emission Spectrometer (TES) observations: Atmospheric temperatures during aerobraking and science phasing. *J. Geophys. Res.*, **105**, 9509-9520.

Fenton, L. K., J. C. Pearl and T. Z. Martin, 1997: Mapping Mariner 9 dust opacities. *Icarus,* **130**, 115-124.

Gierasch, P. J. and R. M. Goody, 1973: A model of a Martian great dust storm. *J. Atmos. Sci.*, **30**, 169-179.

Greeley, R., R. Leach, B. R. White, J. Iversen and J. Pollack, 1980: Threshold windspeeds for sand on Mars: Winds tunnel simulations. *Geophys. Res. Lett.*, **7**, 121-124.

Greeley, R., N. Lancaster, S. Lee and P. Thomas, 1992: Martian Aeolian Processes, Sediments, and Features. *Mars*, H. H. Kieffer, B. M. Jakosky, C. W. Snyder and M. S. Matthews, Eds., University of Arizona Press, 370-766.

Haberle, R. M., C. B. Leovy and J. B. Pollack, 1979: A numerical model of the Martian polar cap winds. *Icarus*, **39**, 151-183.

Haberle, R. M., C. B. Leovy and J. B. Pollack, 1982: Some effects of global dust storms on the atmospheric circulation of Mars, *Icarus*, **50**, 322-367.

Haberle, R. M., H. C. Houben, R. Hertenstein and T. Herdtle. 1993: A Boundary-Layer Model for Mars: Comparison with Viking Lander and Entry Data. *J. Atmos. Sci.*, **50**, 1544–1559.

Haberle, R. M., J. L. Hollingsworth, A. Colaprete, A. F. C. Bridger, C. P. McKay, J. R. Murphy, J. Schaeffer and R. Freedman, 2002: The NASA/Ames general circulation model: model improvements and comparison with observations. Mars atmosphere and modeling conference, Granada, Spain.

Haberle, R.M., J. R. Murphy and J. Schaeffer, 2003: Orbital change experiments with a Mars General Circulation Model. *Icarus*, **161**, 66-89.

Hinson D.P. and R.J. Wilson, 2002: Transient waves in the southern hemisphere of Mars, *Geophys. Res. Lett.*, **29**, doi:10.1029/2001GL014103.

Hollingsworth, J. L. and J. R. Barnes, 1996: Forced stationary planetary waves in Mars' winter hemisphere. *J. Atmos. Sci.*, **53**, 428-448.

Jakosky B. M. and Barker E.S, 1984: Comparison of groundbased and Viking Orbiter measurements of Martian water vapor: Variability of the seasonal cycle. *Icarus*, **57**, 322-334.

James, P. B., H. H. Kieffer and D. A. Paige, 1992: The seasonal cycle of carbon dioxide on Mars. *Mars*, H. H. Kieffer, B. M. Jakosky, C. W. Snyder and M. S. Matthews, Eds., University of Arizona Press, 934-968.

Kahn, R.A., T.Z. Martin, R.W. Zurek and S.W. Lee, 1992: The Martian dust cycle. *Mars*, H. H. Kieffer, B. M. Jakosky, C. W. Snyder and M. S. Matthews, Eds., University of Arizona Press, 1017-1053.

Kieffer, H. H., 1979: Mars south polar spring and summer temperatures: A residual CO_2 frost. *J. Geophys. Res.*, **84**, 8263-8288.

Kieffer, H. H., S. C. Chase, T. Z. Martin, E. D. Miner and F. D. Palluconi, 1976: Martian north pole summer temperatures: Dirty water ice. *Science,* **194,** 1341-1344.

Kieffer, H. H., T. Z. Martin, A. R. Peterfreund, B. M. Jakosky, E. D. Miner and F. D> Palluconi, 1977: Thermal and albedo mapping of Mars during the Viking primary mission. *J. Geophys. Res.,* **82,** 4249-4291.

Kieffer, H.H., B. M. Jakosky and C. W. Snyder, 1992: The planet Mars: From antiquity to the present. *Mars*, H. H. Kieffer, B. M. Jakosky, C. W. Snyder and M. S. Matthews, Eds., University of Arizona Press, 1-33.

Leovy, C.B., 1985: The general circulation of Mars: Models and observations, *Adv. Geophys.*, **28,** 327-346.

Leovy, C. B, 2001: Weather and climate on Mars. *Nature,* **412,** 245-249.

Leovy, C. B. and Y. Mintz, 1969: Numerical Simulation of the Atmospheric Circulation and Climate of Mars. *J. Atmos. Sci.*, **26**, 1167–1190.

Leovy, C. B. and R. W. Zurek, 1979: Thermal tides and Martian dust storms – direct evidence for coupling. , *J. Geophys. Res.,* **84,** 2956-2968.

Leovy, C.B., R.W. Zurek and J.B. Pollack. 1973: Mechanisms for Mars Dust Storms. *J. Atmos. Sci.*, **30**, 749–762.

Malin, M. C., 1992: Mass movements on Venus: Preliminary results from Magellan cycle 1 observations, *J. Geophys. Res.,* **97,** 16337-16352.

Malin, M. C., M. A. Caplinger and S. D. Davis, 2001: Observational evidence for an active surface reservoir of solid carbon dioxide on Mars. *Science*, **294**, 2146-2148.

Malin, M. C. and B. Cantor, 2003: Mars Orbiter Camera climate observations. Mars atmosphere and modeling conference, Granada, Spain.

Malin, M. C., G. E. Danielson, A. P. Ingersoll, H. Masursky, J. Veverka, M. A. Ravine and T. A. Soulanille, 1992: The Mars Observer Camera. *J. Geophys. Res.,* **97,** 7699-7718.

Martin, L. J. and P. B. James, 1979: Persistant dust cloud activity on Mars near Echus Chasma in 1978. *Icarus,* **77**, 35-58.

Martin, L J. and R. W. Zurek, 1993: An analysis of the history of dust activity on Mars. *J. Geophys. Res.*, **98**, 3221-3246.

Mass, C. and C. Sagan, 1976: A numerical circulation model with topography for the Martian summer hemisphere. *J. Atmos. Sci.*, **33**, 1418-1430.

McLaughlin, D., 1954: Volcanism and aeolian deposition on Mars. *Bull. Geol. Soc. Amer.*, **65**, 715-717.

Moriyama, S., 1974: Effects of dust on radiation transfer in the Martian atmosphere. I. On the infrared cooling. *J. Meteor. Soc. Japan*, **52**, 457-462.

Moriyama, S., 1975: Effects of dust on radiation transfer in the Martian atmosphere. II. Heating due to the absorption of the visible solar radiation and importance of radiative effects of dust on the Martian meteorological phenomena. *J. Meteor. Soc. Japan*, **53**, 214-220.

Moriyama, S. and T. Iwashima, 1980: A spectral model of the atmospheric general circulation of Mars: A numerical experiment including the effects of suspended dust and topography. *J. Geophys. Res.*, **85**, 2847-2860.

Mutch, T. A. and Coauthors, 1976: The surface of Mars: The view from the Viking 1 Lander. *Science*, **193**, 791-801.

Paige, D. A., K. E. Herkenhoff and B. C. Murray, 1990: Mariner 9 observations of the south polar cap of Mars: Evidence for residual CO_2 frost. *J. Geophys. Res.*, **95**, 1319-1335.

Pearl, J. C., M. D. Smith, B. J. Conrath, J. L. Banfield and P. R. Christensen, 2001. Observations of Martian ice clouds by the Mars Global Surveyor Thermal Emission Spectrometer: The first Martian year, *J. Geophys. Res.*, **106**, 12,325-12,338.

Peterfreund, A.R. and H.H. Kieffer, 1979: Thermal infrared properties of the Martian atmosphere 3. Local dust clouds. *J. Geophys. Res.*, **84**, 2853-2862.

Pollack, J. B., C.B. Leovy, Y. Mintz and W. Van Camp, 1976: Winds on Mars during the Viking season: Predictions based on a general circulation model with topography. *Geophys. Res. Lett.*, **3**, 479-483.

Pollack, J. B., D. Colburn, R. Kahn, J. Hunter, W. Van Camp, C. E. Carlston and M. R. Wolf, 1977: Properties of aerosols in the Martian atmosphere, as inferred from Viking Lander imaging data. *J. Geophys. Res.*, **82**, 4479-4496.

Pollack, J. B., D. S. Colburn, F. M. Flasar, R. Kahn, C. E. Carlston and D. C. Pidek, 1979: Properties and effects of dust particles suspended in the Martian atmosphere. *J. Geophys. Res.*, **84**, 2929-2945.

Pollack, J. B., C. B. Leovy, P. W. Greiman and Y. Mintz, 1981: A Martian general circulation experiment with large topography. *J. Atmos. Sci.*, **38,** 3-29.

Pollack, J. B., R. M. Haberle, J. Schaeffer and H. Lee, 1990: Simulations of the general circulation of the Martian atmosphere. I. Polar Processes. *J. Geophys. Res.*, **95,** 1447-1473.

Pollack, J. B., M. E. Ockert-Bell and M. K. Shepard, 1995: Viking Lander image analysis of Martian atmospheric dust. *J. Geophys. Res.*, **100**, 5235-5250.

Richardson, M. I. and R. J. Wilson, 2002: A topographically forced asymmetry in the martian circulation and climate. *Nature,* **416**, 298-301.

Ryan, J. A., 1964: Notes on the Martian yellow clouds. *J. Geophys. Res.*, **69,** 3759-3770.

Ryan, J. A. and R. M. Henry, 1979: Mars atmospheric phenomena during major dust storms as measured at the surface. *J. Geophys. Res.*, **84,** 2821-2829.

Ryan J. A. and R. D. Lucich, 1983: Possible dust devils, vortices on Mars, *J. Geophys. Res.*, **88,** 11005-11011.

Schneider, E. K., 1983: Martian great dust storms: Interpretive axially symmetric models. *Icarus,* **55,** 302-331.

Sharp, R. P. and M. C. Malin, 1984: Surface geology from Viking landers on Mars: A second look. *Geol. Soc. Amer. Bull.*, **96**, 1398-1412.

Siili, T., R.M. Haberle and J. R. Murphy, 1997: Sensitivity of Martian southern polar cap edge winds and surface stresses to dust optical thickness and to the large-scale sublimation flow. *Planetary Atmospheres and Ionospheres and Reference Atmospheres, Adv. Space Res.*, **19,** 1241-1244.

Slipher, E. C., 1962: *The Photographic Story of Mars.* Northland Press, 168 pp.

Smith, D. E., M. T. Zuber and G. A. Neumann, 2001: Seasonal variations of snow depth on Mars. *Science*, **294**, 2141-2146.

Smith, M.D., 2003: Interannual variability in TES atmospheric observations of Mars during 1999-2003. *Icarus*, **167**, 148-165.

Smith, M. D., J. L. Banfield and P. R. Christensen, 2000. Separation of atmospheric and surface spectral features in Mars Global Surveyor Thermal Emission Spectrometer (TES) spectra, *J. Geophys. Res.*, **105**, 9589-9609.

Smith, M. D., J. C. Pearl, B. J. Conrath and P. R. Christensen, 2001: Thermal Emission Spectrometer results: Mars atmospheric thermal structure and aerosol distribution, *J. Geophys. Res.*, **106**, 23,929-23,945.

Smith, M. D., J. C. Pearl, B. J. Conrath and P. R. Christensen, 2002: Thermal Emission Spectrometer observations of Martian planet-encircling dust storm 2001A. *Icarus*, **157**, 259-263.

Strausberg, M.J, H. Wang, M.I. Richardson, S.P. Ewald and A.D. Toigo, 2005: Observations of the initiation and evolution of the 2001 Mars global dust storm. J. *Geophys. Res.*, **110**, 2006-2031.

Thomas, P. C. and P. J. Gierasch, 1985: Dust devils on Mars. *Science*, **230**, 175-177.

Tillman, J. E., 1988: Mars global atmospheric oscillations: Annually synchronized, transient normal mode oscillations and the triggering of global dust storms. *J. Geophys. Res.*, **93**, 9433-9451.

Toon, O. B., J. B. Pollack and C. Sagan, 1977: Physical properties of the particles composing the Martian dust storm of 1971-1972. *Icarus*, **30**, 663-696.

Wells, E. N., J. Veverka and P. Thomas, 1984: Mars: Experimental study of albedo changes caused by dust fallout. *Icarus*, **58**, 331-338.

Wilson R.J. and K. Hamilton 1996: Comprehensive model simulation of thermal tides in the Martian atmosphere. *J. Atmos. Sci.* **53**. 1290-1326.

Wilson, R.J., D. Banfield, B.J. Conrath and M.D. Smith, 2002: Traveling waves in the Northern Hemisphere of Mars, *Geophys. Res. Lett.*, **29**, 50-64.

Ye, Z. J., M. Sega and R. A. Pielke, 1990: A comparative study of daytime thermally induced upslope flow on Mars and Earth. *J. Atmos. Sci.*, **47**, 612-648.

Zurek R. W., 1976: Diurnal tide in the Martian atmosphere. *J. Atmos. Sci.*, **33**, 321-337.

Zurek, R. W., 1982: Martian great dust storms: An update. *Icarus*, **50**, 288-310.

Zurek, R.W. and C.B. Leovy, 1981: Thermal tides in the dusty Martian atmosphere: A verification of theory, *Science*, **213**, 437-439.

Zurek, R.W., J. Barnes, R.M. Haberle, J. Pollack, J. Tillman and C. Leovy, 1992: Dynamics of the Atmosphere of Mars. *Mars*, H. H. Kieffer, B. M. Jakosky, C. W. Snyder and M. S. Matthews, Eds., University of Arizona Press, 730-766.

Jeffrey M Gawrych
2184 Peachtree Ln
San Jose, CA 95128

March 23, 2007

Dr. Michael D. Smith
NASA Goddard Space Flight Center
Greenbelt, MD 20771

Dear Dr. Smith:

This letter confirms our recent email conversation. I am completing a master's thesis at San Jose State University entitled "The 2001 Global Dust Storm." I would like your permission to reprint in my thesis figures from the following:

> Smith, M. D., J. C. Pearl, B. J. Conrath and P. R. Christensen, 2001: Thermal Emission Spectrometer results: Mars atmospheric thermal structure and aerosol distribution, *J. Geophys. Res.*
>
> The two figures top be reproduced are 1) Water Vapor Column Abundance and 2) Dust Optical Depth.

The requested permission extends to any future revisions and editions of my thesis, including non-exclusive world rights in all languages, and to the prospective publication of my thesis by UMI. These rights will in no way restrict republication of the material in any other form by you or by others authorized by you. Your signing of this letter will also confirm that you own [or your company owns] the copyright to the above-described material.

If these arrangements meet with your approval, please sign this letter where indicated below and return it to me in the enclosed return envelope. Thank you very much.

Sincerely,

Jeffrey M Gawrych

PERMISSION GRANTED FOR THE
USE REQUESTED ABOVE:

Michael D Smith

[Dr. Michael D. Smith]

Date: 3/27/07